Nanostructured Copper Electrodes for Organic Photovoltaics

By

Oliver Samuel Hutter

A thesis submitted for the degree of

Doctor of Philosophy

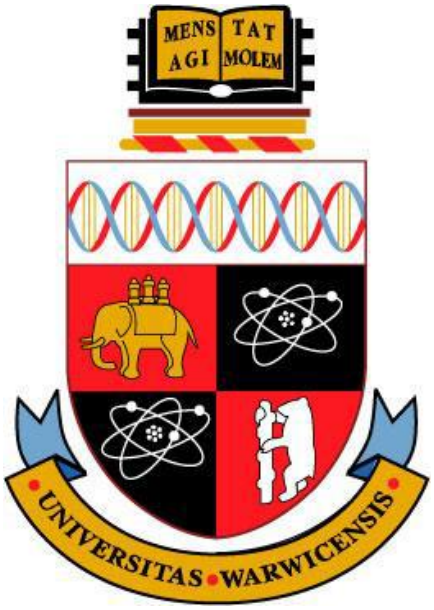

Supervised by **Dr. Ross A. Hatton**

Department of Chemistry,

University of Warwick, UK

March 2015

Abstract

This thesis describes a body of original research focused on the development of a viable alternative to the indium-tin oxide (ITO) glass window electrode used in organic photovoltaic (OPV) devices, based on the use of ultra-thin Cu films.

The first results chapter describes a low cost, robust Cu | Al bilayer window electrode that simultaneously functions as the low work function electron-extracting electrode and as a sink for oxygen/water molecules in OPVs. When the electrode is exposed to air, an ultra-thin oxide layer forms at its surface without any increase in surface roughness, and the sheet resistance of the electrode actually decreases. However, this electrode has the disadvantage of a lower far-field transparency than ITO glass. The second results chapter describes how the transparency of ultra-thin Cu films can be increased to a level comparable to that of ITO glass across most of the spectrum over which OPVs harvest light using an overlayer of tungsten sub-oxide (WO_{3-x}) which is spontaneously doped with Cu, increasing both its refractive index and electrical conductivity. Unfortunately these electrodes are not air stable. The third results chapter describes how the developments described in the previous two chapters might be integrated to realise an electrode that is both air-stable and highly transparent. The final results chapter describes a very different approach to coupling light into an OPV based on a Cu electrode with a dense array of sub-optical wavelength apertures. These electrodes absorb light strongly, concentrating it as surface plasmon excitations. It is shown that this trapped light can be absorbed by the light harvesting organic semiconductor in organic photovoltaics so that electrodes with very low far-field transparency can perform as well as more transparent electrodes.

Table of Contents

Acknowledgements

I would like to thank Warwick University for the Chancellor's Scholarship which funded me to carry out this research.

I would like to thank Dr. Josephine Bunch (University of Birmingham), for assistance with collecting the s-SIMS data, Dr. Marc Walker (University of Warwick, Department of Physics) for assistance with the XPS and UPS data collection and Professor Tim S. Jones for use of his group atomic force microscope and other laboratory equipment. I would like to thank the Jones group for all of their technical support throughout the project, particularly Dr. Paul Sullivan, who helped train me on many pieces of equipment.

I would like to thank everyone in the Hatton research group including Martin Tyler, Kenny Marshall and Helena Stec. I'd also like to thank Luke Daniels for his help and support with my many queries along the way. I'd like to thank my parents, without their love and care I could achieve very little in this world.

Lastly I would like to thank Ross, whose door was always open to me; his support and guidance throughout my PhD have been brilliant and I feel very privileged to have had such an excellent supervisor.

List of Publications

- *"An Indium-Free Low Work Function Window Electrode for Organic Photovoltaics Which Improves with In-Situ Oxidation"* O.S. Hutter, H.M. Stec, R. A. Hatton, *Adv. Mater.* **2013**, *25*, 284.
- *"A Hybrid Copper:Tungsten Suboxide Window Electrode for Organic Photovoltaics"* O.S. Hutter, R.A. Hatton, *Adv. Mater.* **2015**, *27*, 326.

Patents

- R. A. Hatton, O. S. Hutter, GB1409381.0, Filed

Declaration

The work presented in this thesis was conducted at the Department of Chemistry, University of Warwick in Coventry with the exception of the X-ray photoelectron spectroscopy (XPS), ultra-violet photoelectron spectroscopy (UPS), and secondary ion mass spectrometry (SIMS) measurements. The XPS and UPS measurements were carried out in the Department of Physics, University of Warwick with the assistance of Dr. Marc Walker, and the SIMS measurements were carried out in the Department of Chemistry, University of Birmingham with the assistance of Dr. Josephine Bunch. All data collection was performed by me with the exception of the reflectivity of thick Ag and Al films (Figure 6.25), which was recorded by Martin Tyler. I confirm that none of the work included has previously been submitted for a higher degree. Parts of the work have been patented, published in scientific journals and were presented at conferences, symposiums and consortium meetings.

Abbreviations and Acronyms

AFM: Atomic force microscopy

AM1.5: Air Mass 1.5

AOs: Atomic orbitals

BHJ: Bulk heterojunction

CB: Conduction band

DMD: Dielectric metal dielectric

DSSC: Dye sensitized solar cells

E_f : Fermi level

E_g: Band gap

EQE: External quantum efficiency

FF: Fill factor

HOMO: Highest occupied molecular orbital

HOPG: Highly orientated pyrolytic graphite

HPLC: High performance liquid chromatography

IPCE: Incident photon to converted electron

J_{MPP}: Current density at the maximum power point

J_{sc}: short circuit current density

LUMO: Lowest unoccupied molecular orbital

MOs: Molecular orbitals

kWh: Kilowatt hour

OFETs: Organic field effect transistors

OLEDs: Organic light emitting diodes

OPV: Organic photovoltaic

PCE: Power conversion efficiency

PV: Photovoltaic

QCM: Quartz crystal microbalance

RMS: Root mean squared

rpm: Revolutions per minute

R_S: Series resistance

R_{SH}: Sheet resistance

R_{SHUNT}: Shunt resistance

SAM: Self-assembled monolayer

SPP: Surface plasmon polariton

SPR: Surface plasmon resonance

UV: Ultra-violet

VB: Valence band

V_L: Vacuum level

V_{MPP}: Voltage at the maximum power point

V_{oc}: Open circuit voltage

XPS: X-ray photoelectron spectroscopy

%T: %Transmission or %transparency

Φ: Work function

Ω sq^{-1}: Ohms per square

List of chemicals and compounds

APTMS: (3-aminopropyl)trimethoxysilane

BCP: 2,9-dimethyl-4,7-diphenyl- 1,10-phenanthroline or Bathocuproine

CdTe: Cadmium telluride

CIGS: Copper indium gallium selenide

CNT: Carbon nanotube

ClAlPc: Chloroaluminium phthalocyanine

C_{60}: Buckminster fullerene

IPA: Isopropanol

ITO: Indium-tin oxide

MPTMS: (3-mercaptopropyl)trimethoxysilane

PCDTBT:Poly[N-9'-heptadecanyl-2,7-carbazole-alt-5,5-(4',7'-di-2-thienyl-2',1',3'-benzothiadiazole)]

$PC_{60}BM$ or PCBM: [6,6]-phenyl-C_{61}-butyric acid methyl ester

$PC_{70}BM$: 30H-cyclopropa[8,25][5,6]fullerene-C_{71}-D5h(6)-30-butanoic acid, 30-phenyl-, methyl ester

PEDOT:PSS: poly(3,4-ethylenedioxythiophene):poly(styrenesulfonate)

PEN: Polyethylene naphthalate

PET: Polyethylene terephthalate

PTB7: poly- [[4,8-bis[(2-ethylhexyl)oxy]benzo[1,2-b:4,5-b0]dithiophene-2,6-diyl]- [3-fluoro-2-[(2-ethylhexyl)carbonyl]thieno[3,4-b]thiophenediyl]

P3HT: Poly(3-hexylthiophene-2,5-diyl)

Spiro-OMeTAD: 2,2(,7,7(-tetrakis-(N,N-di-pmethoxyphenylamine)9,9'-spirobifluorene

WO_3/WO_{3-x}: Tungsten oxide

Chapter 1- Introduction

1.1 Context

Energy demand is currently soaring due to the increasing world population, which is expected to saturate at ~9 billion people in 2050,[1] and the increasing affluence per capita of many nations. The latter is in large part due to the industrialisation of the very populous nations of India and China.

With global warming due to greenhouse gas emissions, particularly CO_2, giving rise to climate change,[2] low carbon and renewable sources of energy are needed now more than ever. Nations are also striving to secure energy independence, which is driving the development and uptake of renewable energy technologies.[2]

The development and implementation of renewable energy technologies has grown hugely in the past decade; for example, the generation capacity of photovoltaic (PV) panels increased ten-fold between 2000 and 2011.[3] Substantial proportions of many nations' electricity demands are already generated by renewable energy technologies, with renewable energy supplying 18% of the United Kingdom's electricity in the last quarter of 2013.[4] In 2013 the United Kingdom produced 28% more electricity from renewable sources than in the previous year, despite overall electricity generation falling 2% in the same period due to more efficient use of energy.[4] Each different renewable energy technology has its own output variability; for example PVs do not produce electricity at night and the generating capacity varies continuously throughout the day. Thus a mix of renewable technologies is often beneficial for power generation on a large scale. Two billion people currently live without a connection to grid electricity and so developing low carbon, economically viable means of electricity generation at the point

of use is therefore an important challenge. PVs are a very promising option for achieving this.

PVs are the second most studied renewable energy technology after wind turbines.[5] This is due to the many advantages of PVs including low operating costs, portability, and use as a source of power at the point of use without the need for a grid connection. With the sun delivering more energy to earth in one hour than humanity uses in one year,[6] and the cost of electricity generated using PVs already near to grid parity in some sunnier parts of the world,[7] PV technologies are now beginning to play a pivotal role in the energy sector.

1.2 Existing Photovoltaic Technologies

The archetypal PV device is based on inorganic materials and has an active layer made of either mono or poly-crystalline silicon. This type of PV offers a power conversion efficiency (*PCE*) of up to ~25% and excellent stability which results in operational lifetimes of up to 30 years.[8] Over the past 40 years the cost of producing silicon PVs has fallen drastically and *PCE* has steadily increased, reducing the cost per watt of electricity they generate to a level comparable with other more established renewable technologies.[9] However, inorganic PV modules are still relatively expensive to produce due to the large amount of energy required in the material purification and processing stages. Polycrystalline silicon PVs are lower cost than monocrystalline PV, but are still more expensive than third generation PV technologies based on thin films.

In addition to first and second generation PVs, there are many new PV technologies being researched, including organic photovoltaics (OPVs), perovskite PVs,[6,10] dye sensitised solar cells (DSSC),[11] copper indium gallium selenide (CIGS) PVs[12] and quantum dot PVs[13,14] which are based on thin films of photoactive

semiconductors. These thin film PVs are advantageous as they use much less active material (layer thickness < 1 μm) than crystalline Si PVs (layer thickness > 100 μm),[15] which reduces the cost of materials, processing speed and energy required in their fabrication.

All thin film PVs have different stabilities, *PCE* and fabrication costs and so are matched to different potential applications. OPVs have the potential to be one of the lowest cost of all emerging thin film PV technologies due to the very low semiconductor film thickness and the possibility of processing organic semiconductors at low temperatures from solution.[16] Thus, OPVs have strong potential to deliver a transformative reduction in the cost of generating electricity directly from sunlight.[17-19] However, OPVs like all other thin film PV technologies require a transparent electrode, and the existing industry standards are too expensive and poorly matched to the needs of OPV.

1.3 Organic Semiconductors

Organic semiconductors are highly conjugated carbon based molecules that have conduction properties between those of metals and insulators. Organic semiconductors typically have a band gap of 2-3 eV and can be small molecules (e.g. C_{60}, Figure 1.17) or polymeric materials (e.g. poly- [[4,8-bis[(2-ethylhexyl)oxy]benzo[1,2-b:4,5-b0]dithiophene-2,6-diyl]-[3-fluoro-2-[(2-ethylhexyl)carbonyl]thieno[3,4-b]thiophenediyl] (PTB7), Figure 1.13). This class of semiconductor are molecular solids and so their bulk properties are dominated by those of the individual molecules.

When atoms are brought together to form molecules, their atomic orbitals (AOs) spatially overlap and some of the valence AOs merge to form molecular orbitals (MOs), whilst the core AOs remain largely unperturbed. These MOs can be classified as either

bonding (lower energy), or anti-bonding (higher energy) MOs. In an organic semiconductor, often the *s* and two of the *p* AOs of carbon form sp^2 hybridised orbitals, which make up the σ bonded framework of the molecule. The remaining *p* AOs which are out of the plane of the σ bonded framework then form delocalised π molecular orbitals at higher energies than their σ counterparts, which give rise to the optical and electronic properties of organic semiconductors. The highest occupied molecular orbital (HOMO) in a molecule consists of π bonding MOs and the lowest unoccupied molecular orbital (LUMO) comprises π anti-bonding MOs as illustrated in Figure 1.1. The HOMO and LUMO in an organic semiconductor are equivalent to the valence band (VB) and conduction band (CB) edges respectively in an inorganic semiconductor.

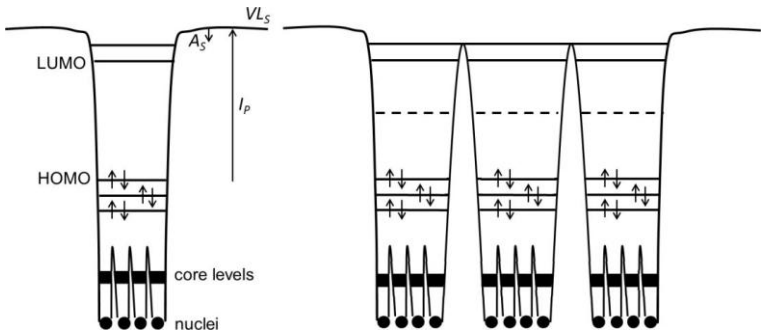

Figure 1.1: The energy levels of an isolated organic molecule (left) and a molecular solid (right), with individual atoms / molecules depicted as potential wells.[20] I_p, VL_S and A_S correspond to the ionisation potential, the vacuum level at the surface and the solid state electron affinity respectively.

The difference between the VB and the CB edges is known as the band gap (E_g). Insulators have large band gaps (>3 eV), conductors have a band gap equal to zero (i.e. a partially filled band) and semiconductors have intermediate band gaps (typically 1-3 eV),

as illustrated in Figure 1.2. Thermal excitation of electrons across the band gap in intrinsic semiconductors at room temperature is minimal and so free charge carriers in semiconductors required for appreciable conduction are produced by the injection of electrons (or holes) into the CB or VB using an electric field or by photo-excitation of electrons from the VB to the CB.

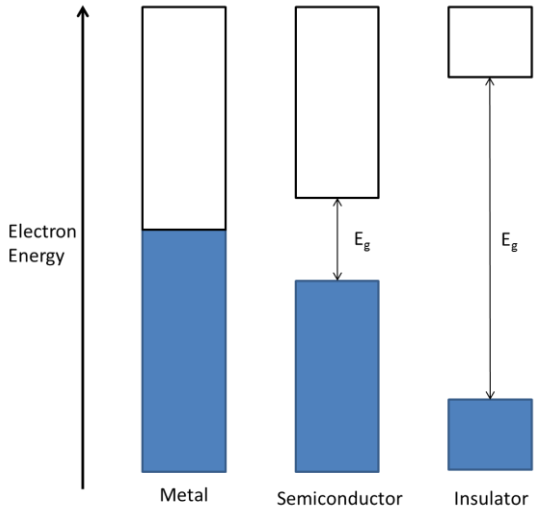

Figure 1.2: Schematic energy level diagrams of a metal, semiconductor and an insulator are shown from left to right. Occupied bands are depicted in blue, with unoccupied bands in white.

The HOMO-LUMO gap in an organic semiconductor is the primary determinant of its colour; for example, the E_g of poly[N-9'-heptadecanyl-2,7-carbazole-alt-5,5-(4',7'-di-2-thienyl-2',1',3'-benzothiadiazole)] (PCDTBT) is ~1.9 eV, which corresponds to an absorption onset at 650 nm.[21] This is in the red part of the spectrum, so this semiconductor is purple in colour. The E_g combined with the accessibility of the frontier orbitals (HOMO and LUMO) determines the electrical properties of the material in a device.

Organic semiconductors typically have low charge carrier mobilities because charge carriers must hop between the potential wells associated with each molecule, and high electric field strengths are therefore required to inject/extract charge carriers. Consequently, very thin active layer thicknesses of typically <200 nm are used in OPVs. The primary advantage of organic semiconductors over conventional inorganic semiconductors for PV applications is that they can be processed at low temperature from solution, which should enable rapid production of low cost PV modules.

1.4 Organic Photovoltaics

The heterojunction OPV was first reported by Tang in 1986, with a *PCE* of ~1% and was based on a bilayer of electron donor and electron acceptor type molecules.[22] However, it was not until the turn of the century that this *PCE* was increased from ~1% to above 11% in 2013;[23] a level considered to be sufficient for commercialisation.[24-26] This rapid progress stemmed from the invention of the bulk-heterojunction (BHJ) device structure; a complex interpenetrating blend of electron donor and electron acceptor type molecules. This progress is illustrated in Figure 1.3, which shows the peak efficiency for laboratory scale BHJ OPVs from 2001 to 2013.

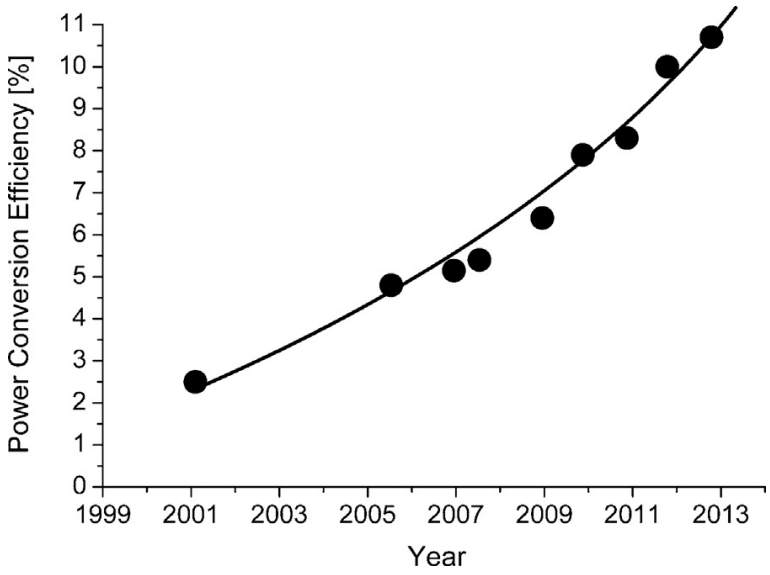

Figure 1.3: Certified *PCE* values for lab scale single layer solution processed OPVs which were published in the journal *Progress in Photovoltaics*, taken from Scharber *et al.*[23]

OPVs have the potential to be a cost effective alternative to inorganic PVs in some applications[27] including for off-grid power generation in developing countries.[7,28] Their light weight and low profile as compared to inorganic PVs also makes them attractive for transport applications. Other potential advantages of OPVs over conventional Si PVs include (i) lower production costs due to the thin film architecture; (ii) the possibility of rapid roll-to-roll production; (iii) low energy input during fabrication translating to very low CO_2 emissions per KWh of energy generated; (iv) the possibility of semi-transparent modules enabling integration with windows.[28] However, issues with stability are prevalent, the *PCE*s are lower, and this technology is still essentially pre-commercialised.[28] With fast roll-to-roll production methods enabling OPV modules to be produced at low cost and at high speed, energy payback times of 180 days have already been demonstrated,[29] where energy payback time is "the time required for

the PV system to generate the equivalent amount of energy consumed in the construction and decommissioning phases".[28] Energy payback times as short as one day have been forecast for OPVs.[17]

The main challenges in OPV research are to increase the *PCE* and the stability, whilst maintaining the cost advantage over conventional PV technologies. Novel organic polymeric materials for active layers of OPVs are a key step in driving up the *PCE* values,[30] as narrow band gap electron donor materials are required to harvest more of the solar irradiance (Figure 1.4).

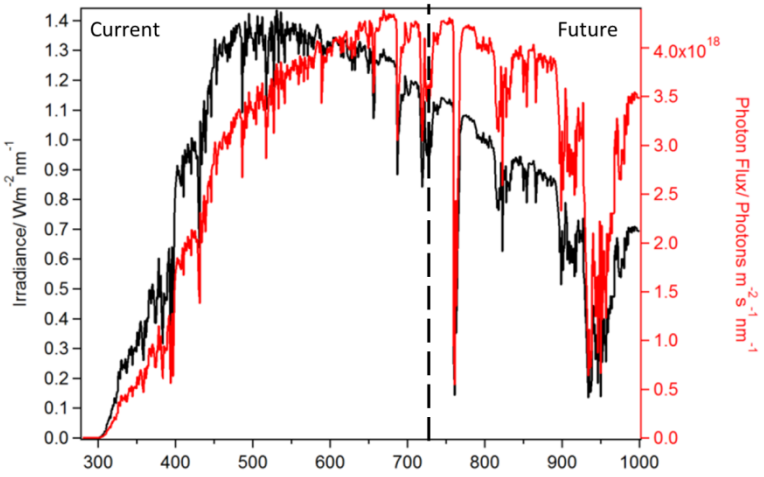

Figure 1.4: The air mass 1.5 (AM1.5) solar irradiance (black) and photon flux (red).[31]

Since most organic semiconductors are susceptible to photo-oxidation, device lifetimes can be improved by blocking the ingress of O_2 into the photoactive layer, and so a great deal of research effort is currently directed at the development of low cost encapsulants for OPVs.

1.5 Principles of Organic Photovoltaic (OPV) Operation

In an OPV, light enters the device through a transparent electrode, and is absorbed by the light harvesting organic semiconductor layer. Upon light absorption a Frenkel exciton is formed, which is a coulombically bound electron and hole pair on the same molecule (Figure 1.5, step 1). Frenkel excitons typically have binding energies of 0.2-1 eV in organic semiconductors and diffuse between molecules (Figure 1.5, step 2), visiting 10^2-10^3 individual molecules before relaxation to the ground state. Frenkel excitons can be dissociated into free electrons and holes at the junction between two different types of organic semiconductor having offset frontier orbital energies such that one serves as an electron donor to the other. Examples of organic semiconductors with donor and acceptor type character are given in Section 1.8 of this thesis. This junction is called a heterojunction due to the abrupt discontinuity in HOMO and LUMO levels. The electron accepting material then transports the free electron to the cathode and the electron donating material transports the free hole to the anode (Figure 1.5, step 4). The electron donor material is therefore the organic semiconductor that will donate electrons into the LUMO of the electron acceptor from the electron donor's LUMO at the heterojunction (Figure 1.5).

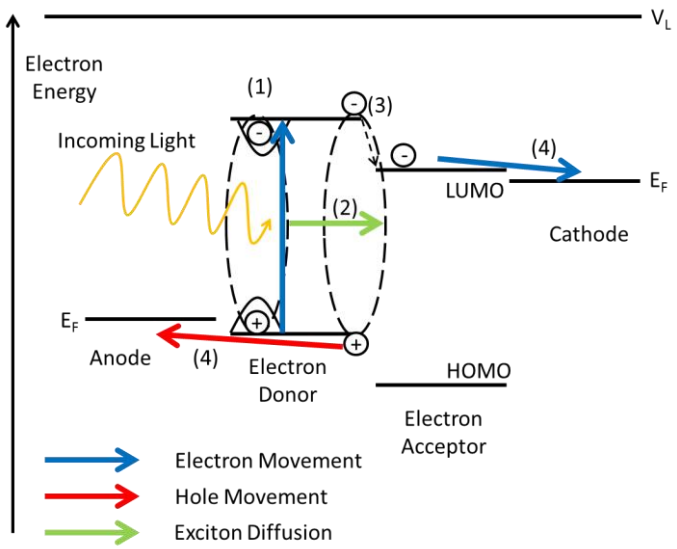

Figure 1.5: Schematic energy level diagram for an OPV device. The flow of electrons (blue) and holes (red) through the HOMOs and LUMOs respectively is shown.

Splitting of excitons at the organic heterojunction can occur with near 100% efficiency.[33] There is however only a limited distance an exciton can diffuse before it relaxes to the ground state, since the lifetime of a singlet exciton is of the order of 1 ns.[33] Triplet excitons are longer lived although more strongly bound and so more energy is required to dissociate them. The small exciton diffusion length in organic semiconductors constrains the organic semiconductor layer thickness in a simple bilayer device to tens of nms at most.

A BHJ is a complex interpenetrating network of donor and acceptor phases which are separated on a scale close to the exciton diffusion length in both materials (Figure 1.6). This architecture ensures all excitons formed in either phase are within a diffusion length of a dissociating interface, which enables the use of thicker photo-active

layers. However, the resistance to charge carrier extraction is increased due to a less direct path to the electrodes.

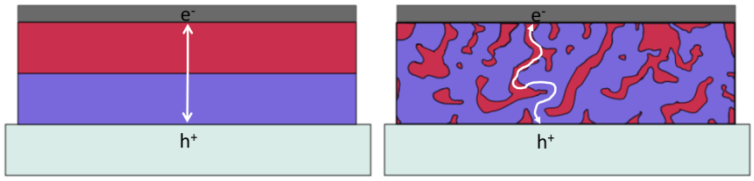

Figure 1.6: Schematic illustration of a bilayer (left) and BHJ (right) device architecture, with the electron donating material (blue), electron accepting material (red) and the electrodes depicted at the top and bottom.

The light harvesting part of the device is also known as the photo-active layer and is usually 50-300 nm thick.[7] The domain size and morphology of the active layer is a critically important factor in determining BHJ device *PCE*.[30]

OPV device structures can be categorised as either *conventional* or *inverted*. In the conventional configuration the transparent substrate electrode is the hole extracting electrode, and in the inverted structure it is the electron extracting electrode. Inverted OPV systems yield comparable or higher efficiencies than their conventional counterparts and improved stability.[35]

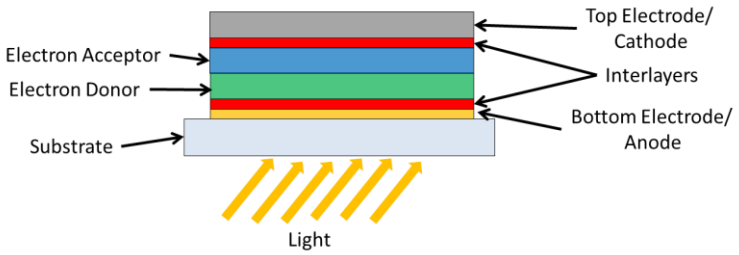

Figure 1.7: A conventional architecture bilayer OPV device with charge extraction interlayers (red). The electron extracting interlayer is in contact with the electron acceptor

(blue) and the opaque low work function top electrode. The hole extracting interlayer is in contact with the electron donor (green) and the bottom high work function window electrode.

OPVs also include charge extraction or buffer layers (Figure 1.7) which can perform a number of functions including (i) tuning the interfacial energetics to optimise the efficiency of free charge carrier extraction; (ii) enabling selective extraction of one charge carrier type; (iii) blocking diffusion of metal ions from the electrodes into the organic semiconductors;[36] (iv) acting as an optical spacer for enhanced light absorption; (v) blocking exciton quenching by the electrode;[37] (vi) improving the wetting and adhesion of the organic semiconductor layers;[36,38] (vii) reducing variations in work functions over an electrode surface; (viii) reducing surface roughness which can lead to devices short circuiting (Section 1.6.2). Modification of the work function of the electrodes to facilitate charge carrier extraction is often required because the Fermi levels of the hole and electron extracting electrodes are often poorly aligned with the frontier molecular orbitals from which they are supposed to extract charge.[39] Removing this mismatch minimises the potential energy losses incurred when extracting charge carries to the external circuit[40] (Figure 1.5). A barrier to charge carrier extraction at either electrode interface causes an S-shaped kink in the current voltage characteristic (Section 1.5.2).[41]

Interlayers can be inorganic or organic materials. For example, 2,9-dimethyl-4,7-diphenyl- 1,10-phenanthroline, commonly known as bathocuproine or BCP (Figure 1.8), is widely used as an electron extraction interlayer in OPVs. BCP works by blocking the extraction of holes because it has a very deep lying HOMO whilst allowing electrons to

reach the Al cathode. Gap states formed in the band gap of BCP upon Al deposition[42] enable electron extraction from the acceptor LUMO to the Al Fermi level. However, the reliance on the formation of these defect states limits the BCP thickness to 5-10 nm[43] and so it cannot be used as an optical spacer. BCP also has a tendency to crystallise and the crystallite grain boundaries trap electrons, thus affecting device lifetimes.

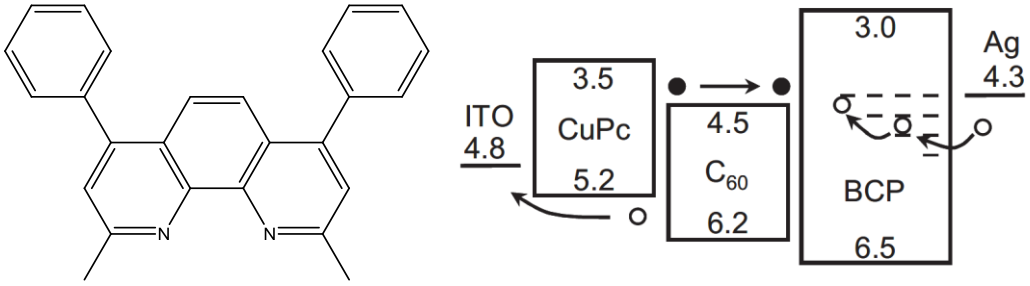

Figure 1.8: The chemical structure of BCP (left) and its flat band schematic energy level diagram depicting how gap states formed in the BCP layer upon Al deposition enable electron extraction (right).[42]

Transition metal oxides are often used in OPVs as interlayers between the photoactive layer and one of the electrodes to improve device *PCE* and stability. The thickness of this oxide layer is of importance as too low a thickness may give incomplete coverage, and too high thickness becomes too insulating, leading to excessive device series resistance.[40] Transition metal oxides have the advantage of having a wide range of work functions from zirconium oxide (~2.0 eV) to vanadium oxide (~7.0 eV) and can be broadly categorised as either low work function (e.g. ZnO, TiO_2) or high work function (e.g. WO_3, MoO_3, NiOx) serving as either electron or hole extraction materials. Metal oxides are discussed in more detail in Section 1.10. If the electrode Fermi levels are not

aligned to the appropriate energy level in the active layers, barriers to charge extraction can result, which lower device *PCE*.[44]

1.5.2. Device Parameters and Characteristics

Typical current density-voltage and power plots for an OPV device are pictured in Figure 1.9.

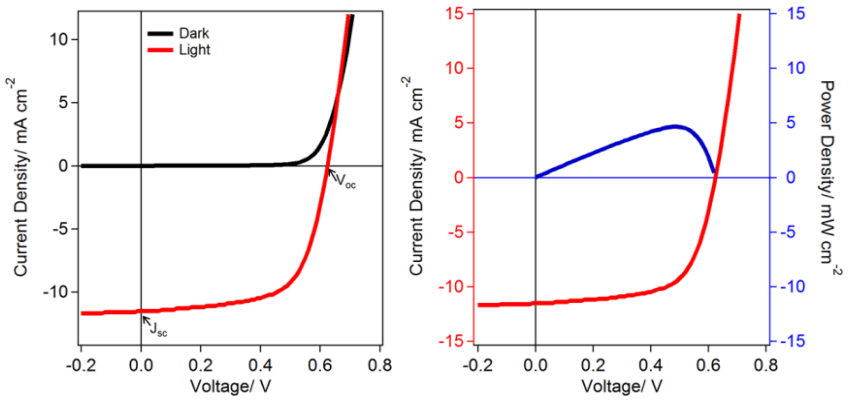

Figure 1.9: Current density / voltage characteristic (left) for an OPV in the dark and light (100 mW cm^{-2}) and current density / voltage characteristic showing the maximum power point (right).

Important figures of merit when testing PV devices are the short circuit current density (J_{sc}), the open circuit voltage (V_{oc}), the fill factor (*FF*) and the power conversion efficiency (*PCE*). J_{sc} is the current density produced by the cell under one sun illumination when the device is in short circuit, i.e. the electrodes are connected with zero resistance. This is illustrated in Figure 1.9 where the light curve (red) intersects the current density axis. The V_{oc} is the potential difference across the device when the electrodes are not connected, or connected with an infinitely large resistance between them. The V_{oc} corresponds to where the light curve intersects the voltage axis. The maximum obtainable V_{oc} in an OPV device is given by the difference in energy between

the HOMO of the electron donor and LUMO of the electron acceptor. The *FF* is the ratio of the maximum power generated in the device, to the maximum power calculated from the product of the J_{sc} and V_{oc}, as shown in Equation 1.1, and is therefore a measure of the "squareness" of the *JV* characteristic. The product $J_{MPP}V_{MPP}$, is the maximum power generated in the device, also known as the maximum power point (M_{PP}). The maximum verified fill factors for OPV cells are ~0.8, which is close to the theoretical limit.[45]

$$FF = \frac{J_{MPP}V_{MPP}}{J_{SC}V_{OC}} \qquad \textbf{Equation 1.1}$$

The *PCE* of a device is the ratio of power generated per unit area to the incident light energy density. This is shown in Equation 1.2:

$$PCE = \frac{J_{MPP}V_{MPP}}{P_{inc}} = \frac{J_{SC}V_{OC}\,\mathrm{FF}}{P_{inc}} \qquad \textbf{Equation 1.2}$$

The equivalent circuit diagram for a PV device is shown in Figure 1.10.

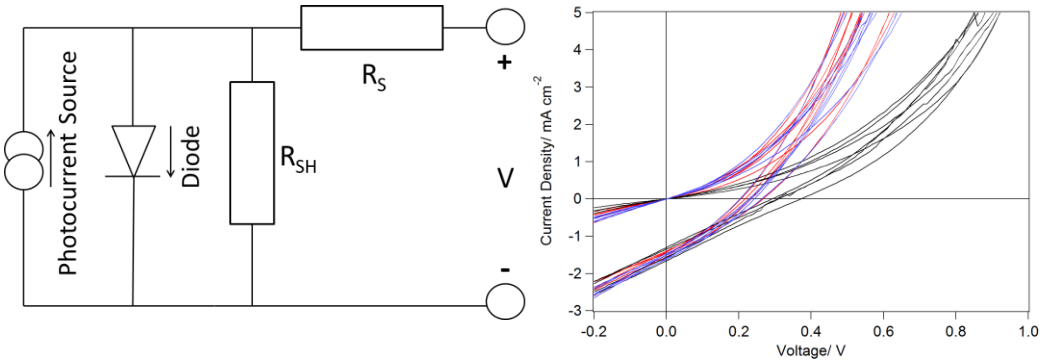

Figure 1.10: Left: Equivalent circuit diagram for a PV, showing the photocurrent source, diode, series resistance (R_S) and shunt resistance (R_{SHUNT}). Right: Current density / voltage characteristic for OPVs with a high series resistance and a poor *PCE*.

The R_S in a PV device can be determined from the inverse of the gradient of the *JV* characteristic in the light. In the example shown in Figure 1.10, the R_S is large. A high

R_S inhibits the extraction of charges and so reduces the fill factor and *PCE* of devices. The R_S is a function of the resistance to charge transport through each layer and the contact resistance at the interface between each layer. R_{SHUNT} is the resistance parallel to the load and determines the gradient of the *JV* curve where it crosses the *y*-axis. Ideally, the series resistance (R_S) is zero and the shunt resistance (R_{SHUNT}) is infinitely large.

The conductivity of the transparent electrode is invariably much lower than that of the opaque electrode in an OPV and so the sheet resistance of the transparent electrode can affect the R_S of the whole device to a large extent. The influence of the sheet resistance of electrodes becomes more important as the area of the device increases. For OPVs using a transparent electrode with a sheet resistance of 14 Ω sq^{-1}, this sheet resistance is the main contribution to loss of J_{sc} and *FF* when OPV devices are scaled up from 0.13 to 7 cm^2.[46]

1.6 OPV stability

Stability in addition to *PCE*, is a key factor for the future potential of OPVs,[47] and it has been outlined as one of the bottlenecks to OPV commercialisation.[48] There are many different degradation mechanisms for OPV cells, related to a variety of different processes including chemical oxidation,[49] water ingress,[50] oxygen doping,[51] and phase separation in the BHJ layer.[52] The specific mechanisms of OPV device degradation are the topic of much research, and a few examples relevant to this thesis are discussed below.

Water and oxygen have been shown to diffuse along grain boundaries and through pinholes in evaporated metal top contacts into the organic semiconductor layers where it participates in oxidation reactions, leading to device degradation.[49] It has been suggested that oxidation of the metal electrodes in organic electronic devices increases

the possibility of delamination between the electrode and organic layers due to the volume increase upon conversion of the metal to its oxide.[50] The oxide layer created during this process also typically has a much higher resistance than the metal and so charge extraction to the external circuit is hindered if this layer becomes thicker than 1-2 nm. This issue is most prevalent for low work function metal electrodes such as Ca and Mg which are most susceptible to oxidation.[53] Despite the fact that most of the top performing polymeric OPVs are very sensitive to air and moisture,[54] OPV cells based on a PCDTBT donor layer have been shown to have a lifetime approaching 7 years.[55] An interesting example of where oxidation of the electrode is not detrimental to device stability is the oxidation of Ag electrodes in OPVs when used for hole extraction. Here the very thin oxide layer changes the work function of the electrode, improving alignment between the donor HOMO and electrode Fermi level.[56]

Water ingress is a particular problem,[49] since as little as 10 mg m^{-2} of water can degrade some OPV devices by 50% of their initial efficiency,[47] and encapsulation and barrier materials are therefore required for sufficient stability of OPV cells to yield commercially viable lifetimes.[49] Effective encapsulation strategies are available but expensive, which undermines the cost advantages of OPVs. The materials used in OPV cells not only affect their stability but also their efficiency and cost, and will therefore be discussed in Section 1.7.

1.7 OPV materials

Materials for OPVs can be deposited either from solution (e.g. spin coating) or by thermal evaporation under vacuum, with many of the processes taken from the more mature OLED industry.[53]

Solution processing is the lowest cost deposition method due to low energy input, low temperature processing and speed of processing.[18,57] Solution processing also enables fabrication of OPVs with the lowest embodied energy. However, fabricating bilayer OPVs from solution is problematic and although OPVs have been fabricated using solution processing for every layer[54] the previous layer's solubility often causes issues, with efficiency values remaining low. Thermal evaporation under vacuum, although not as low energy as solution based techniques, is a widely used deposition method in the electronics industry,[28] and is already used in large scale manufacturing. Thermal evaporation under vacuum also offers much greater control over layer thickness particularly for very thin layers. In practical terms this means vacuum processing is usually required for some of the layers of an OPV despite being a higher energy deposition method.

Many different factors must be considered when screening new materials for PV applications, in addition to their compatibility with particular fabrication processes. The costs involved in chemical manufacture and material purity are an important consideration, for example 2,2(,7,7(-tetrakis-(N,N-di-pmethoxyphenylamine)9,9(-spirobifluorene (spiro-OMeTAD), is a material often used in DSSCs, although it is ten times more expensive than Au,[6] which may reduce the viability of commercialisation. It has also been shown that a complex polymeric material with a multi-step synthesis will contribute more to the cost per module or cost per Watt than a simpler material, like the archetypal polymeric donor material Poly(3-hexylthiophene-2,5-diyl) (P3HT), which has only 3 synthetic steps. However, economies of scale may alleviate this somewhat if these materials are put into mass production.[58]

OPVs are essentially multi-layer devices, and the different layers can be broadly split according to their functions in the device. They can be categorised as the substrate, the window electrode material, the electron donor material, the electron acceptor material, the hole transport material, the electron transport material, the top electrode material and electrode modifying layers (Figure 1.11).

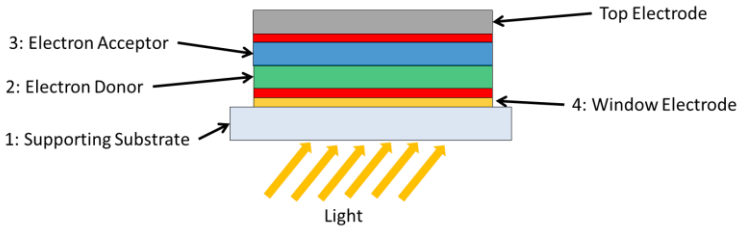

Figure 1.11: A conventional architecture bilayer OPV device schematic. The supporting substrate (light grey), electron acceptor (blue), electron donor (green), and the bottom window electrode (yellow) are highlighted.

1.7.1- Material 1- Supporting Substrate

For a supporting substrate, the requirements are for it to be highly transparent, inexpensive and for it to be able to act as a barrier to water and oxygen ingress into the device. For the supporting substrate to be compatible with high speed roll-to-roll processing it also needs to be flexible.

The archetypal substrate is glass with other common substrate materials being polyethylene terephthalate (PET) and polyethylene naphthalate (PEN) (Figure 1.12). The advantages of PET and PEN are their flexibility, low weight and low cost. PET also absorbs light strongly below 320 nm[59] which is advantageous for OPVs because UV light can bleach organic semiconductors. The use of these plastics also enables the realisation of roll-to-roll printing of OPVs. Plastic substrates like PET and PEN do however have

disadvantages, since some PET substrates cannot withstand temperatures higher than 170 °C[59] and both materials are slightly permeable to water.

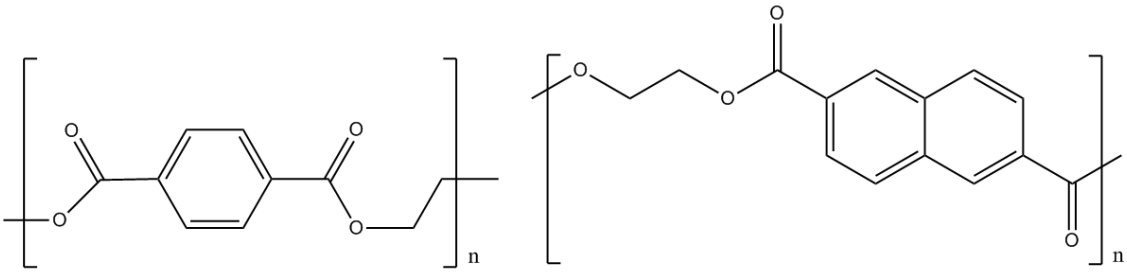

Figure 1.12: The chemical structure of PET (left) and PEN (right).

The window electrode in a conventional OPV architecture (Figure 1.11) allows light into the device and extracts photo-generated holes during device illumination. Window electrode materials will be discussed in detail in Section 1.8.

1.7.2- Material 2- Electron Donor Material

In a conventional OPV architecture, the electron donor material is the organic semiconductor closest to the window electrode (Figure 1.11). These materials can be polymeric or small molecule organic semiconductors. Donor polymers for BHJs must exhibit efficient absorption in the solar spectrum, have a high hole mobility, good solubility in solvents and favourable phase separation properties when combined with fullerenes. The frontier orbitals must also be of the right energy to function as an electron donor and ensure a high V_{oc}.[60] The thermal stability of polymeric OPVs has been shown to depend on the glass transition temperature of the donor polymer.[48] The molecular weight and length of side chains can also drastically affect the *PCE* of an OPV.[61] The side chains of the polymer not only impart solubility, but also affect the morphology and optical density of the film. The regio-regularity of polymeric OPV systems can have

profound effects on the device *PCE* as can the drying time, with longer drying times yielding more crystalline films.

The two polymeric donor materials used in this work; PCDTBT and PTB7, are shown in Figure 1.13.

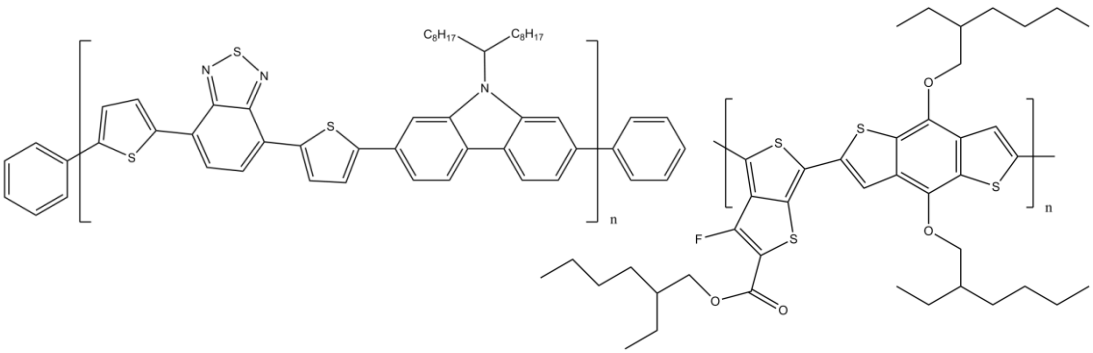

Figure 1.13: The chemical structures of PCDTBT (left) and PTB7 (right), two polymeric donor materials used in this work.

PTB7 is a donor material which when used in conjunction with fullerene electron acceptor materials, and can yield OPVs with *PCE*s of 7-9%.[35,60,62,63] The PCDTBT/$PC_{70}BM$ system can yield devices with *PCE*s of over 6%,[63] and other donor polymer systems are also available with similar efficiencies, for example the PDTSTPD/$PC_{70}BM$ BHJ system, which yields devices with *PCE*s of over 7%.[64] The high *PCE* of the PTB7 system is due in part to its high absorption over the whole visible spectrum (Figure 1.14). PTB7 has an ionisation potential and electron affinity of ~5.2 and ~3.3 eV respectively.[35] The addition of a low volume percentage of diiodooctane to the dichlorobenzene solvent used to process the PTB7/$PC_{70}BM$ shrinks the domain size of pure fullerene regions, resulting in greatly increased efficiency due to a larger domain interface.[34,65]

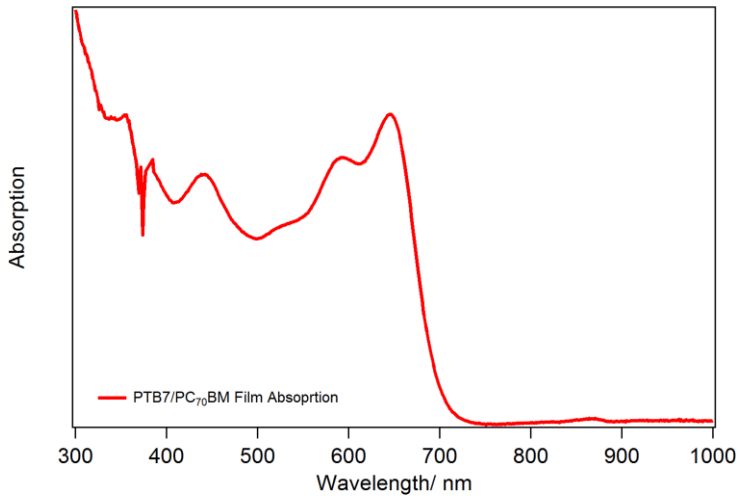

Figure 1.14: Absorption spectrum of a thin spin cast PTB7/ $PC_{70}BM$ film.

Unfortunately, PTB7 is reported to be 200 times more unstable than another widely studied donor polymeric material (DPP-TT-T) under constant illumination in an oxygen atmosphere,[66] although this fast degradation is not observed in the absence of oxygen.

Small molecule organic donor materials are required to have many of the same characteristics as polymeric donor materials, with the obvious exception of solubility. They must also be amenable to evaporation at high vacuum without decomposing upon heating. Phthalocyanines for example, have poor solubility in organic solvents, but very favourable chemical and thermal stability and have been used industrially for many years as dyes. The large conjugated heteroaromatic ring system imparts their semiconducting properties and renders them brightly coloured. Two of the small molecule donor materials used in this work; chloroaluminium phthalocyanine (ClAlPc) and pentacene, are shown in Figure 1.15.

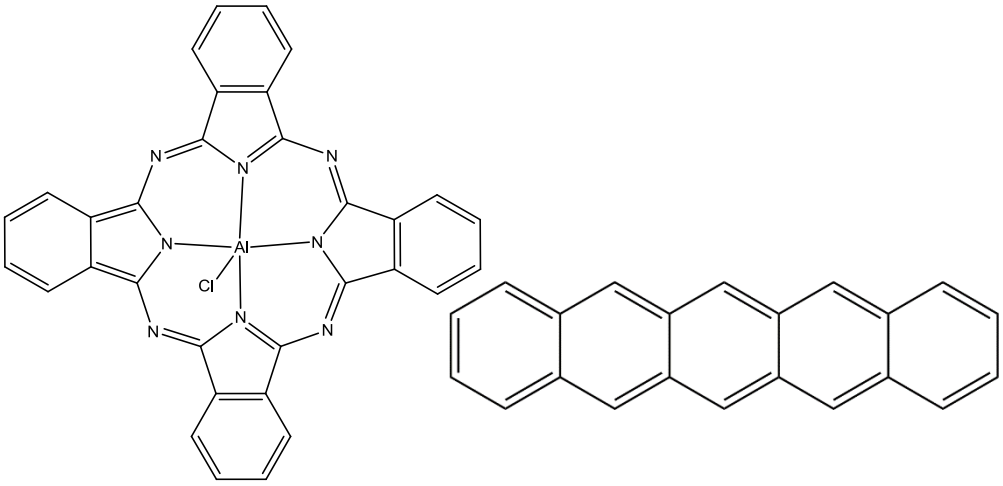

Figure 1.15: The chemical structures of ClAlPc (left) and pentacene (right).

Pentacene is a commonly used electron donor material in OPV devices. It offers the advantageous properties of high hole mobility, ease of vacuum evaporation, good optical absorption and large exciton diffusion lengths. However, it is also easily oxidised, affecting its stability in OPVs.

An ideal organic photo-active layer material absorbs strongly over a wide range of wavelengths between 400-900 nm which is the part of the solar spectrum of most use for PV.[35] Whilst many organic semiconductors absorb light strongly below 400 nm, the photon flux is low in that region of the solar spectrum (Figure 1.4). OPV cells often use sub-cells with different band gaps, to maximise absorption across the whole of the solar spectrum.[30,67,68] Organic small molecules typically absorb over relatively narrow wavelength ranges (Figure 1.16), so to ensure that OPV devices function efficiently the donor and acceptor materials are chosen to ensure that they absorb in complementary parts of the solar spectrum.

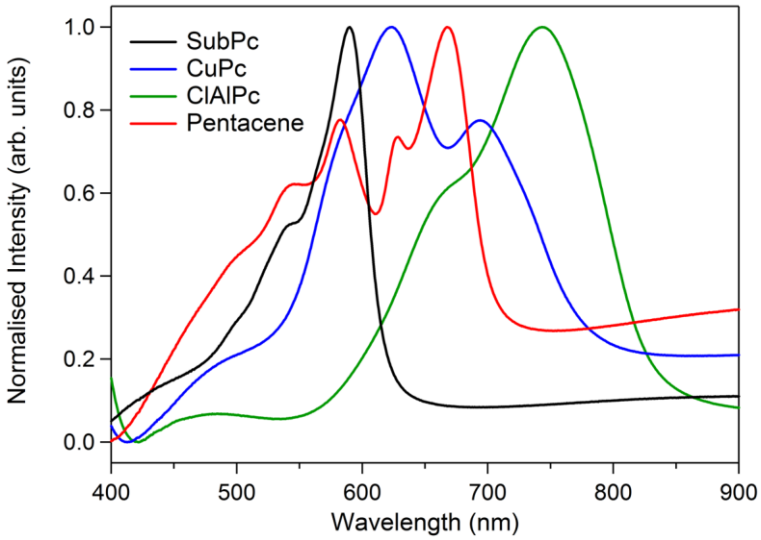

Figure 1.16: Normalized absorption spectra for thin films of four commonly used small molecule organic donor materials: SubPc, CuPc, ClAlPc and Pentacene.[69]

1.7.3- Material 3- Electron Acceptor Material

In an OPV, the electron accepting material accepts electrons and transports holes to the electron donor material. The fullerenes shown in Figure 1.17 are often used as electron acceptors for OPV due to their high electron affinities, high electron mobilities, good exciton diffusion lengths and absorption in the green region of the visible spectrum. Each carbon in the C_{60} molecule is sp^2 hybridised, with each atom forming one double and two single bonds. Both PCBM and C_{60} undergo photo-induced polymerisation reactions upon exposure to UV light which is not detrimental to device performance.[70-72]

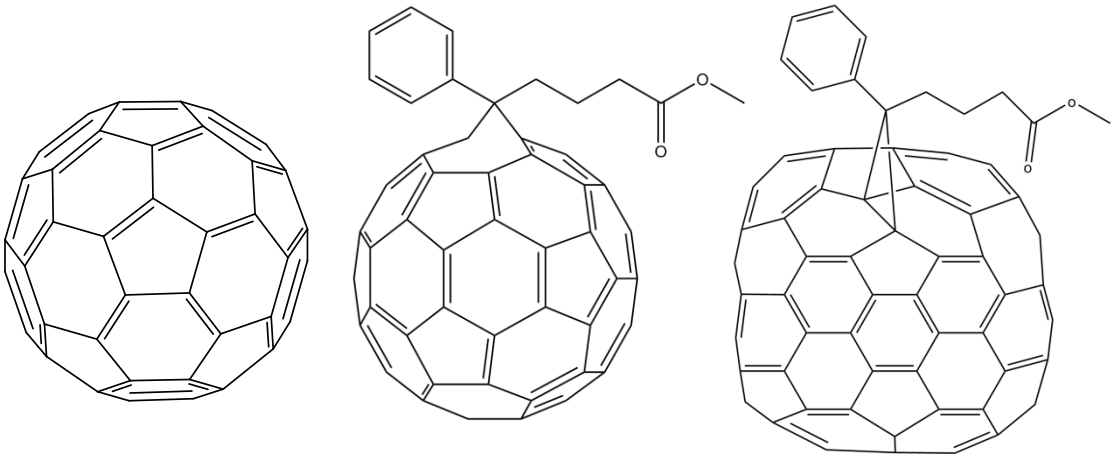

Figure 1.17: The chemical structures three common acceptor materials C_{60} (left), PCBM (middle) and $PC_{70}BM$ (right).

C_{70} is another fullerene that can be used as a small molecule electron acceptor in bilayer OPV devices. It has been shown to yield increased *PCE* in OPV cells when compared to devices using C_{60} due to increased absorption and improved electron transport. C_{70} based OPV are also found to be more stable,[73] although C_{70} is much more expensive to produce than C_{60}.[74] C_{60} and C_{70} are often derivatised to ensure solubility in organic solvents for more facile processing (e.g. PCBM and $PC_{70}BM$, Figure 1.17).[70] As such, C_{60} is usually used as the electron acceptor in evaporated small molecule OPVs, with PCBM or $PC_{70}BM$ used in the solution processed BHJ OPVs. Polymeric acceptors are less commonly used in OPVs because they often undergo large scale phase segregation when blended with donor polymers, and consequently yield relatively poor efficiencies in OPV devices.[75]

Al and Ca are the most commonly used materials for the top opaque electrode due to their low work functions and relatively high reflectivity; they are not discussed in

depth here, although it is worthy to note that their main issue is susceptibility to oxidation.

1.8 Window Electrodes for OPV

The core issue with transparent electrodes for OPVs is that the free electrons that impart conductivity also interact strongly with light, reducing the transparency of the electrode. Window electrodes for OPV devices must therefore be designed with this fundamental problem in mind, as an increase in the conductivity of an electrode will often decrease its transparency and vice versa; consequently a compromise must be achieved.

Window electrodes in OPV devices need to fulfil three important criteria. They need to be optically transparent to let light into the device, electrically conductive to allow the extraction of photogenerated charge carriers, and finally not so rough as to undermine device shunt resistance due to filamentary short formation.[76,77] The surface energy, work function, cost, flexibility and long term stability are also important factors for electrode materials for OPV fabrication. The chemical stability of electrode materials is of importance, as PV modules are exposed to the elements and to significant heating in sunlight, which can raise the temperature to values as high as 60 °C.[78] A low surface roughness is required due to the very thin active layer thicknesses utilised in OPV devices. In practice, the window electrode RMS roughness needs to be $\leq$ 2 nms. The window electrode material also has to be transparent right out to wavelengths of 950 nm, to ensure the maximum amount of the solar spectrum is harvested. An electrode's transmission spectrum must be carefully considered, since for an OPV a low transparency in the ultra-violet part of the solar spectrum can be advantageous, as many organic semiconductors are degraded by UV light.[26]

An OPV's series resistance (or internal cell resistance) can affect the efficiency of the device drastically. The electrical conductivity of window electrodes is quantified in terms of sheet resistance. A window electrode for an OPV must have a sheet resistance of $\leq 10\ \Omega\ sq^{-1}$ to ensure that a large drop in *PCE* is not observed when OPV cells are scaled up to a large cell area for applications.[46,79] These losses can be mitigated by using transparent electrodes with higher conductivity.[80] Thus highly conductive transparent electrode materials are a prerequisite for the realisation of OPV technology industrially.

The leading window electrode materials for OPV are doped metal oxides, as they provide a good compromise between transparency and sheet resistance. The metal oxides utilised have wide band gaps and therefore offer a high degree of optical transparency. These metal oxides are degenerately *n*-doped to increase the conductivity by orders of magnitude. This doping can often be in concentrations as high as 10 atomic %. Figure 1.18 illustrates this for the most commonly used OPV window electrode material, indium-tin oxide (ITO) coated glass. The doping of the material preserves its wide band gap whilst greatly increasing the conductivity as compared to the undoped state.

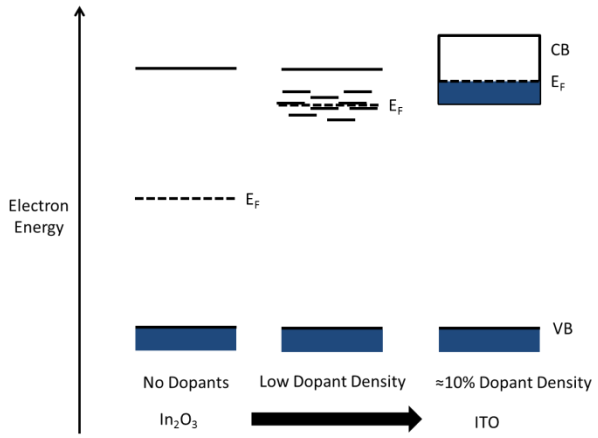

Figure 1.18: Energy level diagram for the doping of indium oxide to create ITO.

ITO glass used for OPVs has a sheet resistance of 6-15 Ω sq^{-1} and a transparency of 75-95% over the visible spectrum. ITO's transparency and sheet resistance are a function of the thickness; the sheet resistance and transparency decrease as the film thickness is increased, with considerably lower transparencies at 6 Ω sq^{-1} (sheet resistance suitable for application in OPVs) compared to the 15 Ω sq^{-1} normally used in small area OPVs as shown in Figure 1.19.

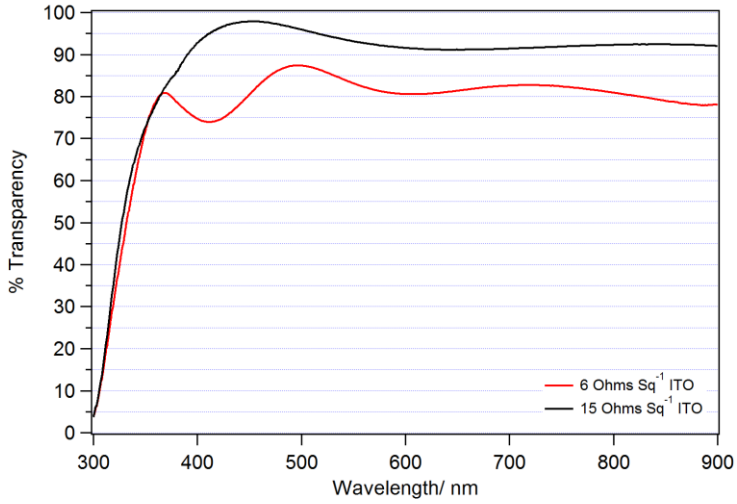

Figure 1.19: Far-field transparency spectra of ITO glass at 6 Ω sq^{-1} (red) and 15 Ω sq^{-1} (black).

ITO does however have a number of drawbacks for applications in OPVs which are discussed in Section 1.9.

1.9 ITO Problems

ITO coated glass is long established as the window electrode of choice for many applications including displays, heat reflective glass and solid-state lighting including OLEDs, where it is the industry standard.[81] It is also the archetypal window electrode material for OPVs, typically at a thickness of ~80 nm.[82] Indium is produced mostly as a by-product of zinc mining from ores with an indium content of only 1-100 ppm.[83,84] The

scarcity of indium in the earth's crust and the proliferation of flat screen displays mean that indium and consequently ITO are expensive.[57]

There are also other problems with ITO glass for utility in OPVs: It has been shown to account for 50-74% of the embodied energy in an OPV device,[19,28] and its sheet resistance (≈15 Ω sq^{-1}) has been found to be a limiting factor for the *PCE* of OPVs sufficiently large for practical applications.[46,85,86] ITO is also meta-stable and is typically deposited at temperatures above 250 °C to ensure optimum performance which makes it poorly matched to the plastic substrates required for high speed roll-to-roll manufacture of OPVs. When ITO films on plastic substrates are bent, cracks being to appear since ITO is inherently brittle, resulting in much higher sheet resistance values.[87] This is not the case with ultra-thin metal films.[85,86] The sheet resistance of ITO on flexible substrates varies, but is invariably >35 Ω sq^{-1}.[85-87] Indium and tin have also been shown to diffuse into the organic layers in OPVs.[88] It is for these reasons that ITO has been described in the literature as not a possible choice for scalable OPV.[7]

1.10 ITO Alternatives

It is widely recognized that the full cost advantage of OPVs over commercial silicon and thin film photovoltaics can only be achieved if the electrode that couples light into the device is based on inexpensive raw materials, involves simple, rapid fabrication processes and is compatible with substrates that are sufficiently flexible for roll-to-roll fabrication of devices.[17,18,57] Due to the aforementioned issues many alternatives to ITO have been proposed, some of which are described individually below. However, no clear leader has yet emerged, since all of these alternative window electrodes have significant disadvantages for application in OPVs including environmental concerns over the

materials, high surface roughness which increases the likelihood of parasitic current shunting in a PV cell,[76,77] or too high sheet resistance.[76]

1.10.1 Alternative Oxides

There has been significant research into other doped metal oxides, including indium titanium oxide,[83,89] and fluorine doped tin oxide (FTO).[89] FTO is not often used in OPV cells as it has large surface roughness as compared to ITO glass.[89] This is not an issue for DSSCs, where it is ubiquitous. Other metal oxides can possibly overcome some of the issues associated with ITO, but not all of them as these materials will always be used in films of 100s of nms in order to be sufficiently conductive for OPVs and will therefore still be liable to crack upon bending. As these materials cannot be compatible with flexible substrates, other alternatives must be sought for OPV.

1.10.2 Carbon Based Nanomaterials

The two main carbon based ITO alternatives are carbon nanotubes and graphene films. Carbon nanotubes can produce films with comparable transparency to ITO glass. However, the sheet resistance of these films is not low enough for large scale OPV.[90] The production methods for carbon nanotubes are also very energy intensive, and carbon nanotube electrodes are intrinsically very rough, which is not ideal for OPVs.

Graphene monolayer and multilayer graphene are also being investigated as potential transparent electrodes for OPV.[91] Whilst graphene electrodes appear theoretically tantalising, particularly once doped, high sheet resistance values of $\approx 200\ \Omega\ sq^{-1}$ at ≈ 80% transparency for fabricated films prohibit the use of graphene for OPVs, where $\approx 10\ \Omega\ sq^{-1}$ is required.[90] This problem is demonstrated by many of the devices currently reported in the literature that have significantly lower *PCE*s than the

analogous ITO based devices.[91] Graphene production methods are also energy intensive and costly currently.

1.10.3 Conducting Polymers

Conductive polymers have undergone research as a material to replace ITO, however they are too resistive to be used as a stand-alone replacement.[92]

1.10.4 Metal Nanowires

Metal nanowires have been suggested for replacement of ITO, including Cu nanowires.[93] Metallic nanowires can be solution processed and have impressively low sheet resistance and high transparency values.[94] However, these electrodes have high RMS roughness, which can cause shorting of the thin active layers in an OPV and have to be combined with conductive polymers to smooth their surface.

1.10.5 Metal Grids

Solution processed silver grid electrodes for OPVs have received significant attention[17] in recent years. Evaporated metal grid electrodes have been achieved with sheet resistance values as low as 2 Ω sq^{-1} at 90% transmission, which compares very favourably to ITO.[95] This was achieved by electrospinning polymer fibres and then evaporating, or sputtering electrode materials on top of them. The polymer grid is then dissolved using solvents.[95] Whilst these values for transmission and sheet resistance are impressive, the metal troughs are ≈80 nm high, which is comparable to the thickness of the semiconducting layer in an OPV and shorting of devices is likely. It has been reported that for large area printed OPVs fabricated on metal grid electrodes with comparable roughness, the short circuiting of devices is an issue.[96] The complexity of the fabrication process may also limit the applicability.

1.10.6 Ultra-thin metal films

In recent years there has been renewed interest in both planar[59,86] and patterned[97] ultra-thin (<10 nm) metal films, as they provide both ideal model electrodes for laboratory testing and offer the prospect of replacing ITO glass electrodes in OPVs. Issues with robustness, transparency and resistivity have prevented the widespread utilisation, as films of the most conductive metals are typically discontinuous at a thickness low enough to be highly transparent. In principle, ultra-thin metal films could yield the required characteristics to replace ITO films, although this has not yet been realised. Metals often employed for this purpose include Au, Ag and Cu. Au is often used for laboratory use, but may be too costly to implement on a large scale. Ag has the advantages of the highest conductivity amongst metals and a low refractive index in the visible region.[98] However, both Au and Ag are expensive. Cu is relatively inexpensive; about 100 times cheaper than Ag and 5000 times cheaper than Au.[93] Cu is already widely used in the electronics industry.[98] It has comparable conductivity to Ag, and better conductivity than Al or Au.[96] The primary obstacle to the use of Cu is the susceptibility to oxidation, which in the context of an ultra-thin film is a serious problem.

Many ultra-thin metal films have been fabricated for use as electrodes in organic electronics. These include both planar and nanostructured Au, Ag and Cu electrodes,[86,97] Ag/Cu bilayers,[98] and Ag electrodes seeded with Cu.[98] If metal films are too thin, (i.e. below the percolation thickness) they will remain as discontinuous island like structures, causing scattering and a reduced transparency, and an increased sheet resistance.[99] The percolation thickness will vary depending on the metal, the deposition method and the substrate, but a typical percolation thickness is 6-7 nm for Ag on PET.[59]

Finally, it is important to note that reduced transparency of the window electrode in an OPV does not always lead to a reduced absorption in the organic semiconductor. The increased reflection can create a resonant cavity between the window and back electrodes, resulting in increased light harvesting.[82,85]

Metal oxides are useful in OPV devices as charge extraction interlayers, but also useful for refractive index matching, thus improving ultra-thin metal film transparencies. They will be discussed in Section 1.12.

1.12 Metal Oxides in OPVs

Metal oxide charge extraction layers are often used in OPVs between the electrodes and the photo-active layer to improve device *PCE* and lifetimes. Metal oxides with low work functions (e.g. ZnO, TiO_2) and high work functions (e.g. WO_3, MoO_3, NiOx) are available, with some having n-type (e.g. ZnO) and some having p-type (e.g. NiOx) characteristics due to intrinsic defects. High work function metal oxides are used as hole extracting interlayers in OPVs, and low work function oxides are used as electron extracting interlayers in which context they serve to improve alignment between the electrode Fermi level and the relevant frontier molecular orbital in the adjacent organic semiconductor as illustrated in Figure 1.20. Consequently when these oxides are used in an OPV they typically increase the built in field across the organic layers, resulting in a higher V_{oc} and more efficient charge carrier extraction.[100]

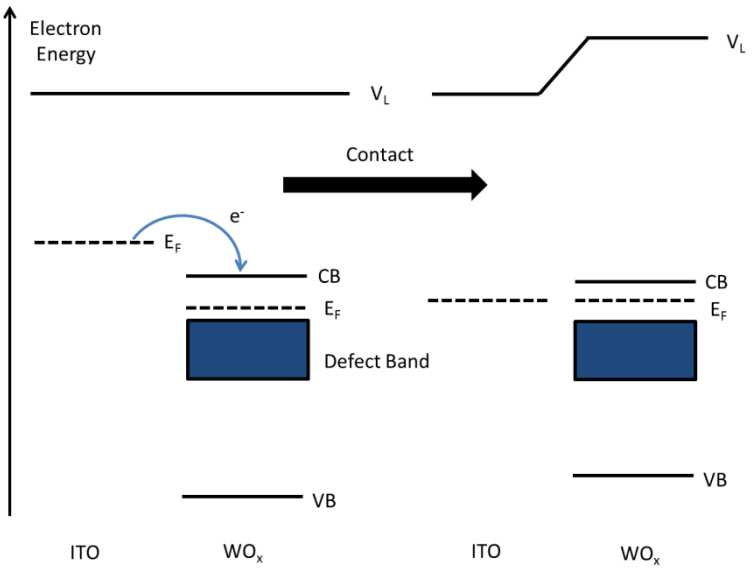

Figure 1.20: Energy level diagram depicting Fermi level alignment at the interface between ITO and WO_x.

Metal oxides can be vacuum or solution processed and the chemical potential can be tuned by altering the amount of oxidation via changes to its deposition method, thus changing the work function.[101] Introducing more oxygen defects into the structure reduces its chemical potential and work function, since the oxygen defects serve as n type dopants.[102] Metal contacts can affect an oxide's chemical and electronic properties within the first few nms of the contact, as a result of charge transfer or doping of the oxide by the metal.[102] For example, MoO_3 becomes semi-metallic near contacts, reducing the work function for films less than 10 nm.[102] Interfacial chemical reactions between metal oxides and organics have been shown to reduce charge transport barriers across interfaces,[103] and so metal oxides have widely used in organic electronics.[104]

Metal oxides are also used as optical spacers in OPVs to maximise light absorption.[101] These optical spacer layers must be both optically transparent and have a

large charge carrier mobility, with materials like aluminium doped zinc oxide and titanium dioxide often being used. Optical spacer layers maximise the light intensity in certain areas of the cell, and so can be used to improve the short circuit current. They are also used to prevent diffusion metal ions from the ITO electrode in OPVs.[105]

Tungsten trioxide (WO_3) is a metal oxide that is widely used in electrochromic devices, since its transparency is altered drastically when ions are injected into the material.[106] Typically Li, Na or H are used as dopants in WO_{3-x} in photochromic devices. Cu can also be used,[32] although Cu doped WO_{3-x} has not been utilized previously in OPVs as a charge extraction material. The photochromic properties of Cu doped tungsten oxide are very complex and not completely understood by the scientific community.[107] Copper has also been shown to alloy with MoO_3 and diffuse through MoO_3 films. [102] This diffusion of Cu into metal oxides has been previously viewed as an issue.[108]

Thin films of stoichiometric WO_3 are transparent to most visible wavelengths with a slightly yellow tint for very thin films,[109] and a yellow/green colour in the bulk.[107] The transparency of tungsten oxide has been shown to change upon UV irradiation.[107] The band gap depends on the crystallinity of the sample, and ranges from 2.6-3.3eV.[109,110] Evaporated WO_3 has a work function of 6.5 eV, an electron affinity of 6.7 eV and an ionisation potential of 9.8 eV,[111] although the work function has been reported to be as low as 4.9eV.[99] The chemical, electronic and optical properties of tungsten oxide films can vary hugely with different deposition techniques.[112] Tungsten oxide has been used in OPVs to increase the transparency of ultra-thin metal films[87] and is suited for this role due to its high refractive index.[109] However, if the tungsten oxide interlayers used are too thick, the series resistance of the device increases, and this leads to a reduced *PCE*, so a balance must be struck. [109]

MoO_3 has similar properties to WO_3, is widely used in OPVs as a hole transport layer, is highly n- type doped and facilitates charge transport via the conduction band.[113] With WO_3 having a very similar ionisation potential, work function and electron affinity to MoO_3,[113] its use as a hole transport layer is promising. It has been shown for MoO_3 that thick (≈100 nm) layers in devices inhibit performance, but this can be overcome by doping with metals.[114] This allows the use of thicker spacers layers to maximise absorption within an OPV device.

1.13 Plasmonics

In addition to metal oxides, another method of increasing the viability of ultra-thin metal films as window electrodes for OPVs is plasmon enhanced absorption, which will now be introduced.

Plasmonics is an active area of research for communications,[115] sensing,[116] and more recently OLEDs[117] and PVs.[118] A surface plasmon resonance (SPR) is the resonant response of free electrons in a conductor to incident light. This can be a local effect confined to a nanoparticle, or aperture in a metal film, known as a localised surface plasmon resonance (LSPR), or a propagating excitation known as a surface plasmon polariton (SPP). These surface excitations result in a strong enhancement of the local optical field. A schematic illustration of the excitation of LSPRs in a metal nanoparticle is shown in Figure 1.21. The nanoparticle diameter is much smaller than the wavelength of the incident light and the free electrons in the nanoparticle oscillate with the change of phase of the incident light.

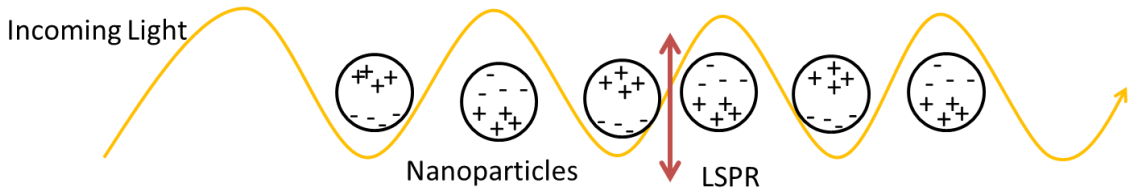

Figure 1.21: LSPR induced in nanoparticles by coupling with visible light.

Much like nanoparticles, sub-wavelength holes in a metal film couple strongly with incident light, exciting SPRs that are located at the site of the aperture. LSPRs associated with an aperture in a film can leak into the surrounding metal film forming propagating SPPs, as shown in Figure 1.22. This is an example of coupling between localised and propagating surface plasmonic excitations.

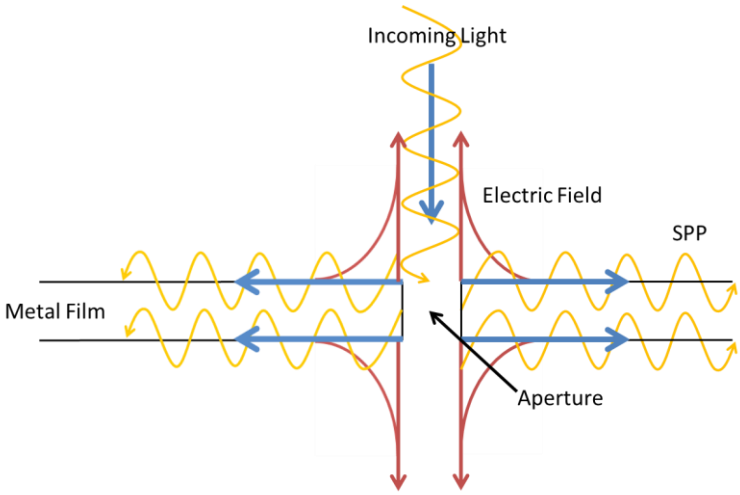

Figure 1.22: Light coupled into a metal film via an aperture.

The onset wavelengths for surface plasmon excitation in Ag, Au and Cu are ~320, 540 and 590 nm respectively;[115] and so the coinage metals are all plasmon active in the visible range and are therefore of interest for PV applications. For other metals this is

typically in the UV part of the spectrum. Plasmonic absorption at metal electrodes can cause optical losses, resulting in reduced transparency for ultra-thin metal films,[87] as incident light is converted into surface plasmon polaritons and is coupled into the film.[119] The addition of 2 nm of Al to Ag films can increase the transparency of the Ag films due to a suppression of surface plasmons in the visible region, because the surface plasmon frequency of Al is at 250-300 nm.[115] This is distinct from the approach applied to enable plasmon enhanced absorption used in this thesis. The amount of Ohmic losses that result from damping of the collective oscillation of conduction electrons in a metal film must also be considered when selecting a metal for a plasmonic application. Ag and Au are by far the most studied materials in the field of plasmonics due to their low Ohmic losses in the visible region. Cu has also been studied as a plasmonic material and has comparable Ohmic losses to Au, but is prone to oxidation,[115,120] with the LSPR frequency of Cu being highly dependent on surface oxidation. The propagation length of SPP at metal surfaces varies widely, and depends strongly on the surface roughness.[121] Cu would be advantageous for plasmonic applications due to its low cost, if similar performance to Au could be achieved.

The optical field intensity in the vicinity of an aperture or at the surface of a flat film is very high near to the SPR frequency and so if a semiconductor with a high absorption coefficient is next to the metal, then the energy can be used to form electron hole pairs in the semiconductor before the SPR dissipates its energy to Ohmic losses. Thus, for PV applications SPRs are useful because they provide a means of concentrating and confining the incident light into a small volume. This is particularly useful in the context of thin film PV where the thickness of the light harvesting semiconductor layer is typically much less than needed to absorb all the incident light. When confined at a

metal-semiconductor interface, the SPR is freely propagating in the plane of the interface and so can increase absorption of light in the semiconducting layer.[33] Plasmonic enhancement can be observed in OPVs using metal film electrodes with apertures smaller than the wavelength of the incident light.[122] Plasmonic excitations in ultra-thin metal films with sub-wavelength apertures are highly localised effects, with the decay length being comparable to the hole's radius,[123] which is usually of the order of 10's nm. This means that they are well suited for OPVs, as similar active layer thicknesses are used,[124] but are not effective in Si based PV technologies.

Metal nanoparticles can also be used in OPVs to achieve plasmon enhanced light absorption.[125,126] However, metal nanoparticle decorated electrodes for OPVs have a higher probability of shorting the device due to the highly increased roughness. This practical limitation does not exist when nano-structuring the window electrode using apertures, as these structures do not compromise the shunt resistance.

1.14 Project Overview

The work presented in this thesis is concerned with the use of ultra-thin Cu films as replacements for ITO as the transparent electrode in OPVs. There are no previous reports of these electrode configurations discussed in the 4 results chapters. Chapter 3 introduces the use of an ultra-thin Al layer to passivate ultra-thin Cu electrodes from oxidation. Chapter 4 increases the transparency of ultra-thin Cu electrodes through the use of a tungsten oxide overlayer. Chapter 5 attempts to combine the distinct approaches of Chapters 3 and 4 into a transparent and air stable electrode. Chapter 6 discusses a separate approach to increased photocurrent in flexible OPVs, via the use of plasmon active transparent electrodes. Chapter 7 summarises the work presented in this thesis and introduces further avenues of investigation.

Chapter 2 – Experimental Techniques

Summary

This chapter describes the methods and techniques for electrode and OPV device fabrication and characterisation used in this thesis.

2.1 Substrate Preparation

2.1.1 Substrate cutting and cleaning

Glass microscope slides (VWR Super Premium, 1.2 mm thick) were cut to size (typically 13×13 mm for OPV devices and 26 × 26 mm for electrode characterisation) using a diamond pen cutter. To thoroughly clean the slides they were then:

- ultra-sonically agitated for 15 minutes in acetone,
- dried under a stream of nitrogen,
- ultra-sonically agitated in a dilute aqueous solution of Decon Surfactant (Neutracon) for 15 minutes,
- ultra-sonically agitated in deionised water (>10 MΩ purity) for 15 minutes,
- removed and rinsed with water and iso-propanol (IPA),
- ultra-sonically agitated in IPA (HPLC grade) for 15 minutes,
- dried in a stream of nitrogen.

All ultra-sonic agitation was carried out in a Fisherbrand FB11002 ultrasonic bath at 100% power.

ITO glass slides were subject to the same cleaning procedure, with the insertion of an initial acetone rinsing step to remove a layer of photoresist as supplied. The ITO slides had a sheet resistance of 15 ± 3 Ω sq^{-1} and an ITO thickness of 145 ± 10 nm and were from Thin Film Devices Inc. The transparency of these films is shown in Figure 1.19.

PET slides were cut to size (typically 13×13 mm for OPV devices and 26 × 26 mm for electrode characterisation) from a large roll (Mitsubishi, Hostaphan GN 125 4600) using a scalpel. To thoroughly clean the slides, they were rinsed with acetone, IPA, deionised water, IPA, deionised water and IPA, and finally dried under a stream of nitrogen.

The far-field transparency of both the glass and PET slides is shown in Figure 2.1.

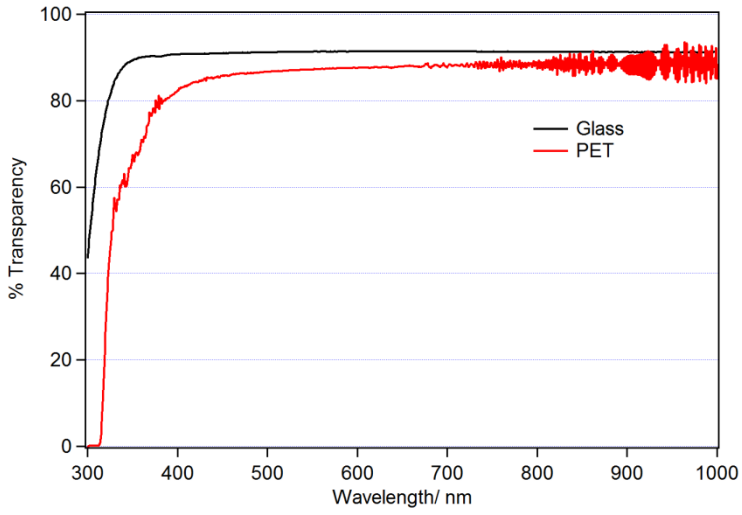

Figure 2.1: Far-field transparency spectra of the glass and PET substrates used in this work, referenced to air.

2.1.2 UV/O_3 treatment

After solvent cleaning, the substrates were UV/O_3 treated to remove solvent residue and other hydrocarbon contaminants adsorbed from the atmosphere. UV/O_3 treatment increases the surface energy of the substrate, which improves film wetting upon layer deposition. UV/O_3 treatment of electrodes (e.g. ITO glass) can also alter the work function.[127] The work function of ITO increases upon UV/O_3 treatment due to the formation of polar oxygen containing groups on the surface and the reduction of the push-back effect caused by organic contaminants, both of which modify the surface potential contribution to the work function.

Figure 2.2: The Novascan PSD-UVT UV/O_3 rig.

UV/O_3 treatment was carried out using a Novascan PSD-UVT UV/O_3 rig (Figure 2.2). This equipment uses a UV lamp (185 nm and 254 nm, 20 mW cm^{-2}) to generate ozone from atmospheric oxygen. Glass and ITO slides were UV/O_3 treated for 15 minutes with UV illumination followed by a further 15 minutes with the lamp off

unless otherwise stated. PET substrates were UV/O_3 treated for varying times between 0-5 minutes, with the lamp on.

2.2 Metal and Monolayer Deposition

2.2.1 Metal Evaporation

Metals were thermally evaporated at a rate of 1 $Å s^{-1}$, from tungsten boats (Testbourne Ltd) at a pressure of ~1×10^{-5} mbar. Material evaporation parameters and evaporation details are given in Table 2.1.

2.2.2 Self-assembled Monolayer (SAM) Deposition

SAMs can be used to engineer the interfaces in organic optoelectronic devices by modifying the surface energy and work function.[85,127] In this work, a mixed SAM of (3-aminopropyl)-trimethoxysilane (APTMS) and (3-mercaptopropyl)trimethoxysilane (MPTMS) (Figure 2.3) was used as a molecular adhesive layer in the fabrication of ultra-thin metal films on glass. This approach to ultra-thin metal film formation was initially developed for Au by the Hatton group and was applied to Cu films for the first time as part of this project. The methoxy groups on the silicon atom in APTMS and MPTMS form a strong siloxane bond to the glass surface, with methanol being released as a by-product.

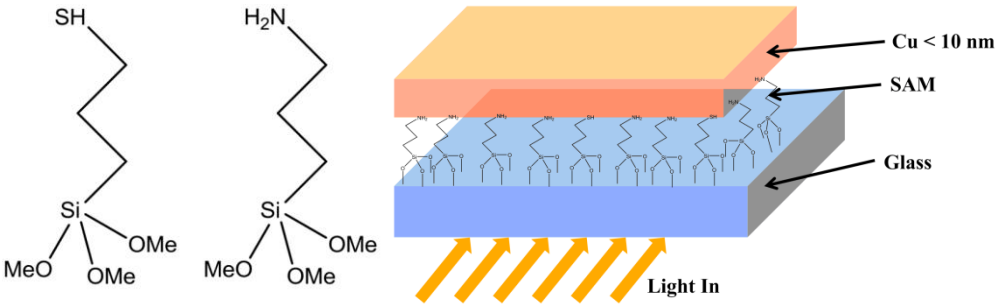

Figure 2.3: The chemical structures of MPTMS (left) and APTMS (middle), and a schematic showing their role as a molecular adhesive layer supporting an ultra-thin metal film.

The thiol and amine head groups on MPTMS and APTMS respectively bind strongly to the incoming Cu atoms during metal evaporation. The primary amine catalyses the coupling reaction between the methoxysilane groups and hydroxyl groups at the glass surface enabling the formation of dense, rapidly formed SAM and also binds to Cu. The thiol head group binds to Cu more strongly than the amine functional group, evident by the greater stability of nanoparticles capped with thiol ligands.[128] A mixed amine and thiol SAM combines the high density of the amine SAM with the stronger bonding interaction of the thiol SAM, producing a dense array of nucleation sites for metal film formation, and ensures that the film grows in a continuous manner with small crystallites that are strongly bound to the substrate at low thickness.[129] SAMs can therefore lower the percolation thickness of ultra-thin metal films, improving conductivity and transparency.[85] MPTMS and APTMS have been reported previously to be capable of supporting Cu films,[130-132] but not when used as a mixed monolayer.

Mixed SAMs (APTMS and MPTMS, 9 drops of each (97% Sigma Aldrich)) were deposited from the vapour phase at reduced pressure (~50 mbar of air) for 4 hours

unless otherwise stated. The vapour phase deposition method removes the need for solvent and ensures that polymerisation does not occur. All Cu electrodes on glass in this thesis are supported on this mixed molecular adhesive layer unless otherwise stated.

2.3 Substrate/ Electrode Characterisation

2.3.1 Sheet Resistance Measurements

Sheet resistance measurements were made using the Van der Pauw 4 point probe method on square substrates,[133] using a Keithly 2400 source meter and a custom substrate holder. Silver conductive paint was used on the four corners of the films to ensure a reliable contact with the substrate holder measurement pins. To minimise error in the measurement the probe contacts with the metal film were made as small as possible (Figure 2.4).[134] To ensure that the change in sheet resistance did not result from changes in the quality of the contacts, silver painted contacts were replaced with Al mechanical contacts and the same results were obtained. A potential of 5 mV was applied and the current was recorded. Two readings were taken 90° apart and averaged. For long term measurements a Labview program was written to record the current at regular time intervals for any number of measurements.

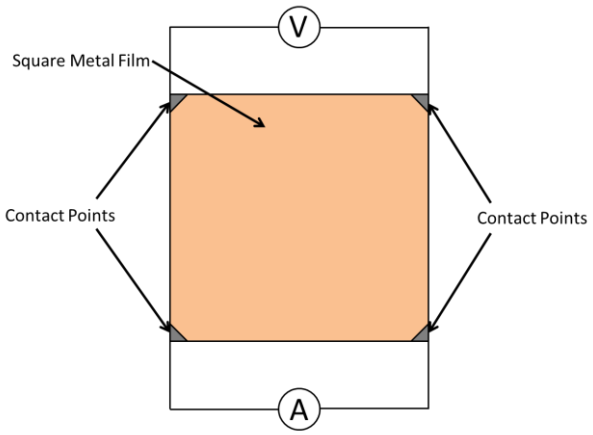

Figure 2.4: Experimental setup for sheet resistance measurements using the Van der Pauw method. A potential is applied between the two top contacts, with the current recorded between the bottom two contacts.

$$R_{SH} = \frac{\pi R}{\ln(2)} = \frac{\pi V}{I \ln(2)} \qquad \textbf{Equation 2.1}$$

Equation 2.1 is used to calculate the sheet resistance of the samples, where V is the applied voltage, I is the recorded current, R is the resistance in Ω and R_{SH} is the sheet resistance in Ω sq^{-1}.[133]

2.3.2 Optical Measurements

The transparency of the window electrode in an OPV is of prime importance, as it determines the amount of light incident on the photoactive layer, and is therefore a key determinant of PV device *PCE*.

Far-field transparency spectra were recorded using a Perkin Elmer Lambda 25 UV/Vis Spectrometer. Spectra were recorded at 1 nm wavelength intervals from 300-1000 nm unless otherwise stated. The spectra were recorded with the incident beam entering from the back of the device (i.e. through the glass) as would be the case in a functioning OPV. A clean glass slide was used as the reference for films deposited on

glass and a PET slide for films deposited on PET, unless otherwise stated. This reference ensures that reflection from the front face is subtracted. This is appropriate as reflections from the front face in a commercial PV module are greatly reduced using anti-reflective coatings.[135]

Transparency spectra of semi-transparent OPV devices were recorded using an external quantum efficiency (EQE) spectrometer which was built in house (Section 2.5.2) due to the small active area of these devices (~1 cm^2).

Dark field microscopy is used to capture an image of the scattered light from a sample. In this work, a bespoke experiment was designed to record spectra of the scattered light using an Ocean Optics USB2000+ spectrometer and a Zeiss Imager M1m optical microscope.

2.3.3 Kelvin Probe Technique

The Kelvin probe allows contactless measurement of changes in surface potential or work function when calibrated to a reference material of known work function. The reference used in this work was freshly cleaved highly orientated pyrolytic graphite (HOPG) which has a work function of 4.475 ± 0.005 eV.[136] This technique works by measuring the contact potential difference between a Au probe and the sample that forms when they are electrically connected. The Au probe is brought to within ~1 mm of the sample and oscillated with an amplitude 0.1-0.5 mm. This oscillation changes the capacitance of the system inducing an oscillating current in the wire connecting the probe to the substrate. A voltage is then applied until this oscillating current is nulled. This nulling voltage is equal in magnitude and opposite in polarity to the contact potential difference. This technique is sensitive to changes in surface potential of ± 3 meV, and is housed in a Faraday cage to screen against stray capacitance. The sample must be grounded, and this is achieved via a

copper pin and by bolting the movable sample holder to the base of the Faraday cage, as illustrated in Figure 2.5.

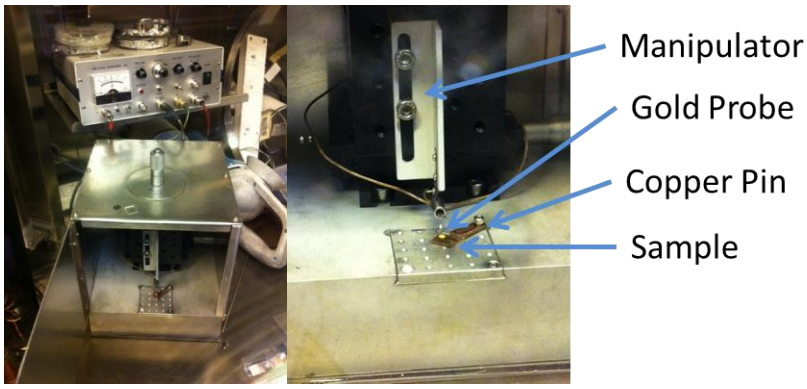

Figure 2.5: The Kelvin probe control box, Faraday cage, micrometers and probe (left) and a close up of the probe and sample (right).

The work function of a material is the energy required to remove an electron from the Fermi level to a place immediately outside the surface where it is at rest (i.e. the vacuum level at the surface). The work function (Φ) of a material is therefore a function of a materials chemical potential (μ) and the surface potential (χ). The surface potential component results from the dipole at the surface formed by spilling of the electron cloud into the vacuum. For this reason different crystal faces of the same materials can have different work functions, and the work function is very sensitive to surface contaminants (Figure 2.6).[20]

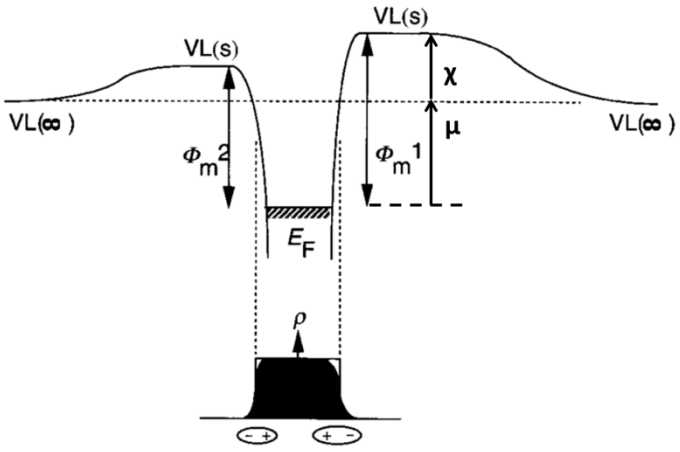

Figure 2.6: The potential surface for an electron being removed from a metal.[20]

Kelvin Probe work function measurements were made using a Besocke Delta Phi GmbH control unit and a 2.5 mm diameter Au probe (Figure 2.5) in a nitrogen filled glovebox, allowing measurements to be made with no exposure to the atmosphere. The work function of freshly cleaved HOPG was recorded and used as a calibration.

2.3.4 Atomic Force Microscopy

Atomic force microscopy (AFM) is a type of scanning probe microscopy with a spatial resolution orders of magnitude higher than optical microscopy which was invented in 1986.[137] The two main modes of AFM operation for measuring topography are contact mode and tapping mode. Both involve a cantilever with a very small tip being rastered across the surface of interest which causes a force on the cantilever, according to Hooke's law.[138] In contact mode, the tip height is varied to maintain a constant force between the cantilever and substrate. In tapping mode, the cantilever is oscillated at near its resonant frequency over the surface. Forces between the surface and the tip alter the oscillation amplitude, and the height is then adjusted to maintain constant oscillation damping. The

tip position is measured by shining a laser on the cantilever and recording the change in reflected laser spot position using a photodiode array (Figure 2.7).

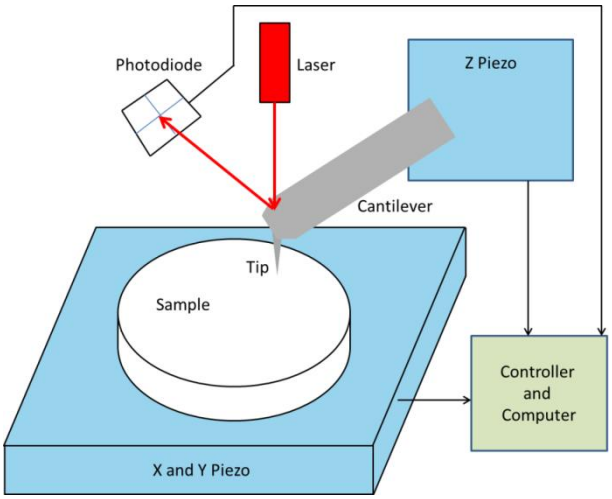

Figure 2.7: Schematic of the laser, photodiode array, sample, peizos, cantilever, computer and controller used in the AFM.

AFM was performed in air using an Asylum Research MFP-3D in tapping mode (Figure 2.8). The tips used were AC240TS-R3 (Asylum Research). The lateral resolution of the AFM is limited by the tip's radius of curvature, which are of the order of 9 ± 2 nm, thus limiting the size of features on the surface that can be measured to near this value. The vertical resolution of AFM is usually <1 nm. A root-mean-squared (RMS) roughness value can be calculated for each image, showing the mean deviation from the middle of the film in either direction. Unless otherwise stated, all surface roughness refers to this RMS roughness. An example AFM scan is shown in Figure 2.9.

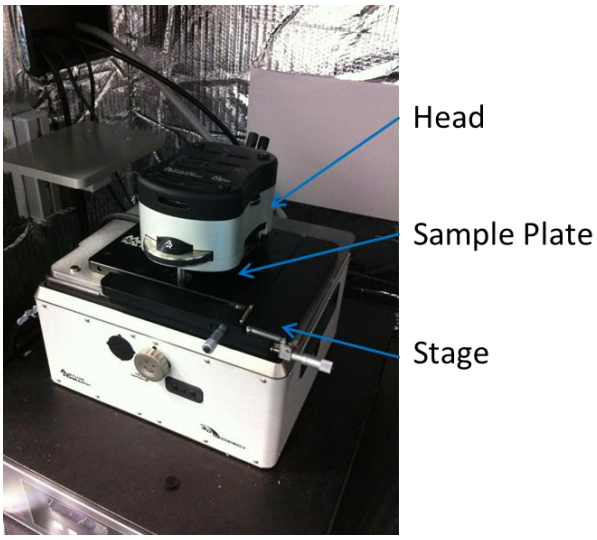

Figure 2.8: The Asylum MFP-3D used in this work.

2.3.5. Scanning Electron Microscopy

Scanning electron microscopy (SEM) is a type of electron microscopy that uses a focused electron beam to produce images, enabling higher resolution than is possible with optical microscopy. The actual resolution is a function of the wavelength of incident electrons which is determined by the acceleration voltage. The smallest feature size that can be imaged using a SEM is typically a few nms across.

In a scanning electron microscope, electrons are emitted from an electron gun (usually a tungsten filament) and focused using electromagnetic lenses to a spot size in the nm range. This electron beam is then rastered over the sample surface using electromagnetic lenses. The detector measures the secondary electrons emitted from the sample, and this is transformed into the brightness of a spot on an image. The samples must be conductive for SEM to prevent sample charging.

SEM measurements were carried out using a ZEISS Supra SP55. The accelerating voltage was typically 5 kV. An example SEM image and an AFM scan are shown in Figure 2.9.

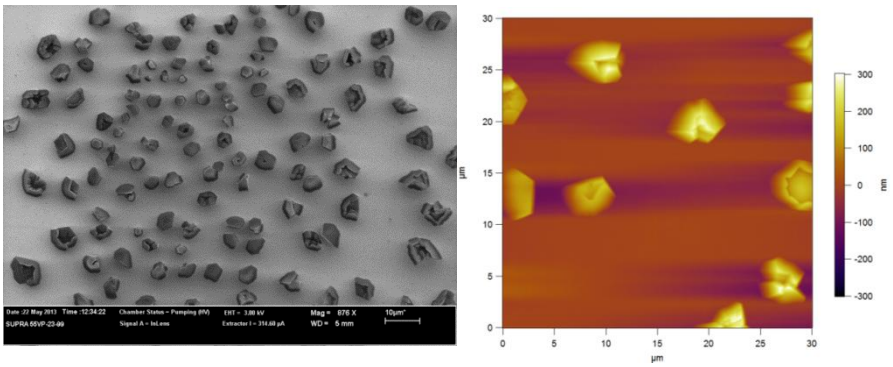

Figure 2.9: An SEM image of a Cu film with large structures (left) and an AFM scan of these structures (right).

Figure 2.9 shows that the lateral dimensions of structures can be visualised very well using an SEM. SEM does not however provide information about how high these structures are. For this reason, SEM and AFM are highly complementary surface imaging techniques. Image artefacts are possible with both AFM and SEM, and can be observed in the left image as shadowing around the structures, and on the right scan as the dark horizontal areas in line with the structures. In the AFM scan, these dark streaks are not real depressions in the film, but merely where the feedback loop of the tip was too slow to record the sharp decrease in height.

2.3.6. Ellipsometry Measurements

Ellipsometry is an optical technique used for investigating thin solid films. It measures the change in polarisation of plane polarised light that is reflected by the top and bottom

faces of a film, and the data is then modelled to yield the parameters of interest. It can be used to calculate the thickness of a film, or the refractive index and extinction coefficient as a function of wavelength.[106] This technique has the advantage of being non-destructive.

Ellipsometry was carried out using a Nanofilm EP3-SE spectroscopic Ellipsometer. Data was collected at 46 wavelengths, between 365 and 1000 nm. Refractive index and extinction coefficient were modelled using the manufacturer's EP4 software at fixed film thicknesses. The modelling software used assumes the layers are discrete and homogenous.

2.3.7. Static-Secondary Ion Mass Spectrometry:

Static-secondary ion mass spectrometry (s-SIMS) is a method of mass spectrometry which operates by bombarding the sample surface with a beam of molecular or atomic ions. The secondary ejected ions are then captured using a time-of-flight tube, or other mass analyser. This technique is extremely surface sensitive, with possible detection levels in the parts per billion range. It is therefore very useful for probing ultra-thin coatings such as SAMs. Samples must be vacuum compatible, and can be conducting or insulating. In this work, s-SIMS was performed using a KORE Surface Seer instrument using a Cs^+ primary ion source and a mass accuracy of ±10 milli amu.

2.3.8 X-ray Photoelectron Spectroscopy

X-ray photoelectron spectroscopy (XPS) is a surface sensitive spectroscopic technique used to determine the elemental composition and bonding environments of the top 5-10 nm of a material, with the exact depth dependent on the inelastic mean free path of an electron in the material and the take-off angle used, as described by the Beer-Lambert law. During XPS an X-ray beam is incident on a sample under ultra-high vacuum and via

the photoelectric effect, electrons are ejected from atoms in the target sample. The number and kinetic energy of ejected core photoelectrons is then measured. Since energy levels in atoms and molecules are quantised, each element has a characteristics set of electron binding energies. The binding energy of core level electrons is typically perturbed by the chemical bonding environment the element is in by up to 10 eV. This is due to the fact that the binding energy of the core electrons is a function of how much charge screening they experience as they leave the atom, which in turn depends on the arrangement of valence electrons. So a Cu atom that is not oxidised will have a lower core electron binding energy than that of oxidised Cu because bonding to oxygen in CuO or Cu_2O withdraws valence electrons from the Cu atom, reducing the screening of the attractive interaction between the nucleus and the recorded ejected electrons. These shifts in the binding energy of core electrons due to perturbation of the valence band structure are called *chemical shifts*.

An XPS spectrum shows the binding energy of electrons on the *x*-axis, and the number of electrons (the intensity, or counts) on the *y*-axis. A survey scan across a wide range of energies is carried out, and then areas of interest are scanned for longer periods and at higher resolution to improve the signal to noise ratio. An example of a high resolution scan is shown in Figure 2.10.

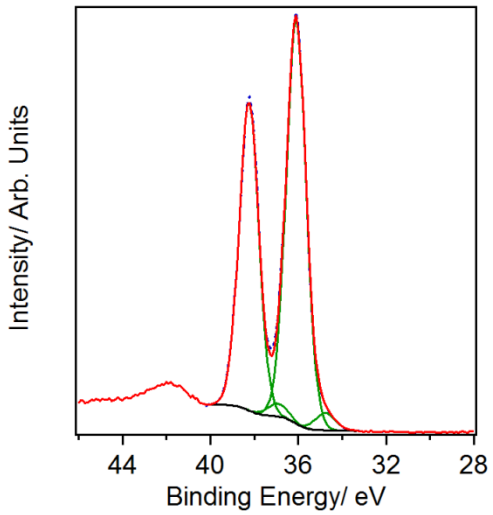

Figure 2.10: A typical high resolution XPS spectrum showing the W4*f* region for a WO_{3-x} film. Raw data, fitted peaks, total fit and background are coloured red, green, dotted blue and black respectively.

XPS measurements were carried out in a UHV system with a base pressure of 2 × 10^{-11} mbar. The sample was excited with X-rays from a mono-chromated Al K_α source ($h\nu$ = 1486.6 eV), with the photoelectrons being detected at a 90° take-off angle using an Omicron Sphera electron analyser. XPS measurements were made with assistance from Dr. Marc Walker (University of Warwick). The survey scan was carried out with binding energies from 1400 eV to -3 eV at a resolution of ~1.50 eV. Following this, core level spectra were collected at a resolution of 0.47 eV. Subsequent data acquisition, processing and fitting was carried out using Casa XPS software, with graph plotting and presentation carried out using Igor Pro 6. When peak fitting, a Shirley background was subtracted from the raw data and the peaks fitted using a non-linear least square routine with a mix of Gaussian and Lorentzian shape peaks.

2.3.9 Ultra-violet Photoelectron Spectroscopy

Ultra-Violet Photoelectron Spectroscopy (UPS) is a technique similar to XPS, in which monochromatic ultraviolet light (e.g. He I emission at an energy of 21.22 eV) is incident on the sample, and the kinetic energy of the ejected electrons is recorded. UPS is a very surface sensitive technique with photoelectrons emanating from only the top 1-2 nm of a sample, as the escape depth of the photoelectrons is small due to their low kinetic energy. The energy of UV photons is much lower than X-rays and UPS therefore probes the valence band electrons and is used to measure the energy of the Fermi level and valence band edge with respect to the vacuum level. UPS is a complimentary technique to the Kelvin Probe.[113] The Kelvin probe technique measures the work function to within an error of ±5 meV and measures the average work function under the probe. UPS measures the work function with a margin of error of ±100 meV and measures the lowest work function value. These differences mean that the measurement technique must be considered when discussing work function values measured using different techniques. A typical UPS spectrum is shown in Figure 2.11.

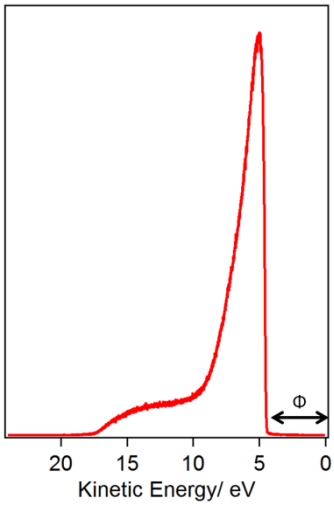

Figure 2.11: A typical UPS spectrum of a Au 8 nm | WO_{3-x} 20 nm film. Φ denotes the work function.

UPS spectra were recorded with assistance from Dr .Marc Walker (University of Warwick). UV photons with energy 21.22 eV from a He I plasma source in the same system as the XPS measurements were carried out. A bias of 10.0 V was applied. The scans were recorded at an emission angle of 0° with a binding energy range of 10 eV to 34 eV. After data acquisition, processing and fitting was carried out using Casa XPS software, with graph plotting and presentation carried out using Igor Pro 6.

2.4 Device Fabrication

2.4.1 Organic Semiconductor and Metal Oxide Deposition

All device fabrication and testing were carried out in a nitrogen filled glovebox (MBraun MB 20G LMF, Figure 2.12) unless otherwise stated. Evaporation of metals, metal oxides and small organic molecules was carried out using a CreaPhys Organic molecular evaporator housed in an MBraun eVap bell-jar. The thickness of materials deposited was measured using a quartz-crystal microbalance (QCM) mounted adjacent to the substrate. This QCM was calibrated regularly by evaporating a thick (~100 nm) film of each material onto a glass substrate, scoring the film using a needle and imaging the scored region using an AFM to determine the true thickness. During evaporation the samples were rotated to minimise shadowing effects and increase uniformity across different substrates.

Figure 2.12: The MBraun MB 20G LMF Glovebox (left) with solar simulator (far left) and the CreaPhys Organic molecular evaporator (right) used.

Table 2.1 lists the deposition parameters for the materials thermally evaporated in this work.

Material	Temperature/ °C or SP*	Rate/ Å s^{-1}	Usual Thickness/ nm	Supplier and Purity
Cu	SP 14	1	8	Kurt J. Lesker 99.99%
Al	SP 12	1	0.8 - 100	Kurt J. Lesker 99.99%
Au	SP 17	1	8	Kurt J. Lesker 99.99%
Ag	SP 11	1	12	Alfa Aesar 99.999%
WO_{3-x}	SP 19	0.1 - 0.3	20	Sigma Aldrich 99.995%
MoO_3	SP 9	0.2 - 0.3	5	Sigma Aldrich 99.99%

ClAlPc	310- 340 °C	1	20	Sigma Aldrich
C_{60}	550 °C	0.1-0.3	32.5 or 40	Nano c
BCP	140 °C	0.5	8	Alfa Aesar
Pentacene	165-190 °C	0.7 - 1.0	45	H.W.Sands Corp.

Table 2.1: Deposition parameters for metals, metal oxides and organics. * SP is an arbitrary unit proportional to the amount of current flowing through a tungsten boat. The actual temperature will depend on a number of factors, such as evaporation boat geometry. All organic materials were purified in house via train sublimation.

The average distance from source to sample is 30 cm. The working pressure of the system was 1×10^{-5} mbar for metals and metal oxides, and 6×10^{-6} mbar for organics. The organic semiconductors and metal oxides were evaporated from boron nitride crucibles. The metals were evaporated from tungsten boats. All evaporation materials were purchased from commercial sources at high purity and were used as received.

WO_3 has a melting point of 1473 °C at atmospheric pressure[112] and was therefore experimentally taxing to evaporate with the system working near or at its maximum operating temperature. This meant that for WO_{3-x} the base pressure was not always 1×10^{-5} mbar and could rise as high as 8×10^{-5} mbar.

When evaporating top Al electrodes the rate was kept below 2 Å s^{-1} for the first 20 nm. This ensured that the organic semiconductors were not damaged by high energy Al atoms reaching the organic semiconductors and forming defect states where charge recombination can take place.

All materials were either purchased at purity sufficient for OPVs, or purified using train sublimation.

2.4.2 Device Shadow Masks and Device Layout

When fabricating OPV devices, different shadow masks (Figure 2.13) were used to define the electrode areas, ensuring the device top and bottom electrodes do not make contact and short circuit the device, and to produce multiple pixels on each slide. These masks were fabricated by an external supplier and are bespoke.

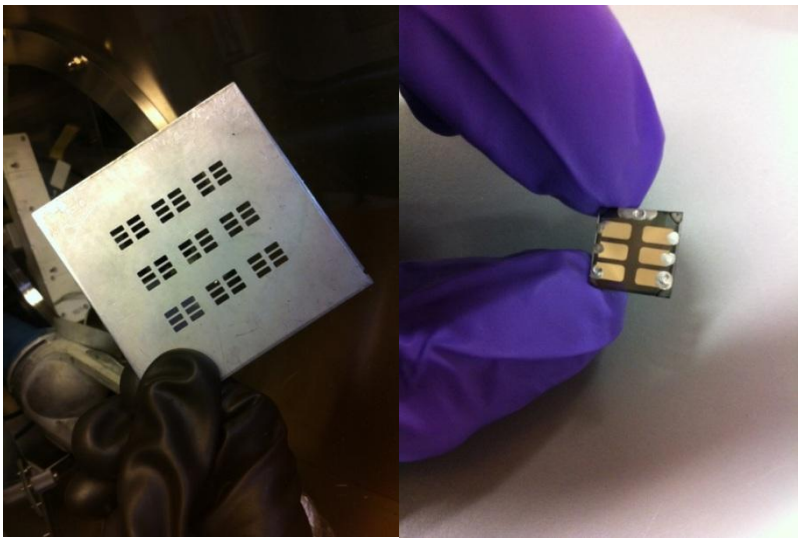

Figure 2.13: An example of the type of shadow mask used in this work to create the top electrodes of devices, and 6 pixels per substrate (left) and example OPV device (right).

The evaporation and mask systems used allowed the fabrication of a maximum of 9 (13×13 mm) substrates at once, each with a maximum of 6 pixels with an active area of 0.06 cm^2. Alternatively, 9 substrates with 3 pixels per substrate and an active area of 0.16 cm^2 per pixel could be fabricated. Active area variations from pixel-to-pixel were higher for the 0.06 cm^2 devices than for the 0.16 cm^2 devices. Thus, in Chapter 5 when

analysing data to judge improvements in photocurrent, 0.16 cm^2 devices were fabricated. This lowered the standard deviation of the J_{sc} and *PCE* significantly.

2.4.3. Spin Coating and Device Annealing

Spin coating is used in a laboratory environment to form thin films of solution processed materials with thicknesses of ≥ 5 nm and a thickness variation of ± 10 % across the film. The substrate is held in place at the centre of a disc using a vacuum chuck and the plate is spun at a specific rate for a specified time. The final film thickness depends on the viscosity of the solution, the spin speed, the spin time and the solvent volatility. Higher spin speeds yield thinner films. The concentration of material used and how the solution wets the substrate also affect the film thickness and morphology.

Spin coating was carried out using a SUSS MicroTec Delta 6RC spin coater in a nitrogen atmosphere (Figure 2.14). Polymeric donor materials and fullerene based acceptor materials were spin cast from mixed solutions to form BHJ layers, the morphology and thickness of which could be controlled by spin speed and post-deposition annealing.

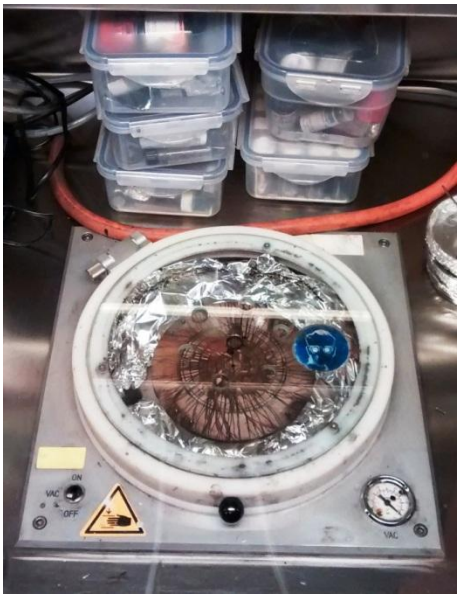

Figure 2.14: The SUSS MicroTec Delta 6RC spin coater used in this work.

In this work all polymer layers (PTB7 and PCDTBT), fullerene derivatives (PCBM and $PC_{70}BM$), and some metal oxide precursors were deposited by spin coating. Annealing of devices was carried out in the glovebox using a hotplate with a copper plate and a thermocouple fitted for accurate temperature measurement and to ensure uniformity of heating.

PTB7/$PC_{70}BM$ films were spin cast from a solution of 97:3 dichlorobenzene:diiodoctane at a concentration of 10 mg/ mL and 15 mg/ mL of PTB7 and $PC_{70}BM$ respectively. The addition of diiodooctane to the dichlorobenzene decreases the BHJ domain size and results in a higher *PCE*.[34] The solutions were stirred overnight at 50 °C. Spin coating was carried out at 1000 rpm for 60 seconds and then 6000 rpm for 4 seconds. The second higher spin speed was required to remove the excess material accumulated at the substrate corners. Solution filtration or film annealing were not needed.

PCDTBT/$PC_{70}BM$ films were spin cast from a solution of chloroform at a concentration of 4 mg/ mL and 12 mg/ mL of PCDTBT and $PC_{70}BM$ respectively. The solutions were stirred for 1 hour at 65 °C. Spin casting was then carried out at 6000 rpm for 60 seconds. The films were then annealed for 30 minutes at 80 °C under nitrogen.

Solution processed tungsten oxide films were prepared by spin coating tungsten isopropoxide in IPA at 1.5 mg/ mL. The solution was drop cast onto the substrates before spinning at 4000 rpm for 60 seconds. The substrates were then annealed at 150 °C for 10 minutes in the glovebox.

Solution processed titanium dioxide films were prepared by spin coating from a stock solution of titanium isopropoxide (0.1 ml) in 1-Butanol (0.5 ml). The solution was drop cast onto the substrates before spinning at 2000 rpm for 60 seconds. The substrates were then annealed at 450 °C for 30 minutes in the glovebox. This leads to a film thickness of approximately 20 nm. Decreasing the titanium isopropoxide stock solution concentration so that 0.1 ml of titanium isopropoxide is diluted with either 1 ml or 2 ml or 1-butanol leads to 10 and 5 nm films respectively.

2.5 Device Testing

2.5.1 Current Density- Voltage Testing

Current density/voltage (*JV*) testing was carried out using a Keithley 2400 source meter, and a custom Labview interface in the dark and under 1 sun simulated solar illumination using an ABET technologies Sun 2000 Solar Simulator (Figure 2.15). Given the active area of the device, the Labview interface calculates the J_{sc}, V_{oc}, *FF* and *PCE*. The intensity was set to 100 mW cm^{-2} over the AM1.5 solar spectrum. The light source was a Xenon short arc lamp with AM1.5 filters and was calibrated using a calibrated silicon diode (PV Measurements Inc.) with KG5 colour filter. This yields a short circuit current of 45 mA cm^{-2}. Devices were scanned from -1 to +1 V with 201 data intervals unless otherwise stated. The electrical leads connected to the multimeter were swapped for use in inverted devices, so that the characteristics are easily comparable.

Figure 2.15: The ABET technologies Sun 2000 Solar Simulator used.

OPV devices were tested in a nitrogen filled glovebox, allowing characterisation of OPV cells without encapsulation, and removing the need to consider degradation by water or oxygen. Prior to testing each electrode contact (usually six Al top electrode contacts and one ITO/Cu transparent electrode contact) had a spot of silver paint (RS components) applied to it to ensure good electrical contact with the device holder.

2.5.2 External Quantum Efficiency Measurements

External quantum efficiency (EQE) spectra, also known as incident-photon-to-converted-electron (IPCE) spectra, yield the spectral response of the device. When combined with absorption data, this technique gives insight into which material in the device is generating the photocurrent.

For an ideal cell the IPCE/EQE would be unity across all the wavelengths, showing that one electron in the external circuit is created for every photon incident upon the device. However, this is not possible as there is insufficient material thickness for full

light absorption of all wavelengths due to the exciton diffusion bottleneck, reflection from the glass face and exciton quenching near to the electrodes. Figure 2.16 shows an example EQE spectrum for an OPV device based on a PTB7/$PC_{70}BM$ active layer from which it is evident that the device is generating photo current from 350-750 nm with a peak EQE of ≈0.7 at 400 nm.

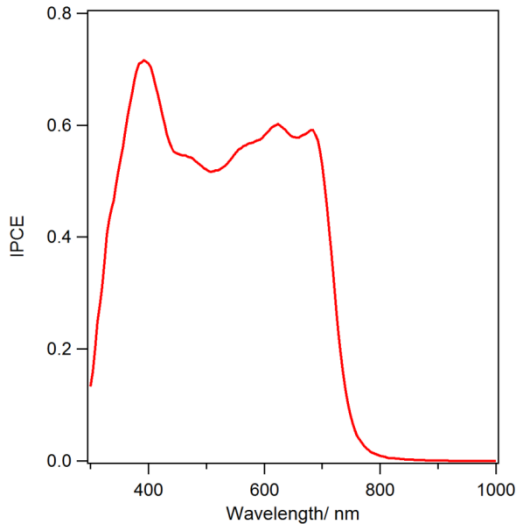

Figure 2.16: A typical EQE spectra of a PTB7/$PC_{70}BM$ OPV device.

EQE measurements were performed under nitrogen with a white light xenon arc lamp (Sciencetech SF150), monochromator (Photon Technology International), focussing and splitting lenses, current-voltage amplifier (Femto DHPCA-100), lock-in amplifier (Stanford Research SR830 DSP) and custom Labview interface. The incoming monochromatic light was chopped at 500 Hz to enable the lock in amplifier to remove any signal generated from background light. The monochromatic light intensity was calibrated against a Si photodiode (818UV, Newport) and the ratio of light hitting the reference and sample was recorded using two Si photodiodes (818UV, Newport) as a

function of wavelength and taken into consideration. This last step is necessary as the splitting lenses do not split the light equally at every wavelength.

2.5.3 Data Analysis

To ensure the statistical significance of any change in device performance parameters (e.g. J_{sc}, V_{oc}, *FF*, *PCE*),[139] at least 18 pixels of each structure were fabricated and the standard deviation is given for each parameter. All data was analysed using Microsoft Excel and plotted using Igor pro 6.

2.5.4 Optical Simulations

Optical simulations for transparency and electric field intensity were carried out using The Essential Macleod Software from Thin Film Center Inc. Refractive index and extinction coefficient data as a function of wavelength were entered into the software for each material. This data was obtained from the literature and from spectroscopic ellipsometry measurements (Section 2.3.6).

Electric field intensity simulations were performed using The Essential Macleod Software from the Thin Film Center Inc. This software assumes smooth interfaces and homogenous media. This technique allows microcavity effects to be visualised, and design of device architectures to ensure that the electrical field strength is maximised in the active layer of the device, producing the maximum photocurrent.

2.5.5 Degradation Measurements

In addition to degradation measurements performed using the solar simulator described in Section 2.5.1, longer term stability test were performed on a rig built in house (Figure 2.17).

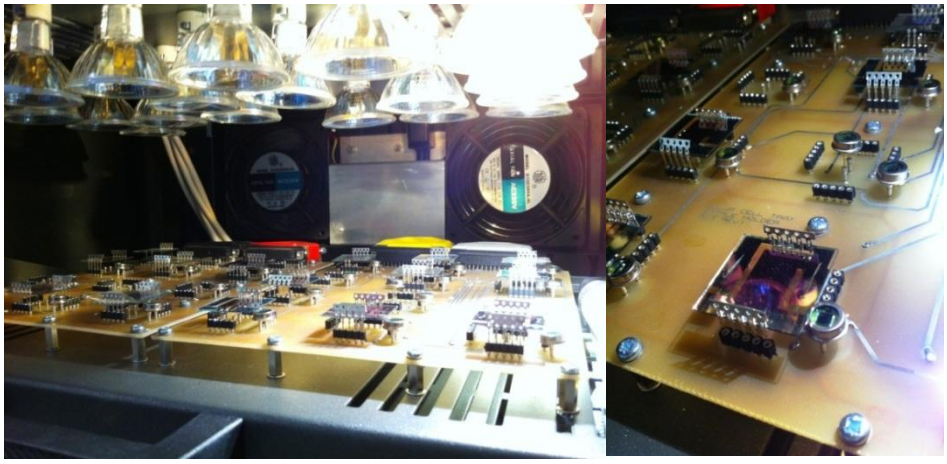

Figure 2.17: The long term illumination rig used for *JV* testing.

Connections to the circuit board below are made with the metal legs shown on the right of Figure 2.17. A Keithley source meter and custom Labview program were then used to run *JV* scans of the cells as described in Section 2.5.1. When not being *JV* tested these cells were all held at their maximum power point via connection to a resistor typically between 150-300 Ω. The cells in this rig were illuminated with commercially available halogen spotlight bulbs which are only a very approximate match to the AM1.5 spectrum. The intensity was measured using a photodiode for each cell and was always 100 ± 8 mW cm^{-2}.

Chapter 3 – Ultra-thin Cu/Al Electrodes

The majority of the work presented in this chapter has been published in the following paper:

"*An Indium-Free Low Work Function Window Electrode for Organic Photovoltaics Which Improves with In-Situ Oxidation*" O.S. Hutter, H.M. Stec, R.A. Hatton, *Adv. Mater*. **2013**, *25*, 284.

3.1 Abstract

This chapter describes an exceptionally robust Cu electrode passivated with an ultra-thin Al layer which simultaneously functions as the low work function electron-extracting electrode, a sink for oxygen and water molecules in the photoactive layer, and a low cost window electrode in inverted BHJ OPVs.

3.2 Background

Organic semiconductors offer the prospect of truly low cost PVs with a very short energy payback time.[17,19,140] As outlined in Chapter 1, this potential can only be realised if low cost alternatives to conducting oxides (e.g. ITO) are forthcoming as window electrodes[19,140,141] and economically viable transparent barrier materials and desiccants are developed that are capable of slowing the ingress of water and oxygen enough to realise useful device lifetimes.[26,49,142,143] There is growing evidence that even trace amounts of O_2 are problematic in OPVs,[144,145] even for relatively stable organic semiconductors such as PCDTBT.[55] Without advances in both of these areas the cost advantage associated with solution processing organic semiconductors will be off-set by the high cost of the window electrode and device encapsulation.[143]

Optically thin (<10 nm) metal films are emerging as a viable class of transparent electrode for OPVs, since both micro-cavity effects[82,146,147] and refractive index matching[146,148] can be used to mitigate against the reduced far-field transparency as compared to optimised conducting oxides.[149] Advantages of optically thin metal films include compatibility with flexible substrates,[150] low materials and processing cost (e.g. by decomposition of an organo-metal precursor deposited by slot-die coating,[17] or by thermal evaporation rather than sputtering, with no requirement for post-deposition annealing), ultra-low roughness[129,151] and chemical uniformity.[90,129,152] Proven low cost manufacturing infra-structure is available for vacuum deposition of metal films over large areas in the form of roll-to-roll vacuum evaporation systems currently used in the packaging industry.[18,153] Owing to its high electrical conductivity,[154] resistance to electro-migration[155] and relatively low cost,[93] Cu is widely used in the microelectronics industry and is receiving growing attention as an electrode material for OPV. Indeed, Cu offers comparable conductivity to Ag, is 1000 times more abundant than In and is 100 times less expensive.[93,84]

Due to its relatively high work function of 4.5-4.6 eV,[156] Cu is most suitable as the hole-extracting electrode in OPVs.[150,154] However, unlike Au or Pt, its work function is not high enough to render it resistant to oxidation under ambient conditions. Exposure to air at room temperature results in the formation of an insulating Cu_2O/CuO layer at the surface of bulk Cu, the thickness of which is not self-limiting.[158] In the context of optically thin films this gradual conversion of Cu to copper oxide results in a large increase in sheet resistance with increasing oxidation time, which renders it unusable in OPV devices. For Cu films to be a viable alternative to ITO glass, they must therefore be passivated from oxidation. In the small number of literature reports that relate to the use

of Cu electrodes in OPVs they are exclusively used as the hole-extracting electrode and are invariably capped with a high work function oxide layer to optimise the interfacial energetics.[150,157,159]

The performance of OPVs is critically dependent on the sheet resistance of the electrodes,[160,161] which for the transparent electrode cannot exceed 15-20 Ω sq^{-1},[46] and should preferably be <10 Ω sq^{-1}.[90] Increases in sheet resistance adversely impact the efficiency of current extraction to the external circuit due to the voltage drop in the plane of the electrode. Additionally once the surface oxide layer exceeds a thickness of ~1 nm it is no longer transparent to the transport of electrons across the interface between the metallic Cu and the organic semiconductor and so the efficiency of current extraction is eroded exponentially with increasing oxide thickness.[162] A further complication that arises when the surface of a Cu electrode oxidises *in-situ* in an OPV device is the 42% increase in volume occupied by the oxide as compared to the metal[163] which increases the likelihood of delamination.[50] Cu electrodes therefore suffer from similar drawbacks to the low work function metals used for electron extraction in OPVs such as Al and Ca, the oxidation of which is known to be a major mode of device degradation.[164-166] To date two different approaches have been employed to mitigate against this problem: (i) The development of air stable electron-extracting layers incorporated at the electrode/organic semiconductor interface, most notably TiO_x,[83] ZnO,[167] and Al:ZnO.[38]; (ii) The use of increasingly sophisticated barrier/encapsulation layers to slow the inevitable ingress of oxygen and water from the atmosphere into the photoactive layer.[143,168]

There are few reports of materials that actively scavenge O_2 and H_2O in an organic electronic device, including TiO_x deposited from a sol-gel,[169,170] and a 5-10 nm CrO_x interfacial layer deposited under low vacuum.[171] In these cases the oxygen/water

scavenging capacity and electron transport properties both originate principally from oxygen array vacancies and so oxygen scavenging is at the expense of electron conductivity.

Al_2O_3 films of >100 nm are known to be an effective encapsulant for organic electronics, particularly when deposited by atomic layer deposition.[172,173] Gan *et al*. have also reported that ultra-thin (0.3 nm and 1 nm) Al_2O_3 layers are effective at retarding the oxidation of Cu films heated in air for 30 seconds.[174] Pérez Lopéz *et al.* have shown that 1.4 nm Al films can retard the diffusion of Cu into the high work function oxide MoO_3 when the metal is deposited onto the oxide.[159]

In this chapter passivation of ultra-thin Cu films from ambient oxidation is described using an ultra-thin Al layer. This Cu | Al film supported on glass modified with a mixed molecular adhesive layer is shown to be a low cost window electrode for OPVs which simultaneously removes the requirement for conducting oxide and conventional low work function electrodes and functions as a sink for oxygen/water in the heart of the device. It is shown that the functionality of this electrode actually improves upon oxidation *in-situ* as demonstrated in BHJ organic photovoltaics and so this composite electrode also serves as a built in desiccant for oxygen.

3.3 Experimental

Preparation of ultra-thin Cu | Al films on glass: When preparing Cu films with the APTMS/MPTMS mixed adhesive layer, it is important for the APTMS not to be used from the fridge, as this results in Cu films with a higher sheet resistance.

OPV fabrication and testing: PCDTBT and $PC_{70}BM$ (Ossila Ltd) were deposited as described in Chapter 2, and allowed to dry at room temperature under nitrogen for 10 min

before annealing at 80 °C for 30 min. MoO_3 was evaporated at 0.1 nm s^{-1}, Al was deposited at 0.5-3 nm s^{-1} through a shadow mask.

Optical transparency measurement: For far-field transparency measurements the reference material was a plain glass slide. The incident beam passed through the glass first of all, as is the case in an OPV device.

Oxidation: Oxidation of all films was carried out in laboratory air, with the exception of electrodes that were incorporated into OPVs and OPV devices, which were oxidised in 1 bar of dry air (<0.015 vol% H_20) in the dark.

3.4 Results and Discussion

Ultra-thin Au films on glass using a mixed SAM as a molecular adhesive layer have been reported previously by Stec *et al.*[129] This protocol was used to fabricate ultra-thin Cu films on glass for the first time as part of this work. The high affinity of Cu for amine and thiol moieties ensures that this approach works well for the preparation of optically thin Cu films.[93,128] Indeed, the two SAMs (APTMS and MPTMS, Figure 2.3) used in this work have been used in isolation to bind Cu to glass and silicon.[175,176] Since the work presented in this chapter, the mixed monolayer protocol has been improved for the formation of Cu films to realise lower sheet resistance values. This was achieved by altering the temperature at which the APTMS is used. The sheet resistance of films fabricated using APTMS stored at 3-5 °C and room temperature were ~11 and 7 Ω sq^{-1} respectively. This is attributed to the primary amine on APTMS catalysing the coupling reaction between the methoxysilane groups and hydroxyl groups at the glass surface, the substrates increased reactivity immediately after UV/O_3 treatment, and the vapour pressure increase of the APTMS at elevated temperature.

The transparency spectrum of a Glass | SAM | Cu 8 nm film is shown in Figure 3.1, with the simulated transparency of the same film using Macleod software. The close agreement of the recorded and simulated spectra in Figure 3.1 illustrate that the fabricated Cu films are continuous and are slab-like. The far-field transparency of Cu | Al electrodes is also similar to Cu electrodes, consistent with the very low Al thickness and expectation that the surface oxide is a wide band gap material.[177,178] Upon oxidation in air for 24 hrs the transparency remains the identical within substrate to substrate variation, and the sheet resistance decreases from 10.8 to 9.9 Ω sq^{-1}, in keeping with the result shown in Figure 3.3.

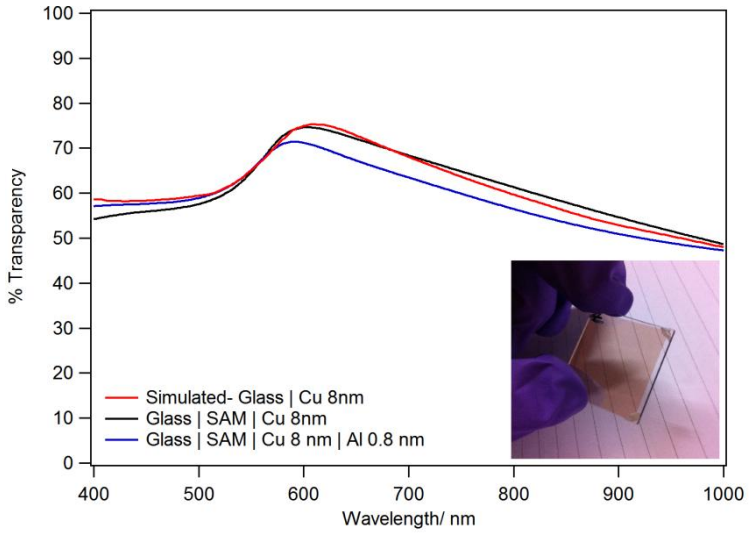

Figure 3.1: Far-field transparency of Glass | SAM | Cu 8 nm (black), Glass | SAM | Cu 8 nm | Al 0.8 nm (blue) and simulated Glass | Cu 8 nm (red) films. Inset: Optical image of a Cu | Al film.

Measurements of the morphology of these Cu 8 nm films performed using AFM (Figure 3.2) corroborate this conclusion, with a roughness comparable to the underlying glass substrate.

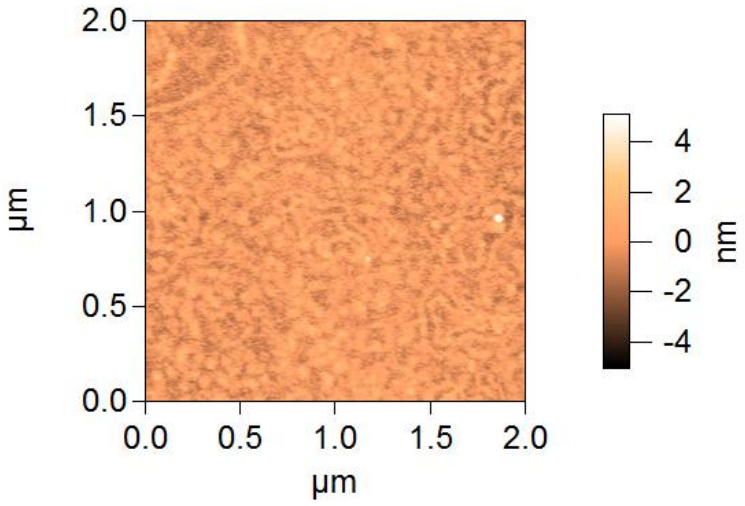

Figure 3.2: AFM scan of a Glass | SAM | Cu 8 nm film.

The AFM scan in Figure 3.2 has an roughness of 0.66 nm over 1 × 1 µm, which is comparable to the underlying glass substrate, confirming that the Cu film is continuous and slab-like. The swirl like features on the Cu surface are associated with the underlying glass substrate, showing Cu forms a conformal layer. The sheet resistance and work function of these glass | SAM | Cu 8nm films is 14 Ohms sq^{-1} and 4.57 ± 0.05 eV respectively. The sheet resistance is comparable to that of the Au ultra-thin films of similar thickness demonstrated by Stec. *et al.*[129] and the work function is consistent with that of Cu. Selecting the thickness of these films for application as the window electrode in OPV is a balance between decreasing sheet resistance and decreasing transparency upon increasing the film thickness. A film thicknesses of ~7 nm was decided to be the best balance of these two criteria. This was largely decided on the basis of sheet resistance, since much above 15 Ω sq^{-1} is known to result in an unacceptable reduction in *PCE*.

The fabricated ultra-thin Cu films have the disadvantage that they oxidise in air resulting in increased sheet resistance, as shown in Figure 3.3 (blue line). The resistivity of the 9 nm and 7 nm Cu films is 8.1×10^{-8} Ω m and 9.8×10^{-8} Ω m respectively. These

values are a factor of ~4.7 and ~5.7 times larger than bulk Cu (1.7×10^{-8} Ω m)[179] respectively. Since these film thicknesses are ~4.4 times and ~5.7 times smaller than the mean free path of an electron in bulk Cu,[180] this scaling of resistivity with thickness shows that scattering at the top and bottom surfaces of the Cu film may be the primary determinant of film resistivity when the film thickness is so low and is further evidence that the films are slab like.[147]

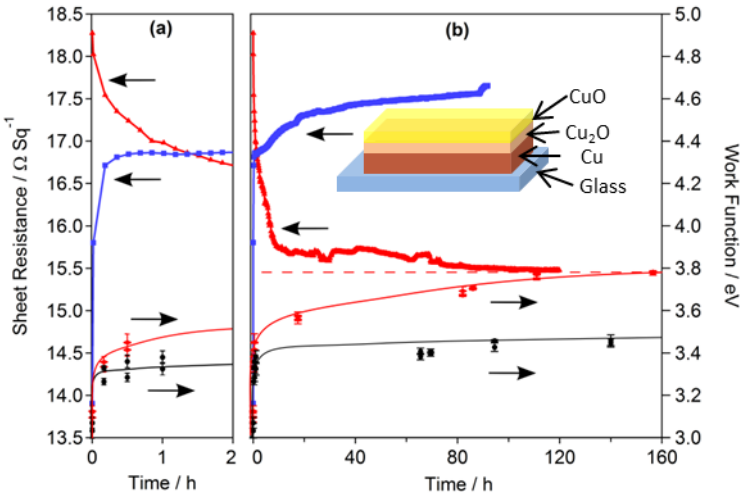

Figure 3.3: Sheet resistance and work function as a function of time exposed to air. Part (a) is an enlarged version of the region between 0 and 2 hours in Part (b).: (Upper, solid blue line) sheet resistance of Cu 7 nm film; (upper, solid red line) sheet resistance of Cu 7 nm | Al 0.8 nm film. The fluctuations in the sheet resistance are due to fluctuations in ambient temperature.; (lower red data points and red line to guide the eye) work function of Cu 7 nm | Al 0.8 nm; (lower, black data points and line to guide the eye) work function of Al 34 nm film. The first measurements (Time =0) were made in a N_2 atmosphere immediately after metal deposition. Inset: Schematic of a Cu film after oxidation.

The sheet resistance of 7 nm Cu film is ~14 Ω sq^{-1}. However, Figure 3.3 shows that upon exposure to air sheet resistance increases rapidly within the first hour followed by a gradual continuous increase. By capping the Cu electrode with a 0.8 nm Al overlayer this increase in sheet resistance is prevented. Thinner Al overlayers were not sufficient to prevent oxidation upon exposure to air. Other methods of surface passivation were also attempted, including the use of an ultra-thin Mg passivation layer[181] but did not passivate the Cu film. Notably, the Cu 7 nm | Al 0.8 nm films have a 4.5 Ω sq^{-1} higher starting resistance than Cu only, which is attributed to Al diffusion into the underlying Cu film particularly between grain boundaries, since Al doped Cu is known to have a higher resistivity than pure Cu even at very low Al concentrations.[182] However, the sheet resistance of the binary Cu 7 nm | Al 0.8 nm film *decreases* by ~15% (3 Ω sq^{-1}) upon oxidation in air. This increase in conductivity is attributed to migration of Al atoms dissolved in the Cu film to the film surface where they are oxidised. Since the sheet resistance of the oxidised Cu 7 nm | Al 0.8 nm film converges to a value 1.5 Ω sq^{-1} above that of unoxidised Cu films, either some Al remains dissolved in the bulk of the Cu film or the thickness of Cu film is reduced due to some Cu being bound up in the surface oxide layer. It is known that Al dissolved in Cu can diffuse at temperatures as low as 100 °C.[182,183] However, the melting point of Cu and Al are 1083 and 660 °C,[184] so it is quite unexpected that diffusion should occur so rapidly at room temperature. This effect is attributed to the suppression of the Cu melting point due to the low film thickness, since 10 nm Cu films have been observed to melt below 400 °C,[185] which in turn suppresses the temperature at which Al atoms can diffuse. Upon deposition of this ultra-thin Al layer, the surface roughness of the electrode remains very low at ~0.6 nm (Figure 3.4).

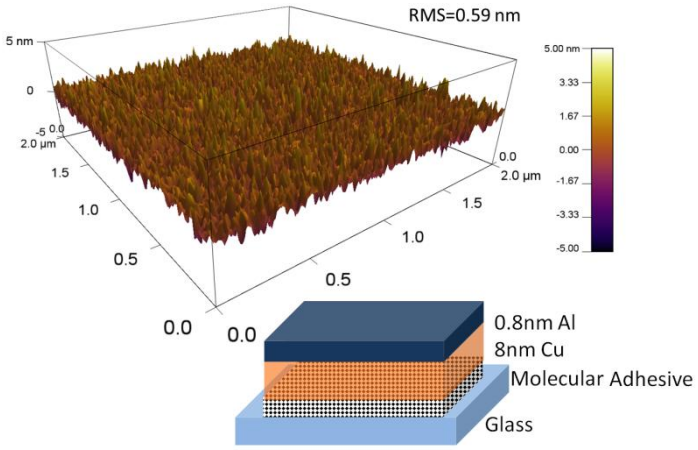

Figure 3.4: 3-D AFM scan of surface morphology of a Cu 8 nm | Al 0.8 nm film (top) and a schematic diagram of the electrode structure (bottom). The film shown has a root-mean-squared roughness of ~0.6 nm.

In principle the effectiveness of such a thin Al overlayer in protecting the underlying Cu towards oxidation cannot be rationalised in terms of the formation of an 0.8 nm Al_2O_3 capping layer since the thickness of the self-limiting oxide on Al is known to be greater than 2 nm.[186-187] It is the formation of this thick oxide layer at the Al/organic semiconductor interface that is the reason for the increase in series resistance in OPVs.[166,188] The surface sensitive technique of static secondary ion mass spectrometry reveals that for a Cu | Al 0.8 nm film the upper most surface includes copper oxide in addition to aluminium and aluminium oxide as shown in Figure 3.5. This sample was in air for 3 minutes prior to data acquisition.

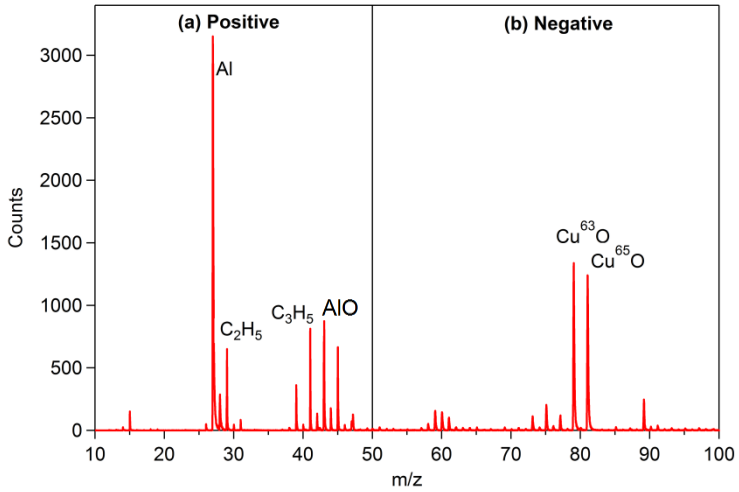

Figure 3.5: Static secondary ion mass spectrometry (s-SIMS) spectra of an ultra-thin Cu film with a 0.8 nm Al overlayer: **(a)** positive ion spectrum.; **(b)** negative ion spectrum.

Even if the Al layer thickness is increased by more than a factor of five to 4.2 nm copper oxide is still present at the surface (Figure 3.6) consistent with the formation of a dense ultra-thin $Al_xCu_yO_z$ surface layer. Various Al oxide fragments are also present in the s-SIMS showing oxidation of the Al e.g. *m/z* values of 59 and 77 for AlO_2 and AlO_3H_2 respectively in the negative spectrum in addition to the peak at *m/z* 43 in the positive spectrum.[189]

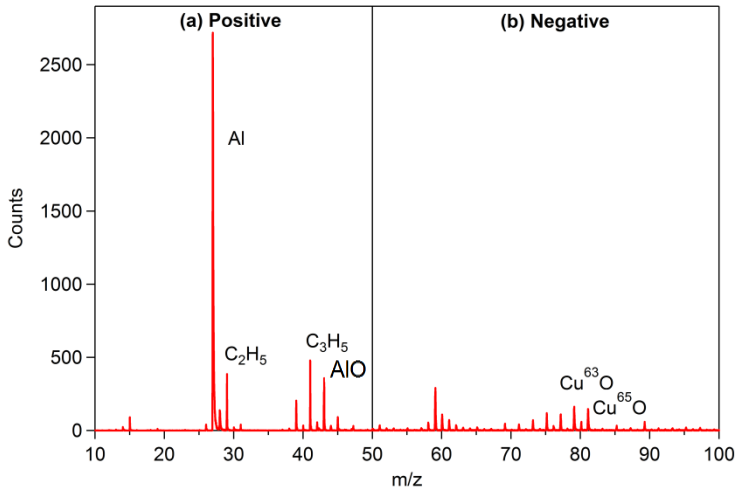

Figure 3.6: s-SIMS spectrum of an ultra-thin Cu film with a 4.2 nm Al overlayer: **(a)** positive ion spectrum.; **(b)** negative ion spectrum.

XPS spectra confirms the presence of Al oxides at the surface of a Cu | Al film, in agreement with XPS spectra of Cu | Al films reported by Tyler *et al.* after this work.[190] Figure 3.7 shows the presence of Cu and AlO_x, at the surface of the film. Cu(II) is not present, although Cu(I) oxide cannot be ruled out by these spectra alone.[190]

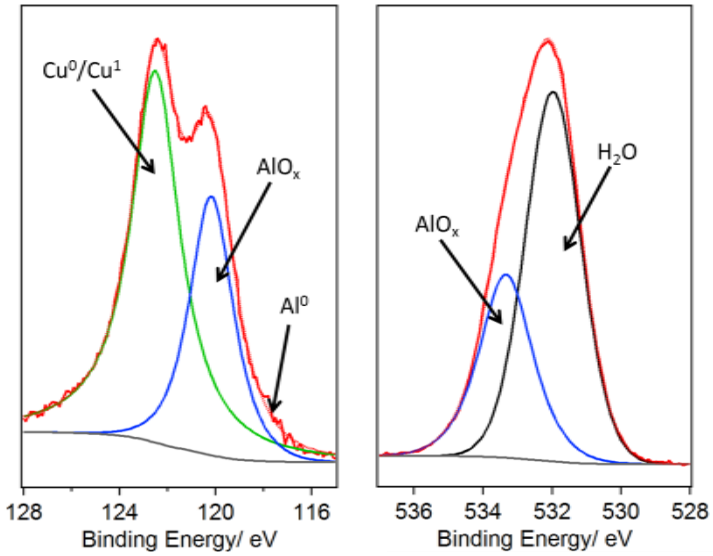

Figure 3.7: Al2*s* / Cu3*s* (left) and *O1s* (right) *XPS* spectra of a Cu 8 nm | Al 0.8 nm film after 75 minutes oxidation. Raw data, total fit and background are coloured red, dotted red and grey respectively. Fitted peaks for Cu, AlO_x, and atmospheric H_2O are coloured green, blue, and black respectively.

Work Function measurements made using a Kelvin Probe co-located in the same glove box as the evaporator corroborate this conclusion, since the work function of oxidised Cu 7 nm | Al 0.8 nm films, 3.78 ± 0.02 eV (Figure 3.3), which is too high to be Al_2O_3 (3.45 ± 0.02 eV) (Figure 3.3) and too low to be Al (4.33 eV),[174] Cu (4.6 eV)[156] or CuO (4.54 ± 0.02 eV). It is evident from Figure 3.3 that the work function of the Cu | Al electrode is very low to begin with (3.11 eV) and after an initial very rapid increase converges to 3.78 eV. This very low starting value is not unexpected, since Al_2O_3 has a

low work function of ~3.2 eV (Figure 3.3) and it is known that an extremely thin oxide layer forms at the surface of freshly evaporated Al films within minutes at 10^{-6} mbar (i.e. high vacuum) due to the very high reactivity of Al towards O_2.[191] When exposed to the glove box environment, which is ~1 ppm O_2, a very thin oxide layer is therefore expected to form extremely rapidly. Importantly, when the work function and sheet resistance evolve with oxidation the surface roughness of the films remain essentially unchanged at an exceptionally low root-mean-square value of ≤0.6 nm, as shown in Figure 3.8. This is much lower than most conducting oxide electrodes at 2-3 nm.[192]

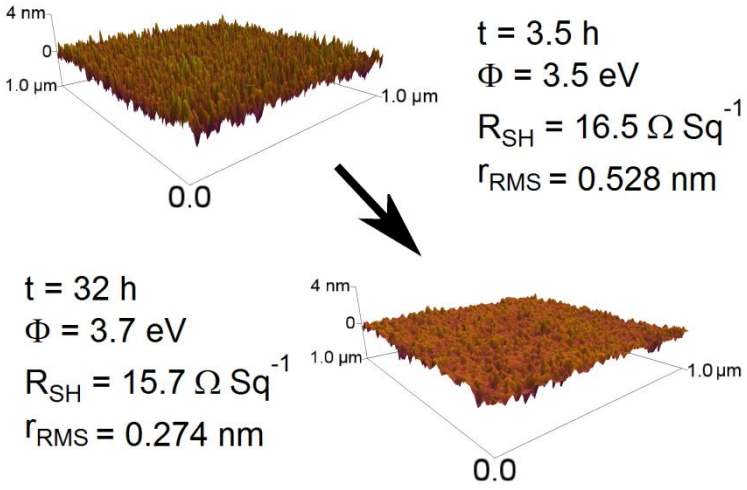

Figure 3.8: 3-dimensional AFM scans of Cu 7 nm | Al 0.8 nm films on APTMS:MPTMS derivatized glass that have been in air for 3.5 hours (top left) and 32 hours (bottom right). The work function, sheet resistance (R_{SH}) and root-mean-squared roughness (r_{RMS}) at these two time intervals are given to show that work function and sheet resistance evolve due to surface oxidation whilst roughness remains essentially unchanged.

Furthermore, these electrodes are robust towards ultra-sonic agitation in toluene, isopropanol and water, with less than 2% increase in sheet resistance, as shown in Table 3.1.

Process	R_{SH} / Ω sq^{-1}
Before ultra-sonic agitation	15.4 ± 0.1
Toluene	15.6 ± 0.1
Isopropanol	15.6 ± 0.1
Water	15.6 ± 0.1

Table 3.1: Sheet Resistance of a Cu 7 nm | Al 0.8 nm film after ultra-sonic agitation in various solvents for 10 minutes.

The low work function and very low surface roughness of the Cu | Al 0.8 nm films combined with the decrease in sheet resistance upon oxidation and capacity to mop up oxygen/water bodes well for application as a transparent electron-extracting electrode and a built-in desiccant for oxygen in OPVs. For this application, the oxide layer formed at the electrode upon *in-situ* oxidation must however remain sufficiently thin to be transparent to the flow of electrons across the electrode - organic semiconductor interface and the change in work function must not adversely impact the efficiency of electron-extraction to the external circuit.

To demonstrate utility in OPVs the electrode was incorporated into model inverted OPVs with the structure: Cu 7 nm | Al 0.8 nm | PCDTBT/$PC_{70}BM$ | MoO_3 10 nm | Al 70 nm. A 7 nm Cu film was chosen because the sheet resistance is comparable to that of the ITO coated glass used in our laboratory for OPVs; 15 Ω sq^{-1}. Whilst, the *PCE* of OPVs using a 7 nm Cu electrode (~4.0%) is ~15% lower than that achieved using a conventional ITO electrode (~4.7%), due to the lower transparency of the former (Figure 3.2), it is important to note that in this study optical spacers have not been employed to maximise micro-cavity effects. All devices were fabricated in a nitrogen filled glove box

with ~1 ppm O_2 and H_2O. *In-situ* oxidation of the electrode was achieved by storing the entire OPV in air at one atmosphere, standardised test protocol ISOS-D-1 Shelf,[193] for 69 hours. Due to the low thickness of the Cu | Al electrode it is possible to monitor the extent of oxidation at the buried interface between the electron-extracting electrode and PCDTBT/PC_{70}BM layer *via* the decrease in resistance of the electrode. The beauty of this non-destructive *in-situ* measurement lies not only in its simplicity but in the fact that it allows changes in the state of the electrode surface to be probed independently of other changes in the OPV such as oxidation or doping of the photoactive layer.

It is well documented that the characteristics of un-encapsulated organic optoelectronic devices stored in air changes on the time scale of minutes to hours due to the ingress of water and molecular oxygen into the organic semiconductor layer(s) and oxidation of the low work function electrode.[73,166,170,171] Since the top metal contact slows the rate of diffusion into the organic semiconductor[166] the OPVs fabricated in this study have a relatively small active area; ~0.13 cm^2, to help ensure rapid air ingress. Figure 3.9 shows representative *JV* characteristics for an OPV before and after storage in air for 69 hours. The 6% decrease in resistance of the electrode from 9.72 to 9.19 Ω, measured using the two point method indicates that the surface of the Cu | Al electrode has oxidised to a significant extent due to air ingress through the photoactive layer. The resistance of a reference comprising a Cu | Al electrode of identical geometry covered with a PCDTBT/PC_{70}BM layer but without a top electrode also exhibited a 6% change confirming that the whole electrode surface is oxidised and not just the area near to the edges of the top electrode in OPV devices.

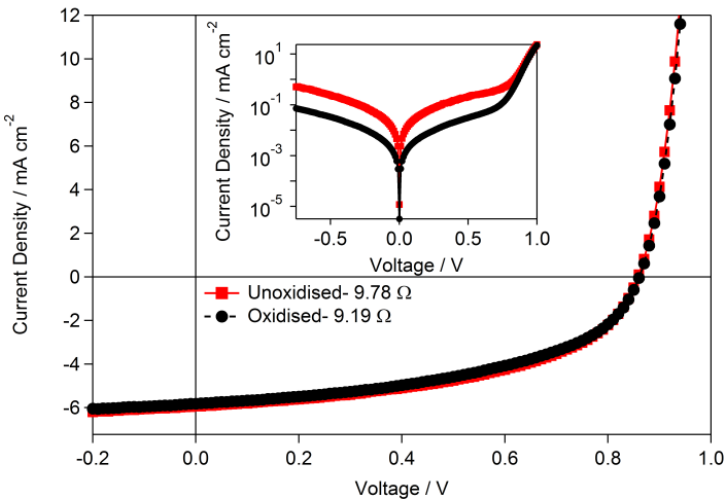

Figure 3.9: Typical *JV* characteristics for OPVs with the structure: Cu 7 nm | Al 0.8 nm | PCDTBT/$PC_{70}BM$ | MoO_3 10 nm | Al 70 nm in the dark (inset) and under 1 sun illumination, both before and after oxidation in air at 1 bar for 69 hours. Notably the resistance was measured using the two point method so the measured resistance is not directly comparable to the sheet resistance.

Crucially, this *in-situ* oxidation of the electrode at the buried interface with the photoactive organic semiconductor layer does not adversely impact J_{sc}, *FF* or V_{oc}, which remain constant at ~5.9 mA cm^{-2}, ~0.50 and ~0.86 V respectively. In fact, there is an order of magnitude decrease in the reverse dark current at -0.75 V which represents a large improvement in the dark *JV* characteristic according to the ideal diode equation:[194]

$$V_{oc} \approx \frac{nkT}{q}\ln\left(\frac{J_{sc}}{J_s}\right) \qquad \textbf{Equation 3.1}$$

Where V_{oc} is the open circuit voltage, n is the diode ideality factor, k is the Boltzmann constant, T is the temperature, q is the fundamental charge, J_{sc} is the short circuit current and J_s is the reverse saturation current. The improvement in dark current characteristics shown in Figure 3.9 have been observed before in OPV systems

employing a thin NiO_x interlayer.[195] OPVs fabricated in a nitrogen atmosphere on pre-oxidised Cu | Al 0.8 nm electrodes exhibit the same improvement in dark *JV* characteristic which remains unchanged upon storage in air, ruling out the possibility that doping of the photoactive layer by oxygen is responsible for the improvement in dark *JV* characteristics (Figure 3.10).

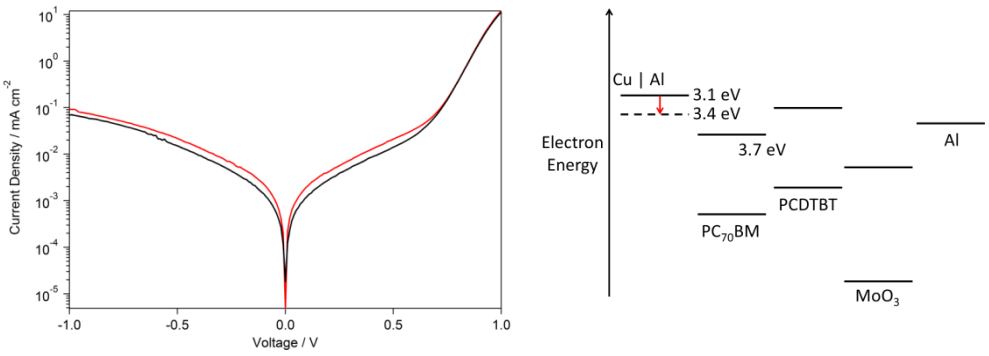

Figure 3.10: Left: Typical *JV* characteristics for OPVs with the structure: Cu 7 nm | Al 0.8 nm | PCDTBT/$PC_{70}BM$ | MoO_3 10 nm | Al 70 nm in the dark. Red: Device fabricated in a nitrogen atmosphere on a pre-oxidised Cu | Al electrode. Black: Device fabricated in a nitrogen atmosphere on a pre-oxidised electrode and stored in air for 20 hrs. Right: Flat band schematic energy level diagram for the OPVs, illustrating the change in electrode work function.

Since the PCDTBT/$PC_{70}BM$ layer is deposited immediately after removal of the Cu | Al electrode from the vacuum chamber, the 6% reduction in sheet resistance of the electrode translates to a 300-350 meV increase in work function of the electron-extracting electrode from 3.11 to 3.43 eV (Figure 3.3). However, since the work function of the electrode remains less than or equal to the electron affinity of $PC_{70}BM$ (3.7 eV)[196] it can be assumed that the degree of alignment between the electrode Fermi level and the LUMO of $PC_{70}BM$ remains unchanged, since ground state charge transfer from the

electrode to $PC_{70}BM$ LUMO will occur pinning the LUMO near to the electrode Fermi level (Figure 3.10). It is not clear at this stage as to why the dark current characteristics improve so dramatically upon formation of the oxide layer. This improvement does not however translate to an increase in V_{oc}[194] as expected according to the ideal diode equation, because it is already at the maximum achievable for this material system.[82]

To further demonstrate the stability of this electrode, degradation measurements were undertaken for encapsulated OPVs. The molecular materials of C_{60} and SubPc were used as they are known to be very stable. Single junction evaporated small molecule cells with an active area of 1 cm^2 were fabricated and the *JV* responses are shown in Figure 3.11 and Table 3.2.

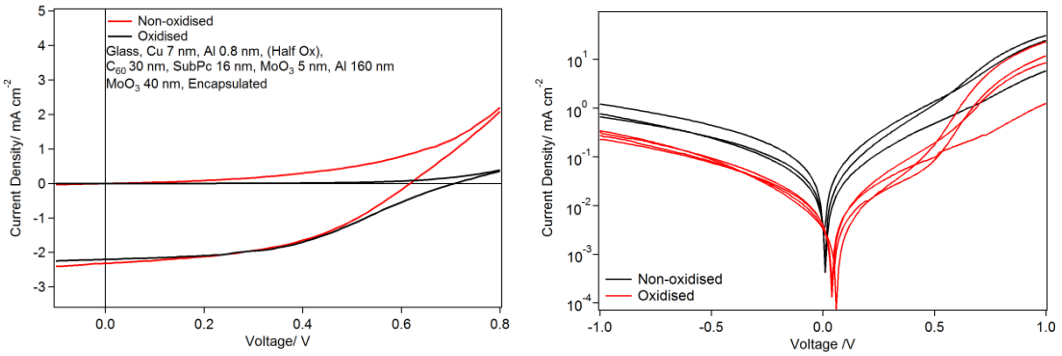

Figure 3.11: Left: *JV* characteristics for devices with the structure: Glass | SAM | Cu 7 nm | Al 0.8 nm | C_{60} 30 nm | SubPc 16 nm | MoO_3 5 nm | Al 160 nm | MoO_3 40 nm. The devices were encapsulated and tested in air immediately after fabrication. Right: Typical *JV* characteristics for the same OPVs in the dark. Red: Devices fabricated on pre-oxidised Cu | Al electrodes. Black: Devices fabricated on unoxidised electrodes.

Window electrode	J_{sc}/ mA cm^{-2}	V_{oc}/ V	*FF*	*PCE*/ %
Non-oxidised	2.3 ± 0.1	0.51 ± 0.08	0.42 ± 0.06	0.5 ± 0.1
Oxidised	2.17 ± 0.06	0.64 ± 0.05	0.43 ± 0.06	0.6 ± 0.1

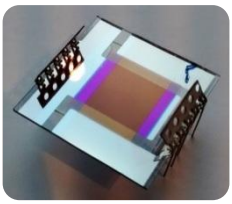

Table 3.2: Left: *JV* data for the OPV devices shown in Figure 3.11. Device architectures: Glass | SAM | Cu 7 nm | Al 0.8 nm | C_{60} 30 nm | SubPc 16 nm | MoO_3 5 nm | Al 160 nm | MoO_3 40 nm. Right: Photograph of a 1cm^2 device.

The increase in V_{oc} for the OPVs in Figure 3.11 and Table 3.2 can be explained with reference to the reverse saturation current: Since the V_{oc} is not at the maximum obtainable for this system for devices fabricated on unoxidised electrodes, an increase in V_{oc} is to be expected when considering the ideal diode equation (Equation 3.1). After encapsulation and testing, these cells were then loaded onto a long term degradation rig, and the *JV* characteristics were recorded successively as the cells underwent degradation in air under illumination. The results are shown in Figure 3.12. It is important to note that the long term degradation testing rig used to generate the data shown in Figure 3.12 uses commercially available spotlight bulbs instead of a AM1.5 lamp source. The intensity was measured using a photodiode for each cell and was always 100 ± 8 mW cm^{-2}. Although these OPVs were encapsulated, there is an inevitable ingress of oxygen and water into the devices whilst testing in air.

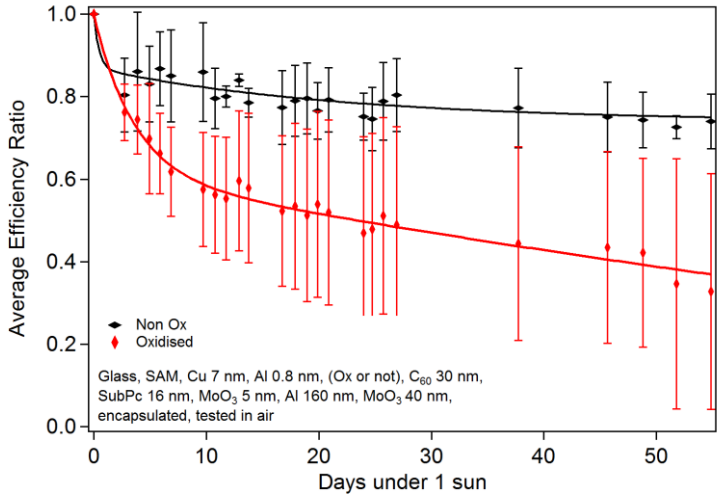

Figure 3.12: Average efficiency ratio values as a function of time under 1 sun for OPV cells fabricated on oxidised (18 hrs) and non-oxidised Cu | Al electrodes. Full device structures were as follows: Glass | SAM | Cu 7 nm | Al 0.8 nm | C_{60} 30 nm | SubPc 16 nm | MoO_3 5 nm | Al 160 nm | MoO_3 40 nm. The devices were encapsulated and tested in air. Data points are shown with an exponential decay data fit to guide the eye.

The degradation of OPVs occurs as a result of a number of parallel mechanisms, although many are known to result from the ingress of oxygen and water into the photoactive layer. Figure 3.12 shows that the initial efficiency of devices using Cu | Al electrodes is very similar, consistent with the results for polymeric devices. The LUMO of C_{60} is 4.5 eV[73] and so again the change in the work function of the electrode upon oxidation is not expected to result in reduced *PCE*. However, the devices fabricated on non-oxidised electrodes last much longer that those fabricated on oxidised electrodes, consistent with the oxygen desiccant property of this electrode system.

3.5 Conclusions

These Glass | SAM | Cu 8 nm | Al 0.8 nm window electrodes are fabricated from low cost materials and simultaneously remove the requirement for a conducting oxide window electrode and a conventional low work function electrode. When the electrode is exposed to air, an ultra-thin self-limiting ternary oxide layer forms at its surface without any increase in surface roughness and the sheet resistance of the electrode actually decreases; thereby improving the electrical properties of the electrode. This is in stark contrast to ultra-thin Cu films on identical substrates, where the sheet resistance increases in air with oxidation. It is shown that oxidation of the electrode surface at the buried interface does not adversely impact the efficiency of electron extraction, even though the work function increases by several hundred milli-electron volts from a very low starting value of ~3.1 eV to a maximum of ~3.8 eV. These electrodes scavenge oxygen/water that permeates into the photoactive layer which is particularly important for OPVs since organic semiconductors are particularly susceptible to damage by low levels of molecular oxygen and the desiccant layer is in direct contact with the organic semiconductor layer. However, this electrode has the disadvantage of a lower far-field transparency than the industry standard; ITO glass.

Chapter 4 – Hybrid Copper: Doped Tungsten Sub-oxide Window Electrodes

The majority of the work presented in this chapter has been published in the following paper:

"*A Hybrid Copper:Tungsten Suboxide Window Electrode for Organic Photovoltaics*" O.S. Hutter, R. A. Hatton, *Adv. Mater.* **2015**, *27*, 326.

4.1 Abstract

This chapter describes a window electrode for OPVs based on an ultra-thin bilayer of Cu and amorphous tungsten sub-oxide, which derives its remarkable optical and electrical properties from spontaneous solid state diffusion of Cu into the oxide layer. This unpatterned Cu electrode performs as well as ITO coated glass in ~6% efficient inverted OPVs, in part by trapping light in a resonant optical cavity. The sheet resistance of this electrode is exceptionally low at 6-7 Ω sq^{-1}, and the transparency maxima is well-matched to the peak of the solar photon flux and thus to narrow band gap polymers and non-fullerene electron acceptors.

4.2 Background

In recent years there has been renewed interest in the use of unpatterned optically thin metal films as window electrodes in OPVs owing to their simplicity, ease of manufacture using the well-established industrial process of roll-to-roll thermal evaporation, and compatibility with flexible substrates.[147,197-199] This resurgence was initiated by O'Connor

et al.[147] who showed, using optical modeling, that thin Ag film electrodes have the potential to outperform conventional conducting oxide electrodes in OPVs without the need for texturing or patterning of the electrode. Using a concept borrowed from low emissivity glass, the far-field transparency of thin metal films can also be greatly improved by sandwiching the metal between oxide layers, to create a triple layer electrode structure.[82,157] Using this approach Sergeant *et al.* have shown that Ag window electrodes with the structure MoO_3 | Ag 6 nm | MoO_3 can perform as well as ITO glass in 4.4% efficient OPVs.[82] In that work the substrate was cooled to -5^{o}C during metal deposition in order to realise a continuous Ag film at such low thickness. Ag is the metal of choice for triple layer oxide-metal-oxide electrodes since it has the highest electrical conductivity amongst metals and the lowest optical absorption.[115,147,200] However, for a large reduction in the cost of the window electrode as compared to low cost conducting oxides such as fluorine doped zinc oxide[201] a much cheaper metal is required and the fabrication process must be simplified. Cu is attractive as a replacement for Ag owing to its comparable electrical conductivity[157] at ~1% of the cost, and is 1000 times more abundant,[84] although the performance of Cu triple layer window electrodes in OPVs has thus far proved to be relatively poor as compared to identical devices employing an ITO electrode, with *PCE*s between 0.22-3.4%.[157,159]

Chapter 3 describes how optically thin, exceptionally robust Cu films with a sub-1 nm surface roughness can be fabricated on glass substrates using a molecular adhesive layer and how metal films can be passivated toward oxidation in air by capping with an 0.8 nm layer of Al which forms a self-limiting sub-1 nm oxide.[203] The disadvantage of this electrode is its ~30% lower far-field transparency across the visible spectrum as compared to ITO glass.[203]

This chapter shows how a layer of sub-stoichiometric tungsten oxide (WO_{3-x}) sequentially deposited onto an 8 nm thick Cu film by vacuum evaporation imparts an exceptionally large improvement in far-field transparency in the important wavelength range for PV applications between 550-900 nm and a reduction in electrode sheet resistance.

4.3 Experimental

Preparation of ultra-thin Cu | WO_{3-x} films on glass: Glass substrates were cleaned as described in Chapter 2, UV/O_3 and a mixed molecular adhesive layer of APTMS and MPTMS was deposited from the vapour phase at reduced pressure 50 mbar for 4 hours. Importantly the APTMS was stored at room temperature prior to use. Tungsten oxide (Aldrich, 99.995%) and molybdenum (Aldrich, 99.995%) oxide were thermally evaporated at a rate of 0.1-0.2 $Å s^{-1}$. To fully convert the tungsten oxide powder in the boron nitride crucible into the black sub-oxide (WO_{3-x}) the tungsten boat is heated at a vacuum pressure of 1×10^{-5} mbar at the onset temperature for sublimation for a period of 30 minutes prior to deposition onto a substrate. The sublimation temperature of tungsten oxide powder at this pressure could not be measured but is ~1000 °C.[202] OPVs fabricated using stoichiometric WO_3, (i.e. without preheating) did not function.

Characterisation: All device and thin film characterisation was carried out using equipment described in Chapter 2. The samples for UPS and XPS were briefly exposed to the laboratory environment prior to loading into the ultra-high vacuum system. The thickness of the PTB7/PC_{70}BM layer used in devices was calculated by scoring devices, recording AFM scans and averaging the cross section data. An example scan of this process is shown in Figure 4.1. Knowledge of the active layer thickness is necessary for optical modeling (Figure 4.16).

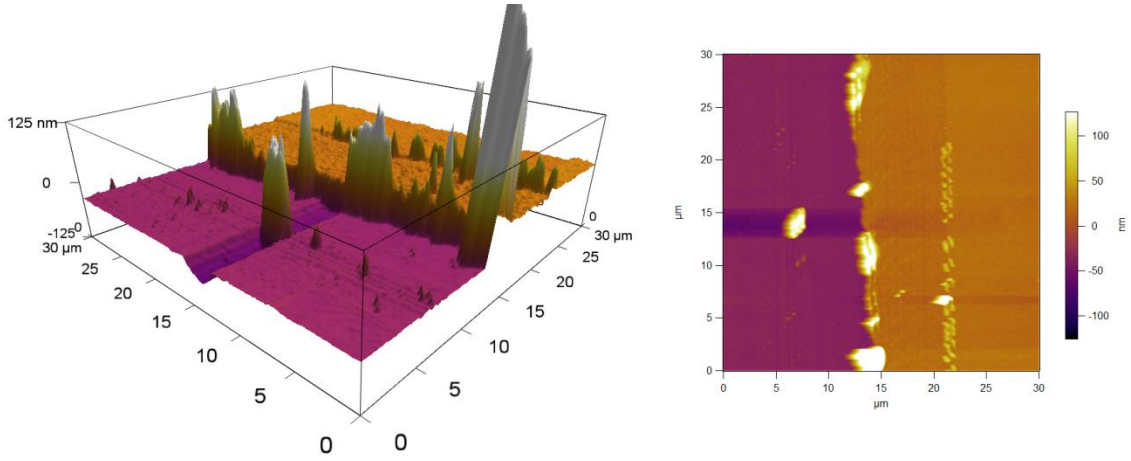

Figure 4.1: AFM scans shown in 3-D (left) and 2-D (right) of a scratched Glass | SAM | Cu 8 nm | WO_{3-x} 5 nm | Al 1.0 nm | PTB7/ $PC_{70}BM$ films.

To ensure the wooden stem only scratched through the polymer layer and not the Cu | WO_{3-x} layer, a Glass | SAM | Cu 8 nm | WO_{3-x} 20 nm film was scratched with the same wooden stem and AFM scans of the films were recorded. As shown in Figure 4.2, the wooden stem did not scratch through the Cu or WO_{3-x} layers, confirming that the calculated thickness used for the devices was correct. The mark that the wooden stem left is clearly visible on Figure 4.2, but the Cu film was not damaged through to the glass.

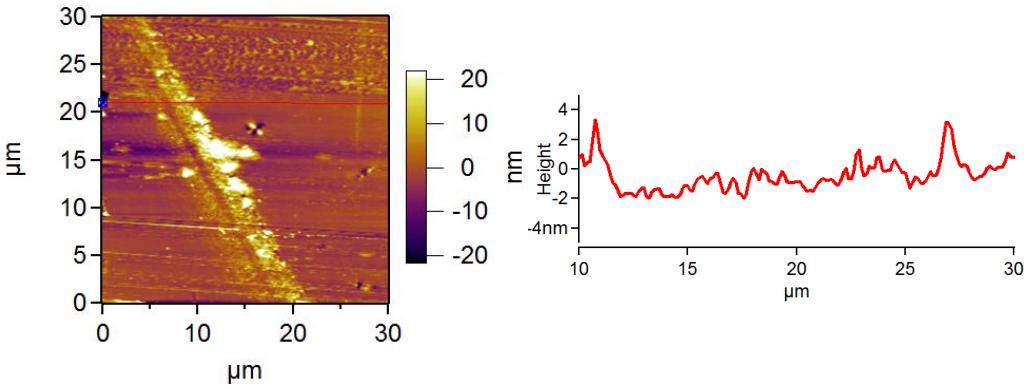

Figure 4.2: 2-D AFM image of a Glass | SAM | Cu 8 nm | WO_{3-x} 20 nm film after being scratched with a wooden stem. The mark left by the wooden stem is clearly visible. The red line of the AFM image illustrates where the cross section of the image was taken.

4.4 Results and Discussion

Figure 4.3 illustrates that the transparency of the Cu film is increased by up to 22% (Figure 4.3 (black arrow)) upon deposition of the 20 nm WO_{3-x} layer. WO_{3-x} was chosen for its high refractive index, with the layer thickness being chosen as a compromise of the increased transparency predicted by optical modeling, and the limited device functionality that results with increasing thickness of a semiconducting interlayer.

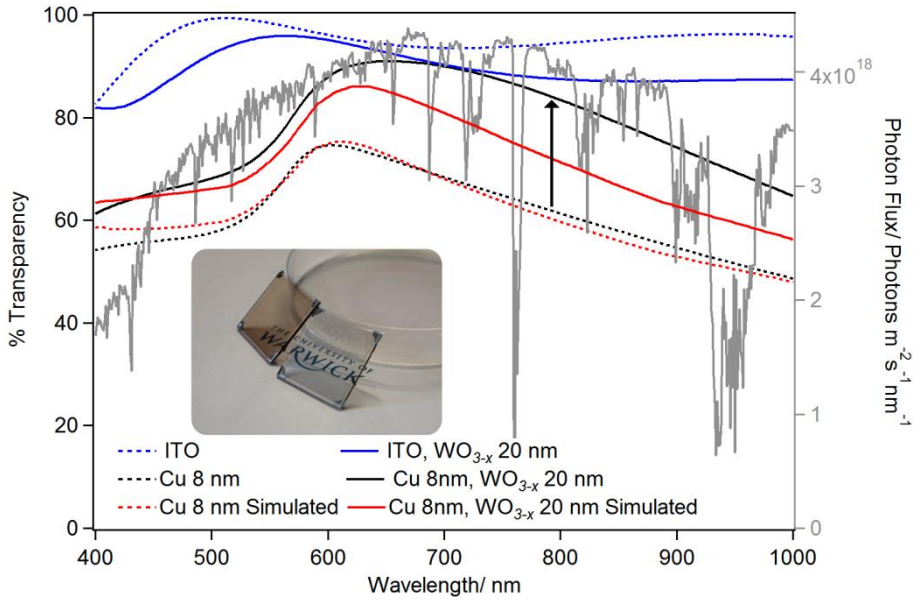

Figure 4.3: UV/Visible spectra showing the far-field transparency of various electrodes with light incident through the glass substrate, as is the case in an OPV. The AM1.5G

solar photon flux is overlaid in grey. Graphs from the top down: ITO 145 nm (dashed blue), ITO | WO_{3-x} 20 nm (solid blue), Cu 8 nm | WO_{3-x} 20 nm (solid black), Cu 8 nm | WO_{3-x} 20 nm simulated (solid red), Cu 8 nm (dashed black) and Cu 8 nm simulated (dashed red) films on glass. Inset: Photograph of Cu 8 nm on glass (left) and Cu 8 nm | WO_{3-x} 20 nm on glass (right), showing the difference in colour and transparency.

The far-field transparency of the Cu 8 nm | WO_{3-x} 20 nm bilayer film, along with that of a number of references is shown in Figure 4.3 along with the results of plane wave optical modeling using commercial software[212] based on the transfer matrix method. The optical model assumes discrete layers of glass, Cu, ITO and WO_{3-x} and the bulk dielectric function of Cu. The good agreement between the simulated and measured transparency of the 8 nm Cu film (Figure 4.3, red & black dotted lines) is consistent with description of a uniform slab of Cu with a thickness of 8 nm. The optical model also accurately predicts the transparency of a 20 nm WO_{3-x} film (Figure 4.4) using literature values for the optical constants.[213] In contrast, the model greatly underestimates the transparency of the Cu | WO_{3-x} electrode by as much as 13% for $\lambda > 625$ nm (Figure 4.3), a disparity that cannot be rationalized in terms of suppression of parasitic plasmonic absorption by the oxide overlayer[214] because the model does not account for losses due to surface plasmon excitation.

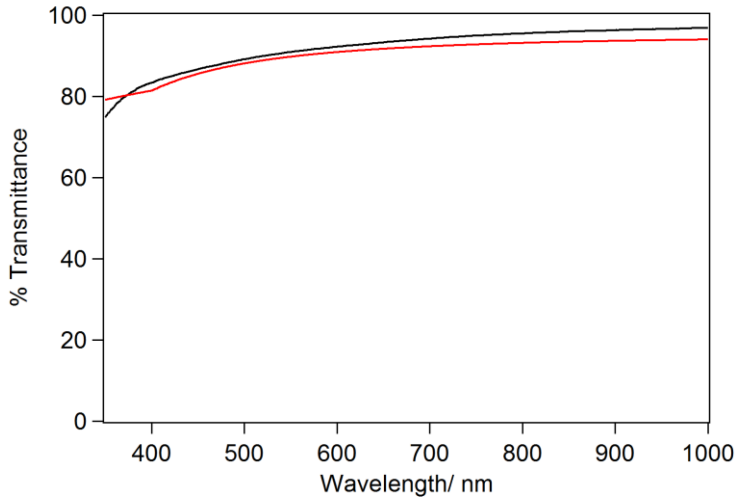

Figure 4.4: The transparency of a 20 nm WO_{3-x} film (black) and the simulated transparency of the same film (red). The simulation was performed using The Essential Macleod software[212] and the optical constants were taken from the literature.[213]

In Figure 4.3, the transparency of the Cu | WO_{3-x} film is compared to the transparency of ITO with a sheet resistance of 15 Ω sq^{-1}, and the sheet resistance of the Cu | WO_{3-x} film is 6-7 Ω sq^{-1}. Notably, if the sheet resistance of the ITO glass used in this work was reduced to that of the Cu | WO_{3-x} electrode by increasing the ITO layer thickness and/or dopant density the far-field transparency is reduced[204,205] in that region of the spectrum where the solar photon flux is greatest, closing the transparency gap between the Cu | WO_{3-x} and ITO electrodes. For window electrodes in OPVs, a sheet resistance below 10 Ω sq^{-1} is required,[90] and it is therefore fitting to compare the transparency of the Cu | WO_{3-x} film to ITO with a sheet resistance of 6 Ω sq^{-1} (Figure 4.5).

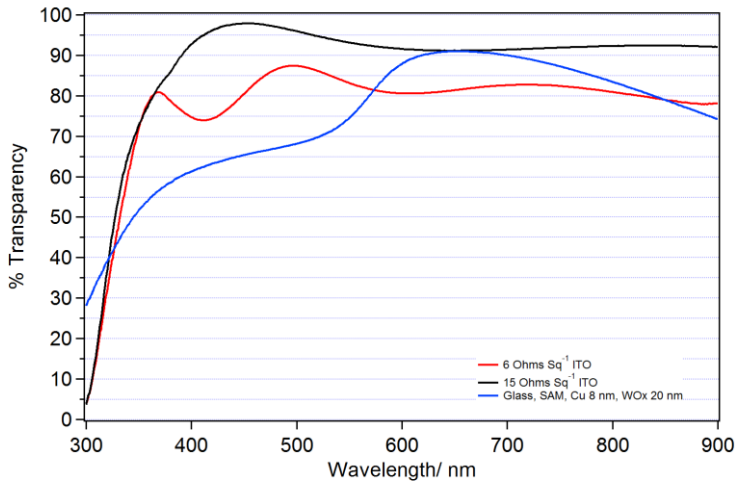

Figure 4.5: UV/Visible spectra showing the far-field transparency of ITO at 15 Ω sq^{-1} (black), ITO at 6 Ω sq^{-1} (red) and Cu | WO_{3-x} at 6-7 Ω sq^{-1} (blue) on glass.

Figure 4.5 illustrates that between 550-850 nm, the transparency of the Cu | WO_{3-x} film is actually higher than that of an ITO film with similar sheet resistance. To achieve the observed increase in transparency for the Cu | WO_{3-x} films, it is necessary to convert stoichiometric tungsten oxide (WO_3), which is yellow in colour, into the black sub-oxide phase (WO_{3-x}) by heating at the sublimation onset temperature for a period of 30 minutes prior to deposition onto the Cu substrate. WO_3 is a wide band gap oxide with a conduction band (CB) comprising W 5d states and is known to form oxygen vacancy defects upon heating, which gives rise to occupied gap-states from which electrons can easily be prompted to the CB.[206] Direct evidence for significant oxygen deficiency in films evaporated from the black phase is provided by core and valence band photoelectron spectroscopy of a WO_{3-x} film supported on a gold coated substrate (Figure 4.6), which shows that 4.9 ± 0.5% of the tungsten atoms are in the 5+ oxidation state - which corresponds to $WO_{2.95}$ - and the presence of a significant density of occupied states in the band gap.

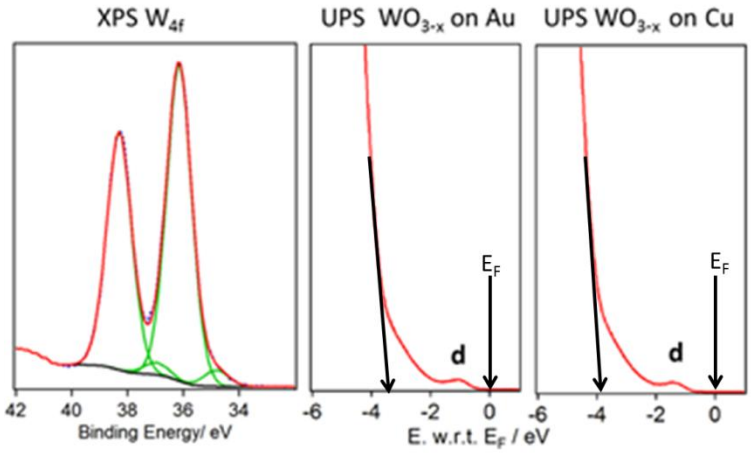

Figure 4.6: High resolution XPS spectrum of the W4*f* region (left) of a WO_{3-x} film supported on Au. There is no evidence for Au in the XPS spectrum (not shown). The W4*f* peaks are well fitted with two doublets. The most intense doublet is attributed to the W^{6+} and the weaker doublet, at lower binding energy, to the W^{5+}, which indicates that the oxide is sub-stoichiometric.[207-209]; **(middle and right)** UPS spectra showing the valence band edge regions for a WO_{3-x} film on Au (**middle**) and WO_{3-x} film on 8 nm Cu film (**right**). The peak at ~1 eV below the Fermi level, labeled **d**, can be attributed to a partially occupied W 5d orbitals within the band gap.[210,211] The energy of the Fermi level (E_F) and extrapolation to determine the energy of the valence band edge with respect to the Fermi level are also shown.

The UPS results in Figure 4.6 show that the energy difference between the VB edge and E_f is increased by 0.4 eV when the WO_{3-x} film is deposited on Cu as compared to the same film on Au. This change in chemical potential is indicative of significant *n*-type doping since E_f has moved closer to the CB. The reported work function of evaporated tungsten oxide varies wildly from 4.9 eV to 6.9 eV, reflecting its high sensitivity to the degree of oxygen deficiency and thus to the deposition conditions.[219] However, in general the work function is expected to decrease as the average oxidation

state decreases.[40] In this case the oxide is pre-heated to convert it to the oxygen deficient black phase and so the work function can be expected to be low. The work function (Φ) of Cu | WO_{3-x} and Au | WO_{3-x} films, measured using a Kelvin probe located in the same nitrogen-filled glove box as the thermal evaporator, was 5.12 ± 0.02 eV and 4.96 ± 0.01 eV respectively. Table 4.1 shows the work function of Cu and Cu | WO_{3-x} electrodes.

Sample	Fresh Work Function/ eV	Work Function after overnight in evaporator/ eV	Work Function after overnight in evaporator and 1 min dry air oxidation/ eV
Glass | SAM | Cu 8 nm	4.87 ± 0.02	4.68 ± 0.01	4.91 ± 0.03
Glass | SAM | Cu 8 nm | WO_{3-x} 5 nm	5.31 ± 0.03	5.02 ± 0.02	5.03 ± 0.02
Glass | SAM | Cu 8 nm | WO_{3-x} 20 nm	5.32 ± 0.01	5.12 ± 0.02	4.68 ± 0.01

Table 4.1: Work function values recorded using the kelvin probe technique for WO_{3-x} of differing thicknesses on Cu.

Since work function changes can result from changes in both chemical and surface potential it is possible that the reduction in chemical potential due to Cu doping is more than off-set by an increase in surface potential. The latter would be expected to increase due to the increased density of conduction band electrons (provided by the Cu dopants), which spill into the vacuum giving rise to the surface dipole.[20] The work function value for WO_{3-x} on Au is in good agreement with that reported by Lee *et al.*[220] and Fang *et al.*,[221] although significantly lower than reported for WO_{3-x} deposited using the hot wire vapor deposition method, 5.3 eV,[222] or WO_3 films deposited and probed

under ultra-high vacuum conditions; 6.7 eV.[223] This difference is possibly due to physisorption of very low levels of gaseous solvent molecules in our glove box, since the work function of transition metal oxides is known to be reduced by surface contaminants via the push-back effect.[20,223]

In addition to the unexpectedly high far-field transparency over a large portion of the solar spectrum, the sheet resistance of the bi-layer electrode is exceptionally low at 6-7 Ω sq^{-1}. This is primarily due to the low resistance of the 8 nm Cu film, which to my knowledge is the lowest of any unpatterned Cu film reported to date - and is achieved using an adaptation of the molecular adhesive approach used in Chapter 3, the details of which are given in the experiment section. Importantly, upon WO_{3-x} deposition onto an 8 nm Cu film the sheet resistance is typically reduced by ~0.2 Ω sq^{-1} within ~1 hour. Figure 4.7 shows evolution of the sheet resistance of a Cu 5.5 nm | WO_{3-x} 20 nm film under nitrogen immediately after deposition. Whilst this reduction is not significant for lateral conduction it indicates that the resistivity of the 20 nm WO_{3-x} overlayer is exceptionally high, since the conductivity of evaporated WO_{3-x} [1×10^{-7} $(\Omega\ cm)^{-1}$ [215,110]] is at least 5 orders of magnitude lower than that of an 8 nm Cu film [7.5×10^{5} $(\Omega\ cm)^{-1}$].

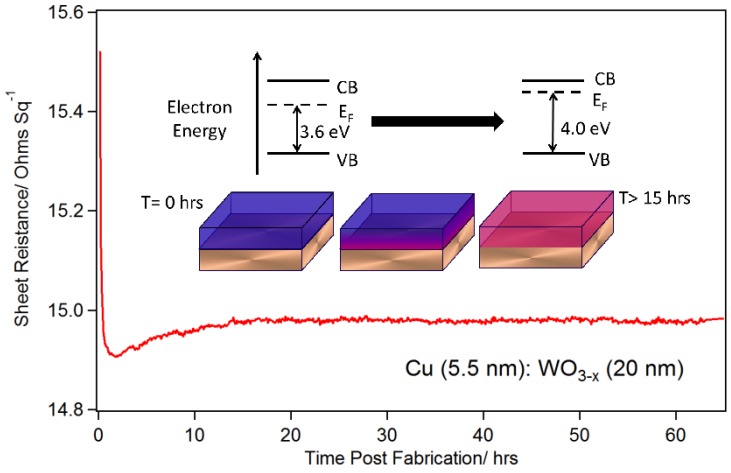

Figure 4.7: Sheet resistance as a function of time in the glove box for a Cu 5.5 nm | WO_{3-x} 20 nm film. **Inset**: Schematic illustration and energy level diagram for a 20 nm WO_{3-x} film before and after Cu doping. The energy levels have been deduced from UPS measurements of WO_{3-x} films on Au and Cu substrates. Because Au does not diffuse into the WO_{3-x} over layer the energy levels for this case correspond to the *before doping* scenario.

Since doping of the WO_{3-x} layer gives rise to a measureable change in the sheet resistance of the bilayer electrode it is possible to indirectly observe the kinetics of Cu diffusion into the oxide *via* the time dependence of changes in the sheet resistance post oxide deposition. This effect is amplified if the metal thickness is reduced, as is evident from Figure 4.7 which gives the sheet resistance change for a 5.5 nm Cu film. It is clear from Figure 4.7 that diffusion of Cu into the WO_{3-x} over layer saturates after 15 hours, although most of the diffusion occurs within the first hour. It is likely that such rapid diffusion of Cu into the WO_{3-x} layer at room temperature is enabled by the coincidence of the very high ionic conductivity of Cu[102] and the nano-porous structure of WO_{3-x} films that results from the high degree of disorder.[106,215,216] The simplest explanation for this

increase in conductivity is diffusion of Cu into the oxide layer where it functions as an *n*-type dopant as schematically illustrated in the inset of Figure 4.7. In this context the extra electrons provided by the Cu atoms would be expected to reduce some W^{6+} to W^{5+}. Direct experimental evidence for spontaneous Cu diffusion into the WO_{3-x} over layer is provided by high resolution XPS analysis of the surface of a 20 nm WO_{3-x} film on an 8 nm Cu film, the results of which are summarized in Figure 4.8 and Table 4.2.

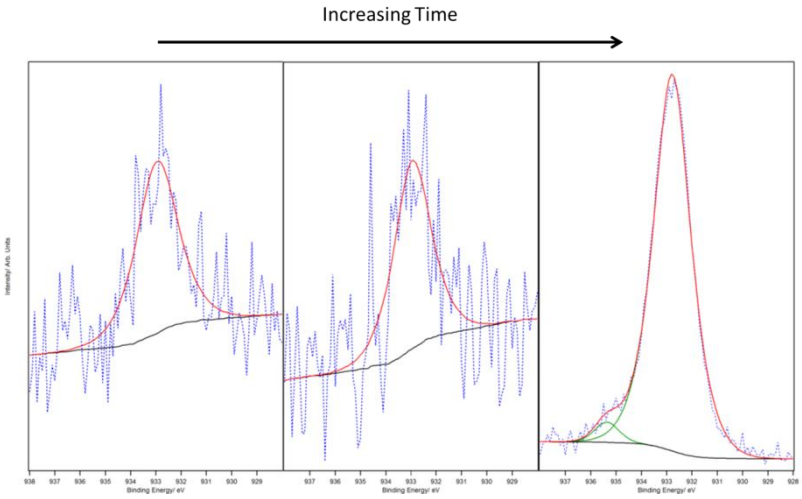

Figure 4.8: Cu2*p* XPS spectra of the Cu 8 nm | WO_{3-x} 20 nm films with various air exposure times, 0 hr, 1 hr and 24 hrs from left to right. Raw data, fitted peaks, total fit and background are coloured dotted blue, green, red and black respectively.

	WO_3	WO_{3-x}	W	Cu	Cu Oxide
Sample	**Atomic %**				
Non Ox	95.0 ± 0.5%	4.4 ± 0.5%	0%	0.6 ± 0.1%	0%
1 hr Ox	96.4 ± 0.5%	3.3 ± 0.5%	0%	0.4 ± 0.1%	0%
24 hr Ox	91.3 ± 0.5%	0%	0%	8.4 ± 0.5%	0.3 ± 0.1%

Table 4.2: XPS analysis of the surface of 20 nm WO_{3-x} film on an 8 nm Cu film. The sampling depth is estimated to be ~7 nm as the mean free path of the electrons in the

material and the beer-lambert law demonstrate 95% of the signal emanates from within this distance. Atomic percentages were calculated using ratios of areas under modelled peaks, taking account of the relative sensitivity factors. The oxidation state of Cu is not specified because of the difficulty in differentiating between $2p_{3/2}$ peaks associated with Cu^0 and Cu^{+1} in copper oxides.[217]

It is evident from Figure 4.7 that Cu diffusion into the WO_{3-x} layer is not complete until ≈15 hours after oxide deposition and so all photoelectron spectroscopy and work function measurements were made after ≥ 15 hours storage under high vacuum (~10^{-6} mbar) inside a vacuum evaporator located inside a nitrogen filled glove box (<5 ppm O_2 and H_2O). Evidence for its role as an *n*-type dopant is provided by ultra-violet photoelectron spectroscopy (UPS) measurements (Figure 4.6), from which the position of the Fermi level (E_f) with respect to the valence band edge (VB) can be determined. XPS analysis of Cu samples (Figure 4.8) can be challenging due to peak asymmetries and overlap of binding energy positions, with the Cu_2O and metallic Cu in the Cu2$p_{3/2}$ region being separated by 0.2 eV in binding energy.[217] In principle, extra information as to the Cu oxidation state can be obtained from the Auger lines in the survey scan but this proved not possible for our samples due to the relatively low concentration of Cu in the WO_{3-x} layer. When the Cu | WO_{3-x} films are brought into air, the non-stoichiometric WO_{3-x} present is oxidised to WO_3, as evident from the lack of oxygen deficient species in the 24hr oxidised sample (Table 4.2 and Figure 4.9). There is virtually no reaction with the copper in the sample, showing that the oxygen deficient tungsten species oxidises preferentially to copper. This is to be expected when considering the enthalpies of formation of copper and tungsten oxides, which are -157.3 kJ mol^{-1}, -589.7 kJ mol^{-1} and -

842.9 kJ mol^{-1} for CuO, WO_2 and WO_3 respectively.[218] Based upon the enthalpies of formation, when molecular oxygen arrives at the surface, it is more thermodynamically favourable for it to react with WO_{3-x}, rather than Cu.

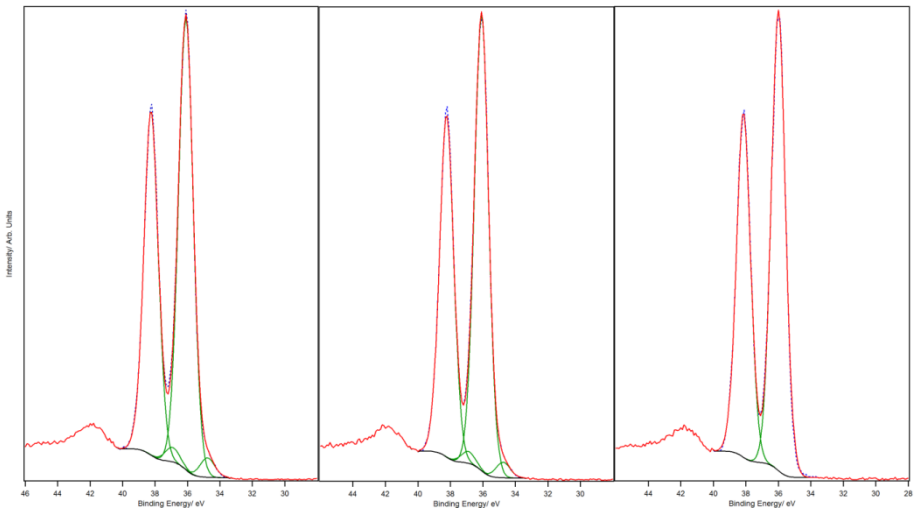

Figure 4.9: W4*f* XPS spectra of the Cu 8 nm | WO_{3-x} 20 nm films with various air exposure times, 0 hr, 1 hr and 24hrs from left to right. Raw data, fitted peaks, total fit and background are coloured red, green, dotted blue and black respectively.

As oxidation proceeds, more copper is brought into the WO_3, but the binding energy of the peak associated with copper remains constant (Figure 4.8), showing that very little oxidation of the metallic copper has taken place (Table 4.2).

Rationalizing the improvement in far-field transparency in Figure 4.3 in terms of Cu doping of the WO_{3-x} over layer is less intuitive since the electrons responsible for the increase in conductivity might also be expected to increase reflection. However, delocalized electrons are required for reflection of light, and it is known that the disorder imparted by the process of thermal evaporation and prevalence of oxygen array vacancies in WO_{3-x} serves to localize charge carriers.[216] Consequently the electrons provided by the

Cu would be expected to increase the refractive index, due to the increase in electronic polarisability of the ions, rather than increase reflectivity. The measured increase in transparency can therefore be attributed to a reduction in reflectivity due to the increased refractive index of the WO_{3-x} layer upon doping. Simulations predict that an increase in refractive index of ~0.7, for wavelengths greater than 600 nm, would give rise to the measured far-field transparency (Figure 4.10). There is evidence that the presence of tungsten in the lower oxidation state, (either due to oxygen deficiency or intercalated cations) increases the refractive index at longer wavelength,[112, 216] and modifies the work function by modifying the chemical potential.[102,224]

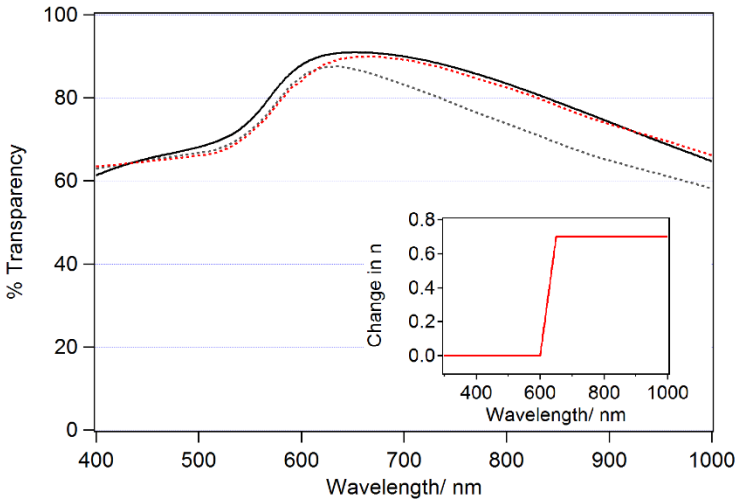

Figure 4.10: Experimental (solid black) and simulated (dotted grey and red) transparency spectra of Cu 8 nm | WO_{3-x} 20 nm films. The dotted grey curve shows the simulated transparency using literature values for the refractive index (n) and extinction coefficient. The dotted red curve shows the simulated transparency with n increased by 0.7 for $\lambda >$ 600 nm, as shown in the inset.

It was not possible to make a reliable measurement of the refractive index of the doped 20 nm WO_{3-x} film on Cu using ellipsometry, due to the very low oxide thickness.

However, the large reduction in reflectivity has been confirmed using spectroscopic reflectivity measurements (Figure 4.11). The reduction in reflectivity is qualitatively consistent with the increase in transparency and, importantly for PV applications this reduction in reflectivity persists for off-normal angles.

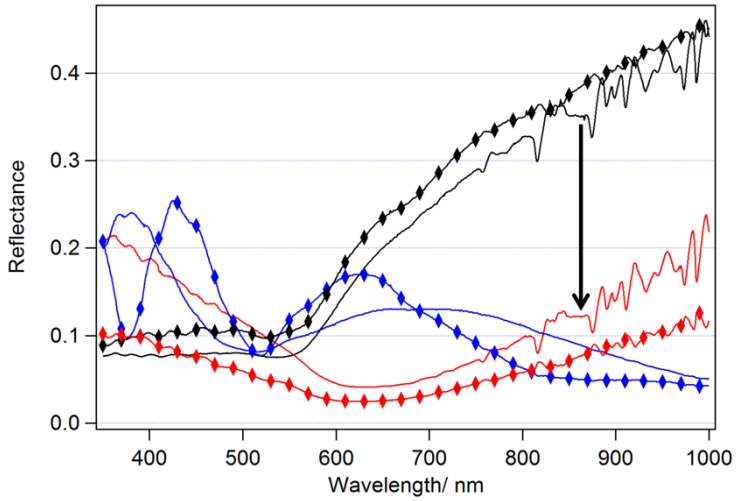

Figure 4.11: Reflectivity spectra of Cu 8 nm (black), Cu 8 nm | WO_{3-x} 20 nm (red) and ITO (blue) films. The angle of incidence is 36.5° for lines with markers, and 10.5° for lines without. The light was incident from the glass side as is the case in an OPV device.

The transparency spectrum of the Cu | WO_{3-x} window electrode is well matched to the current and emerging generation of OPVs, which rely on the high photon flux in the red and near infra-red part of the solar spectrum to achieve high photocurrent. The very low surface roughness (~0.7 nm) is also well matched to OPVs, helping to minimize the likelihood of parasitic current shunting across the thin light harvesting organic semiconductor layers used in the most efficient OPV device architectures. Vasilopoulou *et al.* have reported the use of a very thin (~ 5 nm) film of reduced tungsten oxide ($WO_{2.5}$) as an electron injection layer in organic light emitting diodes,[207] but to my knowledge WO_3 has exclusively been used as a hole-extracting layer in OPVs due to its

high work function, and the layer thickness is limited to ≤10 nm by its low conductivity.[222,225-227] In view of the evidence for the *n*-type character of the Cu doped WO_{3-x} and the relatively low work function of the Cu | WO_{3-x} electrode the possibility that this electrode might be well suited as the *electron extracting layer* in inverted OPVs was investigated. A model OPV based on the efficient BHJ PTB7/$PC_{70}BM$ was used, along with a film thickness that has been shown to result in optimal performance in inverted OPVs.[35] To ensure good alignment between the lowest unoccupied molecular orbital (LUMO) of the electron acceptor ($PC_{70}BM$ LUMO 3.7 eV below the vacuum level)[196] and the E_f of the window electrode a ~1 nm Al layer was deposited onto the electrode immediately prior to device fabrication. Importantly this additional layer reduces the work function of the Cu | WO_{3-x} electrode and reference ITO | WO_{3-x} electrode to almost exactly the same value; 3.67 ± 0.01 eV and 3.71 ± 0.02 eV respectively after 15 hours storage in a vacuum (Table 4.3), which ensures comparable interfacial energetics with the PTB7/$PC_{70}BM$ layer.

Substrate	Conditions	Work Function/ eV
Cu 8 nm | WO_{3-x} 10 nm | Al 1.2 nm	Fresh	3.66 ± 0.05
	After 15hrs in Vacuum	3.67 ± 0.01
Cu 8 nm | WO_{3-x} 20 nm | Al 1.2 nm	Fresh	3.33 ± 0.11
	After 15hrs in Vacuum	3.69 ± 0.08
ITO | WO_{3-x} 10 nm | Al 1.2 nm	Fresh	3.63 ± 0.17
	After 15hrs in Vacuum	3.71 ± 0.02

Table 4.3: Work function values of WO_{3-x} based electrodes.

These work function measurements were made using a Kelvin probe located in the same glove box as the thermal evaporator and spin coater used for device fabrication (Section 2.33). The work function after this period of storage under vacuum is the value that is relevant for device studies, since spin coating of the polymer layer is carried out the day after electrode fabrication in our laboratory. This time also ensures doping of the WO_{3-x} layer by Cu is complete (Figure 4.7). These two identical work functions within error show that the electrodes have the same work function when put into the device, showing that any changes in V_{oc} cannot be attributed to a difference in work function, and that the deposition of this Al layer can be carried out at different thicknesses yielding the same result. The fresh Cu 8 nm | WO_{3-x} 20 nm | Al 1.2 nm result can be explained by the fact that aluminium films with surface oxidation have a work function of ≈3.4 eV, whereas the Cu doped films have a work function of ≈3.7 eV.[203]

Furthermore, the sheet resistance and transparency of the Cu | WO_{3-x} electrode does not significantly change upon annealing at 200°C for 10 minutes under nitrogen (Figures 4.12 and 4.13), the highest temperature used for annealing solution processed BHJ layers for OPVs.[228] The Cu | WO_{3-x} electrode's thermal stability was tested by heating a Cu 8 nm | WO_{3-x} 20 nm | Al 0.8 nm film under nitrogen and recording the resulting sheet resistance (Figure 4.12).

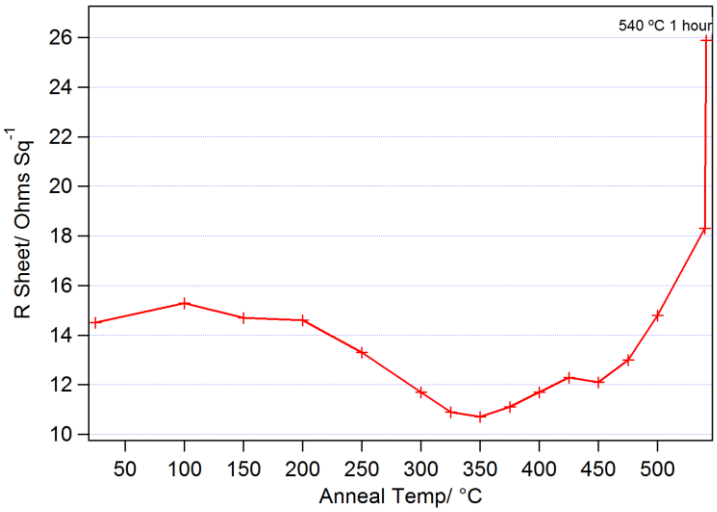

Figure 4.12: Sheet resistance of a Glass | SAM | Cu 8 nm | WO_{3-x} 20 nm | Al 0.8 nm film after heating successively at varying temperatures under nitrogen. All heating was carried out for 10 minutes, with the exception of the final point which was for one hour.

Figure 4.12 shows that these Cu | WO_{3-x} films are exceptionally thermally stable, with comparable sheet resistance values upon heating even at temperatures as high as 500 °C, with the sheet resistance values of 14.5 and 14.8 Ω sq^{-1} for unheated and heated at 500 °C for 10 minutes respectively. The sheet resistance actually falls for temperatures below 500 °C, in keeping with previous reports in the literature for thin copper films.[131] The far-field transparency of these Cu | WO_{3-x} | Al films was also probed as a function of annealing temperature, and the results are shown in Figure 4.13.

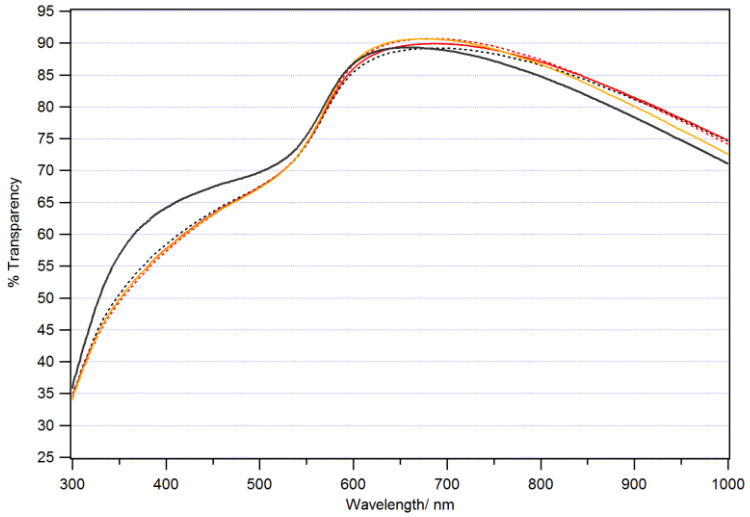

Figure 4.13: Transparency spectra of Glass | SAM | Cu 8 nm | WO_{3-x} 20 nm | Al 0.8 nm films after annealing at varying temperatures. Non-annealed, annealed at 100, 150 and 200 °C are coloured in black, dotted black, red, dotted red and yellow respectively. All annealing was carried for 10 minutes.

Figure 4.13 shows that annealing these electrodes at temperatures up to 200 °C has little effect on their transparency, with maximum deviations from the non-annealed sample of ~5%. This is crucial for screening OPV device materials, as the processes involved in OPV manufacture often contain annealing steps, and when PV modules are in use the temperatures of devices can increase significantly.

Representive *JV* characteristics for OPVs fabricated on Cu | WO_{3-x} | Al and ITO | WO_{3-x} | Al electrodes under one sun simulated solar illumination and in the dark are given in Figure 4.14 and the full data set is given in Table 4.4.

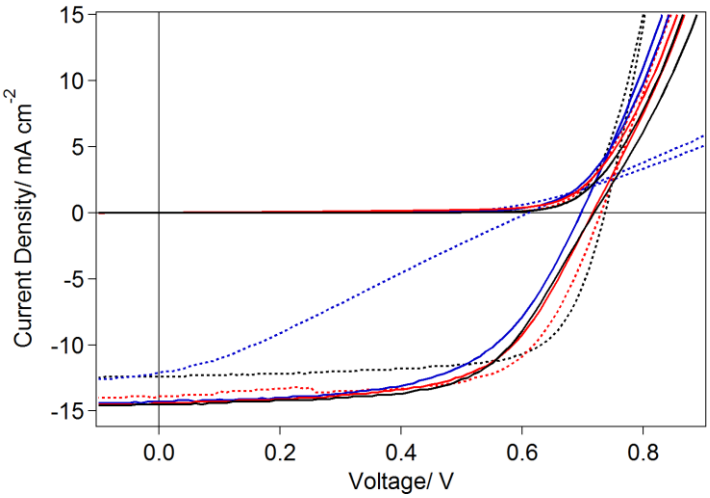

Figure 4.14: Champion OPV devices with ITO and Cu electrodes, with 5, 10 and 20 nm WO_{3-x}. ITO with 5, 10 and 20 nm of WO_{3-x} and Cu with 5, 10 and 20 nm of WO_{3-x} are coloured dashed black, dashed red, dashed blue, solid black, solid red and solid blue respectively. Device architectures: Glass | SAM | Cu 8 nm | WO_{3-x} (5, 10 or 20 nm) | Al 1.2 nm | PTB7/$PC_{70}BM$ | MoO_3 5 nm | Al and Glass | ITO | WO_{3-x} (5, 10 or 20 nm) | Al 1.2 nm | PTB7/$PC_{70}BM$ | MoO_3 5 nm | Al.

Window electrode	J_{sc}/ **mA cm^{-2}**	V_{oc}/ **V**	***FF***	***PCE*/ %**
ITO | WO_{3-x} 5 nm	12.6 ± 0.9, 14.2 (Best)	0.66 ± 0.08, 0.737 (Best)	0.6 ± 0.1, 0.702 (Best)	5 ± 1, 6.42 (Best)
ITO | WO_{3-x} 10 nm	13 ± 1, 14.9	0.69 ± 0.03, 0.730	0.60 ± 0.06, 0.659	5.2 ± 0.9, 6.70
ITO | WO_{3-x} 20 nm	8 ± 3, 12.1	0.56 ± 0.08, 0.639	0.25 ± 0.04, 0.320	1.2 ± 0.6, 2.06
Cu | WO_{3-x} 5 nm	14.3 ± 0.4, 15.2	0.70 ± 0.03, 0.733	0.58 ± 0.03, 0.626	5.8 ± 0.5, 6.37
Cu | WO_{3-x} 10 nm	13.5 ± 0.9, 14.5	0.68 ± 0.04, 0.725	0.56 ± 0.04, 0.606	5.1 ± 0.7, 6.27
Cu | WO_{3-x} 20 nm	12.4 ± 0.8, 14.3	0.66 ± 0.03, 0.703	0.54 ± 0.03, 0.583	4.5 ± 0.6, 5.81

Table 4.4: *JV* data for the inverted devices shown in Figure 4.14. Device architectures: Glass | SAM | Cu 8 nm | WO_{3-x} (5, 10 or 20 nm) | Al 1.2 nm | PTB7/$PC_{70}BM$ | MoO_3 5 nm | Al and Glass | ITO | WO_{3-x} (5, 10 or 20 nm) | Al 1.2 nm | PTB7/$PC_{70}BM$ | MoO_3 5 nm | Al.

As expected, the ITO reference devices using a 20 nm WO_{3-x} layer (dashed blue line in Figure 4.14) have very low fill factors due to the high series resistance of the WO_{3-x} layer. This is manifested in a shallower gradient as the *JV* curve crosses the voltage axis. Conversely, the device based on a Cu electrode functions well for all WO_{3-x} thicknesses, consistent with the observation that the WO_{3-x} film is spontaneously doped by Cu, and this doping lowers the sheet resistance of the WO_{3-x} layer. This is in stark contrast to the ITO reference devices. Thus, the Cu doping of WO_{3-x} is needed for efficient electron extraction with a 20 nm WO_{3-x} film. It has been reported previously that the conductivity of WO_3 can be improved by doping with Cu,[32] so this conclusion does not seem unreasonable. Devices using Cu electrodes have a higher series resistance which is evident from the shallow gradient where the *JV* curve intersects the *x* axis. This cannot be due to a difference in conductivity since Cu doped WO_3 must be more conductive, and it is therefore attributed to a small field dependent barrier at the electron extracting/$PC_{70}BM$ interface, which results in increased recombination. Figure 4.15 shows the champion cells for the same structure as in Figure 4.14, but with 0.8 nm of Al to modify the WO_{3-x} electrode in place of 1.2 nm. There is an S shaped kink present, which is consistent with a buildup of charges and a loss of charge extraction near the open circuit condition. This may be caused by a mismatched work function of the

electrode. 1.2 nm of Al was subsequently used for all other devices, and the S shaped kink is not apparent.

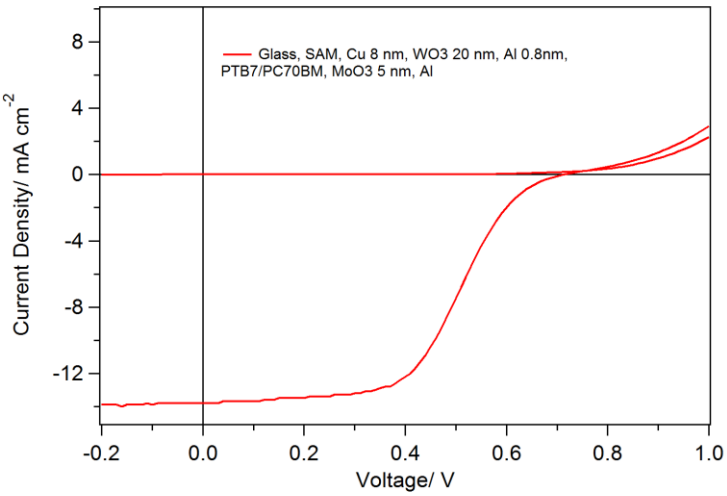

Figure 4.15: Champion OPVs with the structure: Glass | SAM | Cu 8 nm | WO_{3-x} 20 nm | Al 0.8 nm | PTB7/$PC_{70}BM$ | MoO_3 5 nm | Al.

It was necessary to explore three different thicknesses of WO_{3-x} to achieve optimal performance in the ITO reference device (Figure 4.14). Devices employing a Cu window electrode achieve slightly higher average photocurrents than the ITO reference OPVs and smaller variance of performance. The latter can be understood in terms of the higher degree of electrical homogeneity of the Cu | WO_{3-x} as compared to ITO | WO_{3-x} since the variability of the properties of ITO glass across on the 10-100 nm scale is well documented.[229] The far-field transparency of the Cu | WO_{3-x} electrode is however lower than that of ITO and so the fractionally higher J_{sc} cannot be rationalized in terms of more light entering the device through the window electrode. It can however be explained by light trapping in a resonant optical cavity, consistent with the sharp peak in the external quantum efficiency spectra between 600-700 nm (Figure 4.16). This conclusion is supported by the results of optical field intensity modeling, which shows strong

overlapping optical resonances at ~600 nm and ~750 nm using optical constants for PTB7/$PC_{70}BM$ layer taken from the literature[35] and optical constants for MoO_3 measured using spectroscopic ellipsometry. The n and k values of MoO_3 were measured using spectroscopic ellipsometry using a thick MoO_3 film deposited in our laboratory and were found to be in good agreement with the literature. Since photocurrent is directly proportional to the optical field intensity this gives rise to the dramatic increase in EQE in this wavelength range which compensates for the lower reduced light harvesting capability below ~ 500 nm.

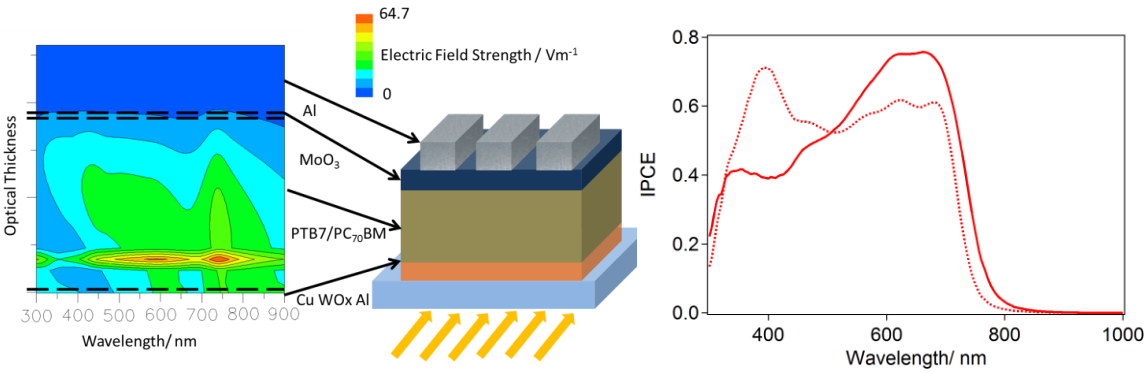

Figure 4.16: Left: Electrical field strength simulations for a Glass | Cu 8 nm | WO_{3-x} 5 nm | Al 1.2 nm | PTB7/$PC_{70}BM$ 90 nm | MoO_3 5 nm | Al 100 nm device. Right: EQE spectra for Glass | SAM | Cu 8 nm | WO_{3-x} 10 nm | Al 1.2 nm | PTB7/$PC_{70}BM$ | MoO_3 5 nm | Al (solid red) and Glass | ITO | WO_{3-x} 10 nm | Al 1.2 nm | PTB7/$PC_{70}BM$ | MoO_3 5 nm | Al (dashed red) OPVs.

The sensitivity of the transparency of Cu | WO_{3-x} electrodes to the extent of Cu diffusion into the WO_{3-x} over layer serves as an *in-situ* probe for its stability towards current density and electric field strength in a working OPV device. Model semi-transparent OPVs based on a pentacene/C_{60} heterojunction and a semi-transparent Ag

hole extracting electrode were fabricated using either ITO | WO_{3-x} or Cu | WO_{3-x} as the electron extracting electrode. This heterojunction was selected because it does not absorb significantly in the region where the Cu electrode is most transparent, and vacuum deposition of both materials ensures a very high degree of control over layer thickness. The transparency of each device was measured before and after 1 hour constant illumination at the maximum power point (Figure 4.17).

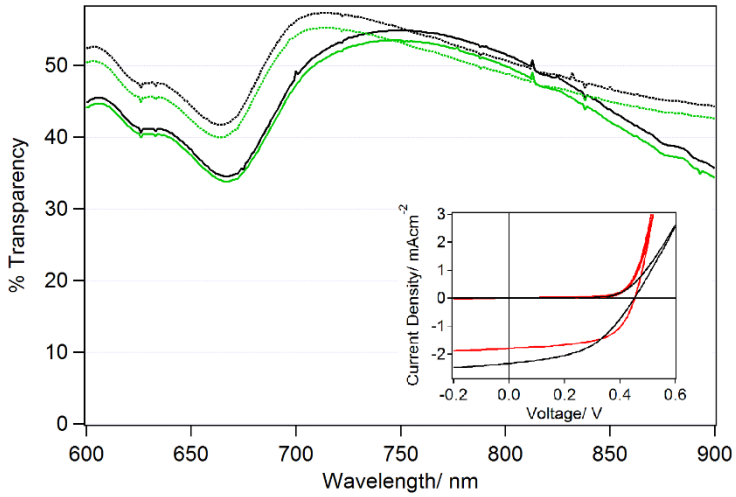

Figure 4.17: Transparency spectra of semi-transparent OPV devices using an ITO | WO_{3-x} (dashed lines) or Cu | WO_{3-x} (solid lines) electrode. The device structure is: Glass | Cu 8 nm or ITO 100 nm | WO_{3-x} 10 nm | Al 1.2 nm | C_{60} 40 nm | pentacene 46 nm | MoO_3 5 nm | Al 1 nm | Ag 12 nm | MoO_3 30 nm. Black curves correspond to device transparency before testing. Green curves correspond to device transparency after 1 hour at the maximum power under one sun simulated solar illumination. **Inset**: Typical current density- voltage curves for OPV devices using a Cu (red) or ITO (black) electrode. These semi-transparent devices had an active area of 0.4 cm^2.

In addition to the transparency spectra in Figure 4.17, the transparency of these semi-transparent devices was also recoded after 1 hour at the open circuit condition. As shown in Figure 4.18, the transparency for the Cu devices changes slightly less than that of the ITO devices.

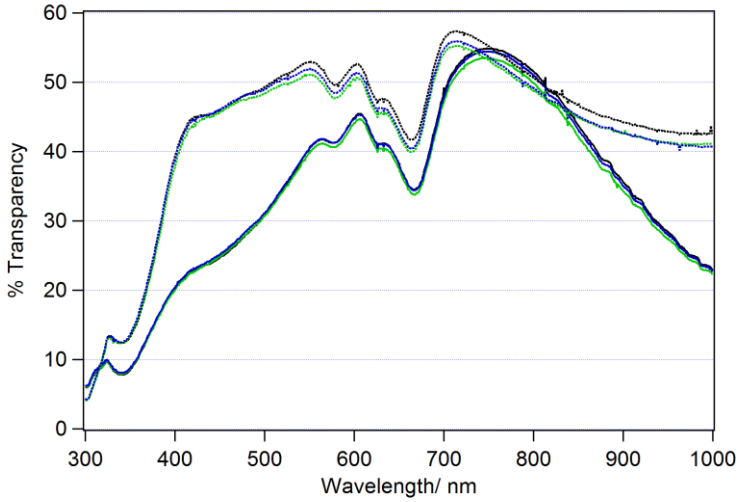

Figure 4.18: Transparency spectra of semi-transparent OPV devices using an ITO |WO_{3-x} (dashed lines) or Cu | WO_{3-x} (solid lines) electrode. The device structure is: Glass | Cu 8 nm or ITO 100 nm | WO_{3-x} 10 nm | Al 1.2 nm | C_{60} 40 nm | pentacene 46 nm | MoO_3 5 nm | Al 1 nm | Ag 12 nm | MoO_3 30 nm. Black curves correspond to device transparency before testing. Green curves correspond to device transparency after 1 hour at the maximum power under one sun simulated solar illumination. Blue curves correspond to OPVs after 1 hour at the open circuit condition under one sun simulated solar illumination.

The pentacene OPV devices fabricated for transparency measurements had an active area of ~0.4 cm^2. In both the conventional and inverted pentacene devices, devices fabricated on Cu electrodes have higher fill factors that their ITO based equivalents. This

decrease in *FF* observed for ITO devices shows that the sheet resistance is an important factor, as explained previously (Section 1.9). The transparency in both sets of devices dropped by the same amount (~2%) across the wavelength 600-900 nm (Figure 4.17), indicating that this change is not due to a change in the transparency of the Cu | WO_{3-x} electrode, but to another part of the OPV device that is common to all devices. The Cu | WO_{3-x} electrode also functions efficiently in conventional devices, as shown in Figures 4.19, 4.20 and Table 4.5.

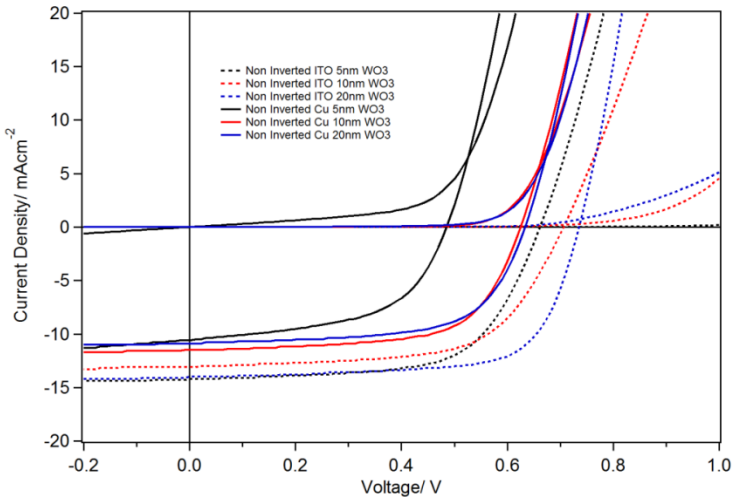

Figure 4.19: Champion devices for ITO and Cu conventional structures, with 5, 10 and 20 nm of WO_{3-x}. Full device structures were: Glass | SAM | Cu 8 nm | WO_{3-x} (5, 10 or 20 nm) | PTB7/PC_{70}BM | BCP 8 nm | Al 90 nm or Glass | ITO | WO_{3-x} (5, 10 or 20 nm) | PTB7/PC_{70}BM | BCP 8 nm | Al 90 nm.

	J_{sc}/ mA cm^{-2}	V_{oc}/ V	*FF*	*PCE*/ %
ITO | WO_{3-x} 5 nm	11 ± 1, 14.2	0.660 ± 0.009, 0.672	0.63 ± 0.02, 0.661	4.7 ± 0.5, 6.01
ITO | WO_{3-x} 10 nm	11.3 ± 0.9, 13.1	0.68 ± 0.02, 0.713	0.61 ± 0.03, 0.646	4.8 ± 0.6, 5.77
ITO | WO_{3-x} 20 nm	11 ± 1, 14.0	0.72 ± 0.01, 0.735	0.67 ± 0.08, 0.700	5.4 ± 0.8, 7.23
Cu | WO_{3-x} 5 nm	10.1 ± 0.6, 11.1	0.45 ± 0.03, 0.485	0.588 ± 0.02, 0.615	2.7 ± 0.1, 2.80
Cu | WO_{3-x} 10 nm	10.8 ± 0.5, 11.7	0.56 ± 0.04, 0.625	0.60 ± 0.07, 0.644	3.6 ± 0.5, 4.65
Cu | WO_{3-x} 20 nm	10.7 ± 0.2, 10.9	0.62 ± 0.01, 0.642	0.60 ± 0.04, 0.640	4.0 ± 0.4, 4.41

Table 4.5: *JV* characteristics of Cu and ITO based PTB7/$PC_{70}BM$ OPV cells; each column contains the mean with standard deviation followed by the champion value. Full device structures were: Glass | SAM | Cu 8 nm | WO_{3-x} (5, 10 or 20 nm) | PTB7/$PC_{70}BM$ | BCP 8 nm | Al 90 nm or Glass | ITO | WO_{3-x} 5, 10 or 20 nm | PTB7/$PC_{70}BM$ | BCP 8 nm | Al 90 nm.

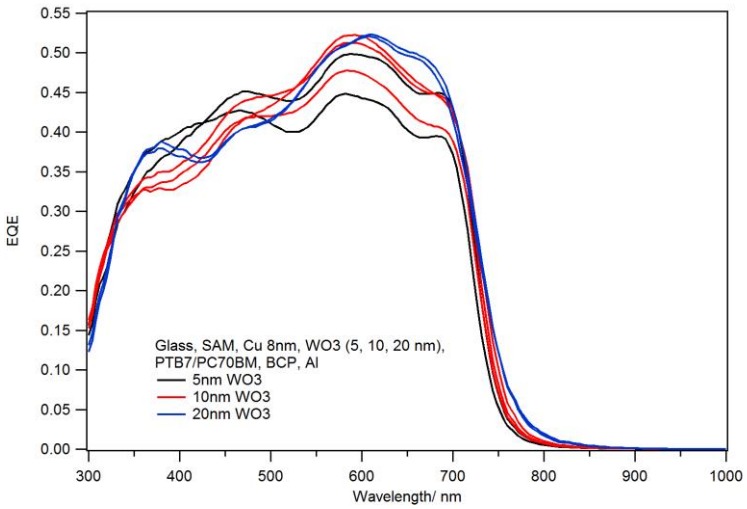

Figure 4.20: EQE spectra for conventional devices fabricated on Cu electrodes, with 5, 10 and 20 nm WOx. The full structure is Glass | SAM | Cu 8 nm | WO_{3-x} (5, 10 or 20 nm) | PTB7/$PC_{70}BM$ | BCP | Al.

In-contra to the inverted 20 nm ITO devices shown in Figure 4.14, the conventional devices fabricated on ITO | WO_{3-x} 20 nm electrodes function efficiently. This shows that doping of the WO_{3-x} layer is required for electron extraction, but not for hole extraction. Figure 4.19 and Table 4.5 show that 5 nm of WO_{3-x} is not thick enough to yield the maximum V_{oc} in conventional devices, based on either ITO or Cu electrodes. This data suggests that V_{oc} is not just a function of work function for oxide buffer layers, it is also function of the degree of interfacial alignment. To investigate this, the work function of WO_{3-x} of differing thicknesses was recorded on ITO glass, and the results are presented in Table 4.6. The increased series resistance must be due to a small barrier to electron extraction at the organic/WO_{3-x} interface as the resistance of the oxide is much lower than transport through the organic.[230]

Substrate	Fresh Work Function/ eV	Work Function After Vacuum Overnight/ eV
ITO | WO_{3-x} 5 nm	5.7 ± 0.1	5.02 ± 0.02
ITO | WO_{3-x} 10 nm	5.3 ± 0.1	4.87 ± 0.01
ITO | WO_{3-x} 20 nm	5.40 ± 0.03	4.89 ± 0.02

Table 4.6: Work function values for ITO | WO_{3-x} electrodes, work function values were recorded immediately after deposition, and after being left in the vacuum chamber overnight.

Table 4.6 shows that the 10 and 20 nm WO_{3-x} samples plateau to the same value of ~4.9 eV after storage under vacuum overnight. It is this value that is important, as this is the electrode used in device fabrication; device fabrication was carried the day

after electrode fabrication. Given that the ionisation potential of PTB7 is ~5.15 eV,[35,60] these three work function values are all suitable for the extraction of holes in this device, and the reduction in V_{oc} with decreasing thickness cannot therefore be explained in light of these results. However, these results are recorded using the Kelvin Probe technique, which records the average work function, so there is a possibility that there is a lack of homogeneity or dead spots on the surface of the 5 nm device, reducing the V_{oc} but not greatly affecting the recorded work function.

Figure 4.7 shows that the Cu | WO_{3-x} window electrode has a stable sheet resistance in a nitrogen filled glovebox, but the stability of the electrode in air is also of importance. Figure 4.21 shows the sheet resistance of a Cu | WO_{3-x} film in laboratory air.

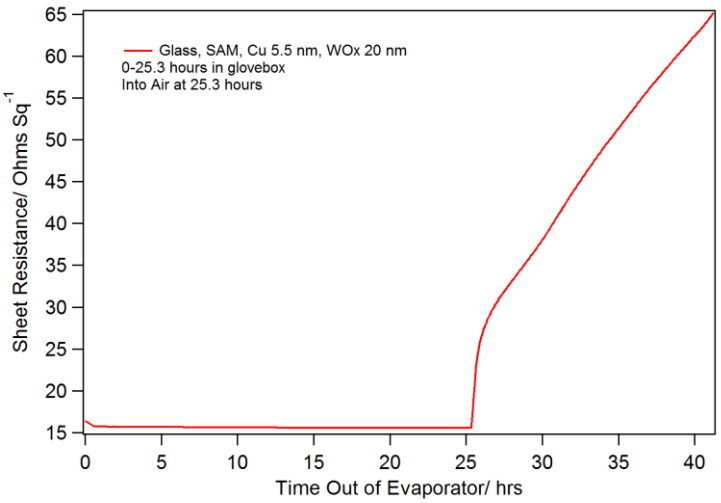

Figure 4.21: Sheet resistance as a function of time in air for a Cu 5.5 nm | WO_{3-x} 20 nm film on glass with a mixed SAM.

Figure 4.21 shows that the Cu | WO_{3-x} film's sheet resistance rises sharply when brought into air (at 25.3 hours) and does not saturate in ~ 20 hours. It also shows that the sheet resistance values rise to values higher than are viable for large scale OPVs, illustrating a disadvantage of this electrode system.

4.5 Conclusions

In summary, a novel window electrode for OPVs has been presented based on an ultra-thin bilayer of Cu and tungsten sub-oxide. This electrode is fabricated by simple sequential deposition of these low cost and abundant materials. This electrode derives its exceptional optical and electrical properties from spontaneous solid state diffusion of Cu into the adjacent WO_{3-x} layer at room temperature. This diffusion imparts excellent far-field transparency over a broad range of wavelengths matched to the solar spectrum, and over a range of angles of incidence and renders the oxide layer highly electrically conductive towards the transport of electrons. It has been demonstrated that this unpatterned Cu electrode can perform as well as ITO glass in ~6% efficient inverted OPVs by trapping light in a resonant optical cavity. To my knowledge this is the first time an unpatterned Cu electrode has been shown to perform as well as ITO glass in an OPV. In addition to the materials cost advantage associated with the use of Cu instead of Ag this electrode also offers the advantages of: (i) a sheet resistance nearly half that of any unpatterned Cu film electrode reported to date, at 6-7 Ω sq^{-1}.; (ii) a simplified architecture as compared to triple layer Ag electrodes.; (iii) and, unlike optically thin Ag electrodes, the transparency maxima is well-matched to the peak of the solar photon flux, and thus to the emerging generation of narrow band gap polymers[35] and non-fullerene electron acceptors.[231,232] The lack of air stability is however a disadvantage, and an issue that would need to be solved prior to use outside a research laboratory environment.

Chapter 5 – Achieving Stability and Transparency in Cu Window Electrodes

5.1 Abstract

In Chapter 3 it was shown that optically thin Cu films can be passivated towards oxidation in air using an ultra-thin Al layer. In Chapter 4 it was shown that the transparency of Cu window electrodes can be increased to a level comparable to that of ITO glass, across most of the spectrum over which state-of-the-art thin film PV harvest light, using a layer of the low cost, wide band gap sub-oxide WO_{3-x} which is spontaneously doped with Cu from the underlying Cu film. The first part of this chapter describes an attempt to combine these approaches to achieve both high transparency and high stability. The second part explores a different approach to achieving this objective based on the use of a Cu | Ag bilayer.

5.2 Background

As shown in Chapter 3, sub-9 nm, Cu films can be fabricated on glass substrates using a molecular adhesive layer and passivated toward oxidation in air by deposition of a 0.8 nm Al overlayer which forms an ultra-thin self-limiting $CuAlO_x$ oxide upon exposure to air.[203] Crucially this oxide layer[177] is so thin that it does not impede charge transport from the semiconductor into the electrode. The only serious disadvantage of this electrode is its low transparency as compared to commercial conducting oxide coated glass; approximately 30% lower across the visible spectrum.[203]

Chapter 4 describes an approach to address the problem of low transparency based on using a sub stoichiometric WO_{3-x} overlayer that is spontaneously *n*-doped at

room temperature by Cu atoms diffusing up from the underlying electrode. This high refractive index overlayer dramatically improves the transparency of ultra-thin Cu electrodes. Unfortunately, these electrodes are not air stable, which is a property that is required for long life applications of this electrode including use as the window electrode in OPVs. This chapter describes two approaches to realise Cu electrodes with both stability towards oxidation in air and high far-field transparency, the first of which involves integration of the two approaches developed in Chapters 3 and 4 of this thesis. The second approach exploits the greater resistance of Ag to oxidation in air than Cu, although the use of Ag inevitably increases the materials cost since Ag is 100 times more expensive that Cu.[84] Where these electrodes do not have Cu dopants in the WO_{3-x} layer, this could affect the device characteristics, so the layer thickness may need to be altered, or OPVs may need to be fabricated in the standard architecture.

5.3 Experimental

Cu and WO_{3-x} films were prepared on glass substrates as described in Chapter 4. Model OPVs were fabricated as described in Chapter 2. Cu | Ag bilayers were evaporated without breaking vacuum. All oxidation of electrodes prior to subsequent layer deposition was carried out in dry air (1 bar, <0.015 vol% H_20) in the dark. All oxidation of films for sheet resistance measurements were carried out using laboratory air with ambient indoor light.

5.4 Results and Discussion

In the first instance experiments were undertaken to passivate the Cu | WO_{3-x} films towards oxidation in air using an ultra-thin Al layer on top of the Cu film. The Al was deposited immediately after Cu deposition and the electrode was exposed to the glove box environment (≤5 ppm O_2) for 10 minutes whilst the WO_{3-x} deposition boat was

loaded into the vacuum chamber. Due to the very high reactivity of Al a very thin (< 0.8 nm) oxide layer will most likely have formed at the electrode surface during this brief period even though the oxygen levels in the glove box are ≤5 ppm. Figure 5.1 shows the sheet resistance of a Cu | Al | WO_{3-x} | film as a function of time immediately after WO_{3-x} deposition. For the first 23 hours the electrode was in the glove box environment, after which it was bought into the laboratory for oxidation.

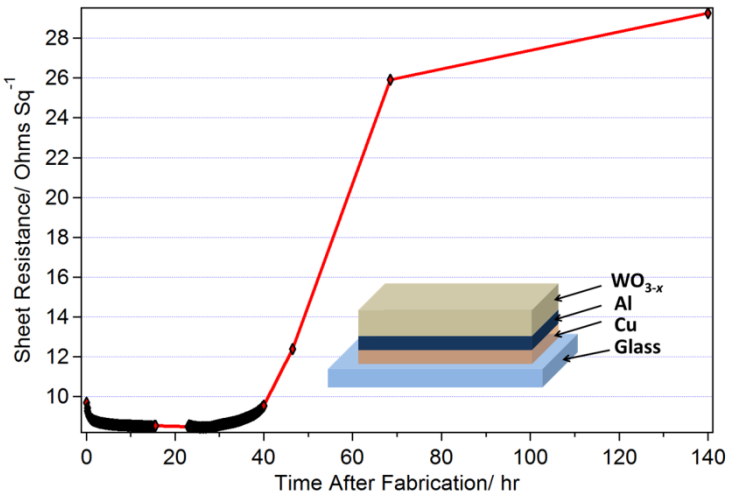

Figure 5.1: Sheet resistance as a function of time in air for a Cu 8 nm | Al 0.8 nm | WO_{3-x} 20 nm film on glass with a mixed SAM.

Figure 5.1 shows a small initial decrease in the sheet resistance of the electrode under nitrogen, as seen previously for Cu | Al films. It also shows that the Al layer between the Cu and WO_{3-x} layers does not completely passivate the electrode since the sheet resistance increases gradually at first and much more rapidly increases once the electrode is brought into air. This result is surprising since in Chapter 3 a 0.8 nm Al layer has been shown to passivate Cu electrodes towards air oxidation without a WO_{3-x} layer. A plausible reason for this is that the partially oxidised Al layer is disrupted (i.e. made discontinuous) by the incoming WO_{3-x} which is sub-stoichiometric and therefore reactive.

As explained in Chapter 4 a great deal of energy is needed to evaporate WO_{3-x} such that the whole vacuum chamber heats to ~ 50 °C during WO_{3-x} layer deposition.

In an attempt to overcome this issue, a Cu | Al film was oxidised in dry air for 1 hour prior to WO_{3-x} deposition to form a protective oxide cap at the electrode surface. The evolution of the sheet resistance recorded in a nitrogen filled glove box and in laboratory air as before is shown in Figure 5.2.

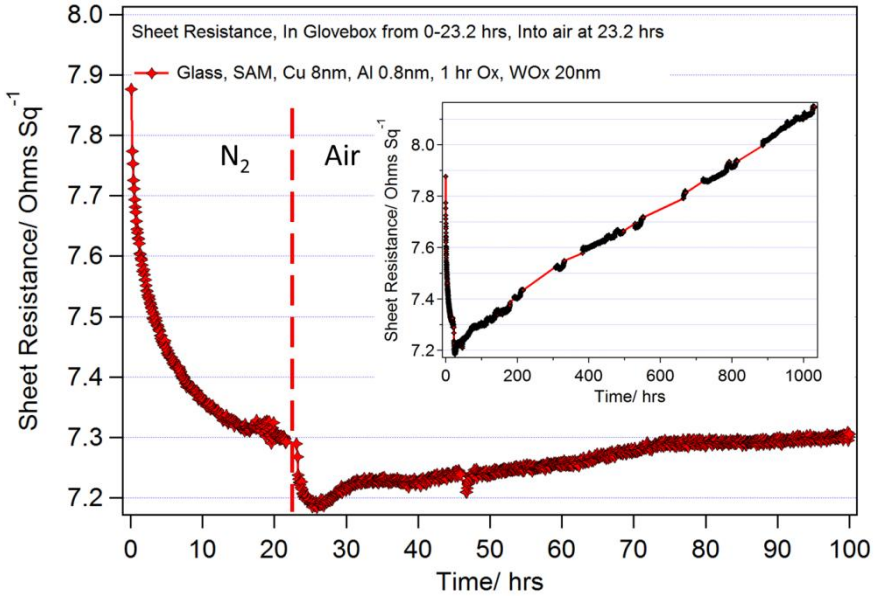

Figure 5.2: Sheet resistance as a function of time in air for a Cu 8 nm | Al 0.8 nm | 1 hr Ox | WO_{3-x} 20 nm film on glass with a mixed SAM. Inset: Sheet resistance for the same film over a longer time scale in air.

Figure 5.2 shows that oxidising the Cu | Al electrode for 1 hour prior to WO_{3-x} deposition dramatically improves the stability of the triple layer electrode since the film sheet resistance remains below 8.2 Ω sq^{-1} for 1000 hours in laboratory air. This approach to passivating the electrode does however also block the diffusion of Cu into the WO_{3-x} layer, which is needed to improve the optical and electrical properties of that layer as

described in Chapter 4. Evidence for this is provided by the XPS spectra in Figure 5.3 for Cu | WO_{3-x}, Cu | Al | WO_{3-x} , and Cu | Al | 1 hour Oxidation | WO_{3-x} samples. Since the escape depth for ~95% of the photoelectrons generated by the incident X-rays is estimated to be <7 nm and XPS is sensitive to elemental composition to a level of ~ 0.1% it is clear that even without oxidation of the Cu | Al electrode prior to WO_{3-x} deposition Cu diffusion into the WO_{3-x} is blocked by the ultra-thin Al interlayer.

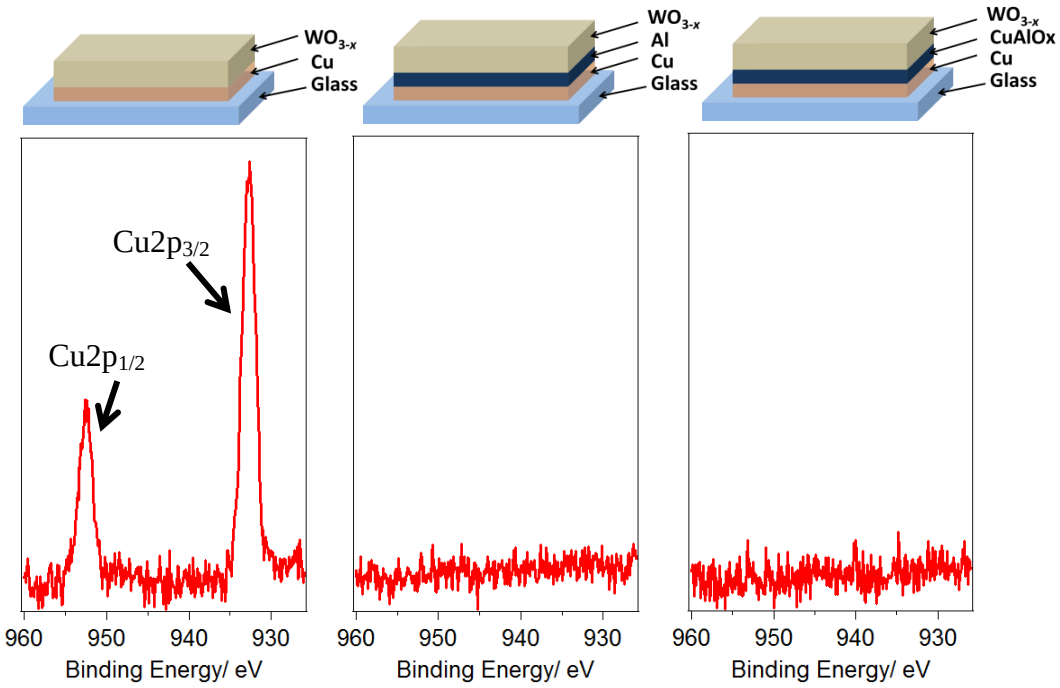

Figure 5.3: Cu2*p* XPS spectra of Cu 8 nm | WO_{3-x} 24 nm, Cu 8 nm | Al 0.8 nm | WO_{3-x} 24 nm, and Cu 8 nm | Al 0.8 nm | 1 hour Oxidation | WO_{3-x} 24 nm films from left to right. A schematic illustrating film the structure in each case is shown above the spectra. The substrates were stored under vacuum for 4 days before measurement to ensure diffusion of Cu into the WO_{3-x} layer has sufficient time to occur. Notably, the samples for XPS were briefly exposed to the laboratory environment prior to loading into the ultra-high vacuum system.

Figure 5.3 shows that prevention of diffusion of Cu into the WO_{3-x} overlayer is achieved with the Al interlayer, regardless of whether or not this interlayer is intentionally oxidised, as there is no evidence for Cu in the WO_{3-x} spectra.

To investigate the utility of the electrode in OPVs, devices were fabricated using the Cu | Al | 1 hr Ox | WO_{3-x} | 1.5hr Ox electrode and the PTB7/PC_{70}BM BHJ system. The second oxidation step was found to improve the transparency of the electrode. The champion device *JV* characteristics are shown in Figure 5.4, and the full data set is given in Table 5.1. The EQE spectra of a number of the Cu | WO_{3-x} 10 nm and ITO | WO_{3-x} 10nm devices given in Figure 5.5.

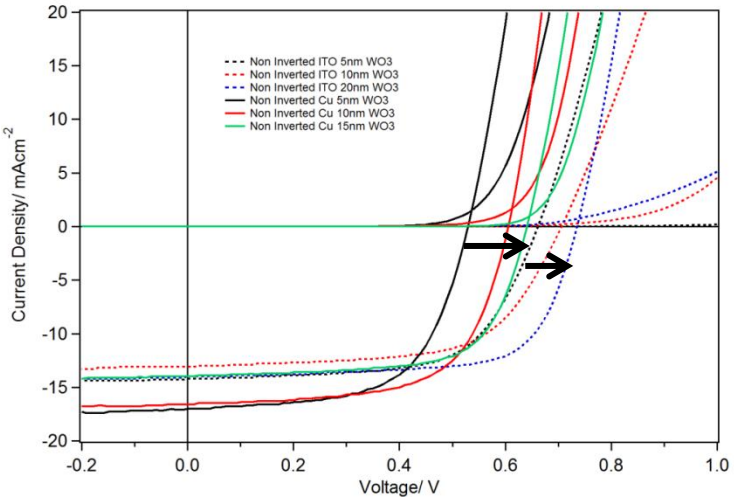

Figure 5.4: Champion OPV devices with ITO and Cu electrodes with 5, 10 and 15 or 20 nm of WO_{3-x}. The Cu devices are fabricated on Cu | Al (1hr Ox) | WO_{3-x} (1.5hr Ox) electrodes, with device structures as follows: Glass | SAM | Cu 8 nm | Al 0.8 nm | (1hr Ox) | WO_{3-x} | (1.5 hrs Ox) | PTB7/PC_{70}BM | BCP 8 nm | Al and | ITO | WO_{3-x} | PTB7/PC_{70}BM | BCP 8 nm | Al.

	J_{sc}/ mA cm^{-2}	V_{oc}/ V	*FF*	*PCE*/ %
ITO | WO_{3-x} 5 nm	14.2, 11.3 ± 1.1	0.672, 0.660 ± 0.009	0.661, 0.634 ± 0.02	6.01, 4.7 ± 0.5
ITO | WO_{3-x} 10 nm	13.1, 11.3 ± 0.9	0.713, 0.68 ± 0.02	0.646, 0.612 ± 0.03	5.77, 4.8 ± 0.6
ITO | WO_{3-x} 20 nm	14.0, 11.4 ± 1.3	0.735, 0.72 ± 0.01	0.700, 0.670 ± 0.08	7.23, 5.4 ± 0.8
Cu | Al | WO_{3-x} 5 nm	17.0, 14 ± 1	0.582, 0.53 ± 0.03	0.638, 0.61 ± 0.03	5.94, 4.6 ± 0.7
Cu | Al | WO_{3-x} 10 nm	17.2, 16 ± 1	0.656, 0.60 ± 0.02	0.698, 0.62 ± 0.04	6.4, 5.7 ± 0.5
Cu | Al | WO_{3-x} 15 nm	15.2, 13.9 ± 0.5	0.656, 0.63 ± 0.01	0.689, 0.63 ± 0.04	6.06, 5.5 ± 0.4

Table 5.1: *JV* characteristics of oxidised Cu | Al and ITO based PTB7/$PC_{70}BM$ OPV cells shown in Figure 5.4; each column contains the champion value followed by the mean with standard deviation.

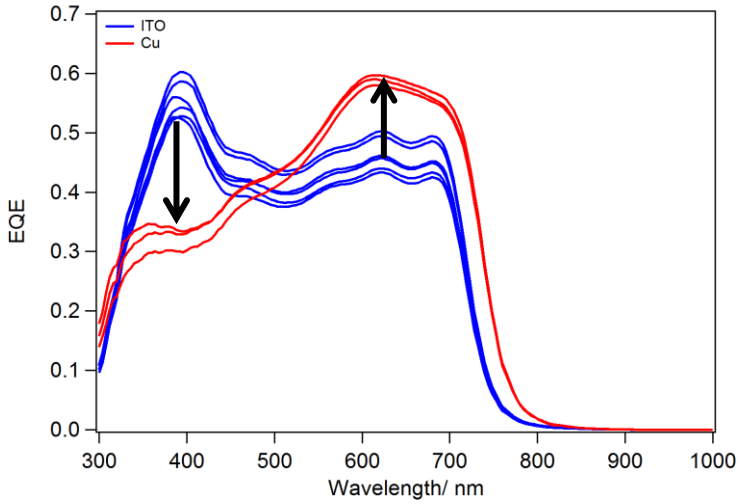

Figure 5.5: EQE spectra for ITO and Cu conventional structure OPVs with 10 nm WO_{3-x}, coloured blue and red respectively. The device structures as follows: Glass | SAM | Cu 8 nm | Al 0.8 nm | 1hr Ox | WO_{3-x} 10 nm | 1.5 hrs Ox | PTB7/$PC_{70}BM$ | BCP 8 nm | Al for

Cu devices and Glass | ITO | WO_{3-x} 10 nm | PTB7/$PC_{70}BM$ | BCP 8 nm | Al for the ITO devices.

The OPV devices fabricated on oxidised Cu | Al | WO_{3-x} electrodes have comparable *PCE* values to the ITO reference devices, with the former having a higher J_{sc} and a lower V_{oc}. The difference in J_{sc} cannot be explained in terms of a difference in electrode transparency. However, the improvement in J_{sc} is strongly dependent on device thickness and so most likely results from microcavity light trapping. This conclusion is supported by the EQE spectra in Figure 5.5, with a large enhancement of EQE in the high wavelength region.

It is evident from Table 5.1 that the V_{oc} increases with increasing WO_{3-x} thickness and the V_{oc} in devices using a Cu | Al | WO_{3-x} electrode is always significantly lower than that of devices using ITO | $WO_{3-x.}$ The thickness dependence of the V_{oc} cannot be explained with reference to incomplete WO_{3-x} coverage since it is known transition metal oxides form continuous films below 5 nm.[113] The dependence of V_{oc} with WO_{3-x} thickness may relate to the thickness of the space charge region formed at the metal-WO_{3-x} interface as there may be barrier to extraction if the electrode and WO_{3-x} have not established thermodynamic equilibrium. The change in V_{oc} may also result from a reduction in the work function of the Cu | Al | WO_{3-x} electrode during the final oxidation step, since the ionisation potential of PTB7 is ~5.2 eV[35,233] and the work function of WO_{3-x} has been shown to reduce with oxidation (Table 4.1).

The stability of OPV devices fabricated on these triple layer electrodes was assessed by measuring the current-voltage characteristic as a function of time under constant illumination (Figures 5.6 and 5.7).

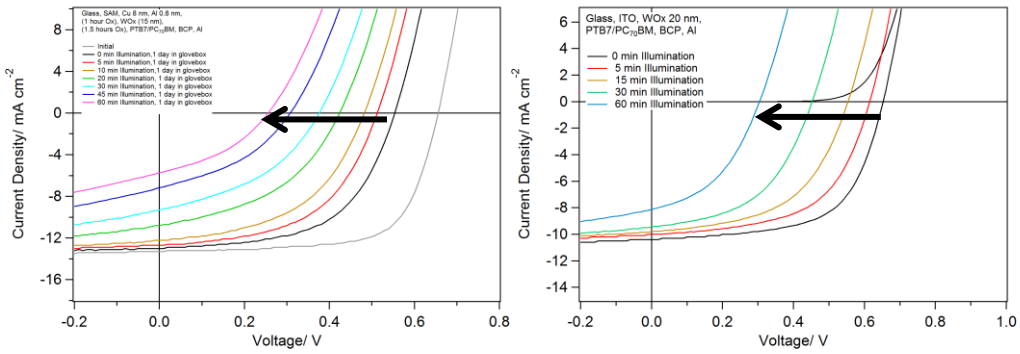

Figure 5.6: *JV* scans under constant illumination. The full device structure is as follows: Glass | SAM | Cu 8 nm | Al 0.8 nm | 1 hr Ox | WO_{3-x} 15 nm | 1.5 hrs Ox | PTB7/PC_{70}BM | BCP 8 nm | Al (left) and Glass | ITO | WO_{3-x} 20 nm | PTB7/PC_{70}BM | BCP 8 nm | Al (right). *JV* scans after 0, 5, 10, 20, 30, 45 and 60 minutes under constant illumination are coloured in black, red, yellow, green, light blue, dark blue and purple respectively for the left figure. These scans were recorded after 1 days storage in a nitrogen filled glovebox, with the exception of the initial device characterization, which is shown in grey. *JV* scans after 0, 5, 15, 30 and 60 minutes are coloured in black, red, orange, green and blue respectively for the right figure.

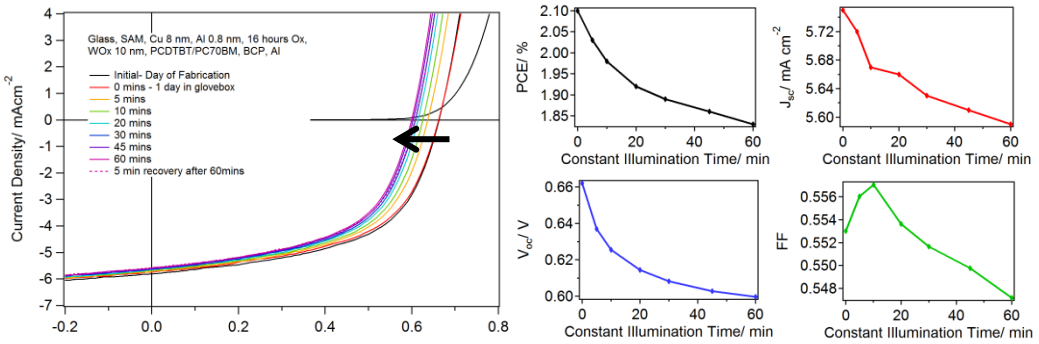

Figure 5.7: Left: *JV* scans under constant illumination using the PCDTBT/PC_{70}BM polymer system. The full device structure is as follows: Glass | SAM | Cu 8 nm | Al 0.8 nm | 16 hrs Ox | WO_{3-x} 10 nm | PCDTBT/PC_{70}BM | BCP 8 nm | Al. *JV* scans after 0, 5, 10, 20, 30, 45 and 60 minutes under constant illumination are coloured in red, yellow,

green, light blue, dark blue, purple and pink respectively. A scan after being in the light for 60 minutes, left in the dark for 5 minutes and then immediately rescanned is also shown in dotted pink. These scans were recorded after 1 days storage in a nitrogen filled glovebox, with the exception of the initial device characterization, which is shown in black. Right: *PCE*, J_{sc}, V_{oc} and *FF* as a function of constant illumination time for the same OPV.

Figure 5.6 shows that these cells are very unstable under constant illumination, with the J_{sc} and V_{oc} deteriorating to less than half their initial values after 60 minutes. However, device degradation can result from a number of parallel mechanisms some of which are unrelated to the electrode or its interface with the semiconductor material. OPVs with the same electrode structure but with a different BHJ system were then fabricated, to ascertain if this instability was caused by the electrode or another part of the device (Figure 5.7). The rapid degradation under constant illumination shown in Figure 5.6 is also present for devices fabricated on ITO electrodes. This shows that the observed lack of stability under constant illumination is inherent within the PTB7/$PC_{70}BM$ polymer system, and not the electrode studied in this chapter.

To test this hypothesis, devices were fabricated with a different BHJ system, PCDTBT/$PC_{70}BM$, and the current-voltage characteristic as a function of time under constant illumination is shown in Figure 5.7. This Figure shows that the Cu | Al | WO_{3-x} electrode is stable under constant illumination for 1 hour compared to the devices fabricated on Cu electrodes in Figure 5.6. OPV devices fabricated with the same electrode structure and a different BHJ are much more stable under constant illumination,

demonstrating that the fast degradation shown in Figure 5.6 is due to the BHJ, and not the electrode.

Finally, in order to improve the transparency of this electrode for light wavelengths below 550 nm and improve electrode stability towards oxidation in air, bilayer electrodes of Cu and Ag were fabricated. In this case the total metal thickness was kept at 8 nm: 4 nm of Cu was buried beneath 4 nm of Ag, since Ag is much more stable towards oxidation and Cu binds strongly to the molecular adhesive layer at the glass surface. Figure 5.8 shows that combining Ag with Cu improves the transparency for wavelengths <550 nm although this is at the expense of reduced transparency for wavelengths >550 nm since Ag absorbs light more strongly at longer wavelengths.[86] Using this electrode in conjunction with a 20 nm WO_{3-x} layer dramatically increases the transparency of the Cu | Ag films across a large range of wavelengths by 20-25%, as shown Figure 5.8.

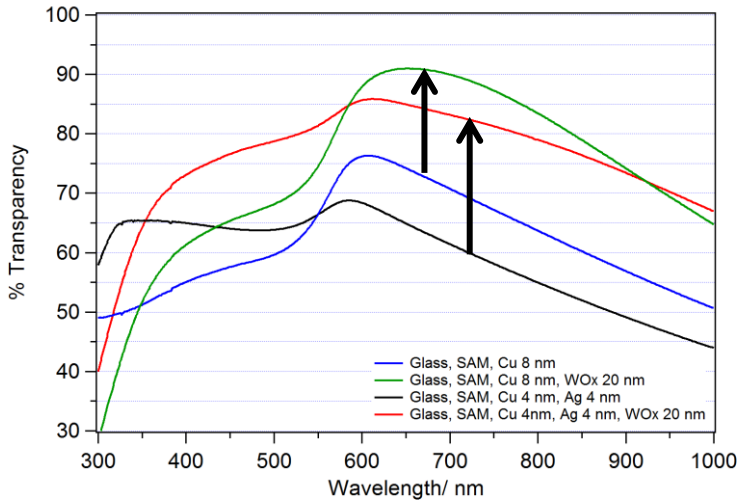

Figure 5.8: Far-field transparency of Cu 8 nm, Cu 8 nm | WO_{3-x} 20 nm, Cu 4 nm | Ag 4 nm and Cu 4 nm | Ag 4 nm | WO_{3-x} 20 nm films on SAM derivatised glass.

Unfortunately these bilayer electrodes also oxidise in air as is evident from the gradual increase in sheet resistance with time exposed to air. This is shown in Figure 5.9. Notably, the Cu | Ag films in Figure 5.9 increase in sheet resistance at a slower rate than for Cu only films (Figure 3.3). In an attempt to completely passivate the bilayer electrode the Al surface passivation method was investigated and the results are shown in Figure 5.10.

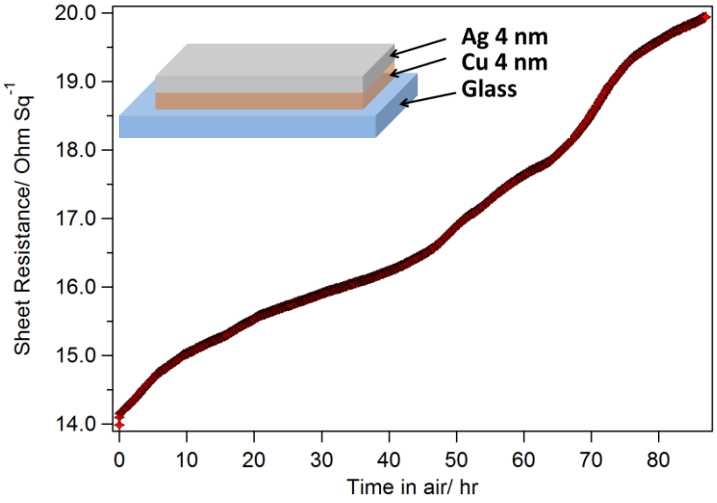

Figure 5.9: Sheet resistance as a function of time in air for a Cu 4 nm | Ag 4 nm film on glass with a mixed SAM.

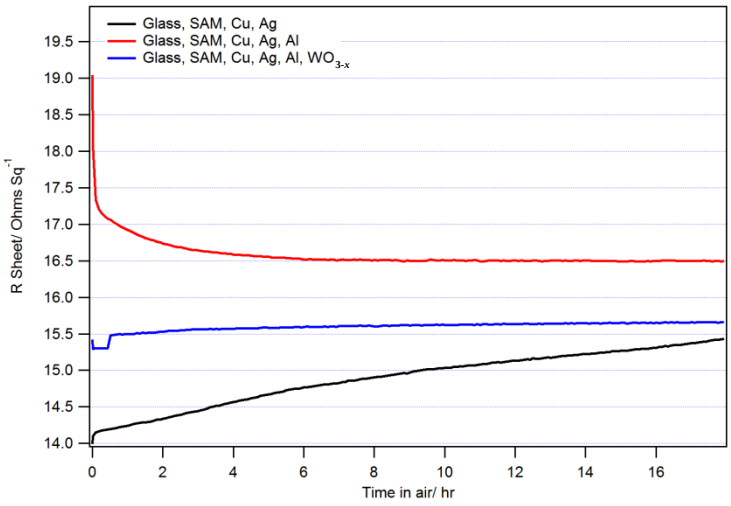

Figure 5.10: Sheet resistance as a function of time in air for Cu 4 nm | Ag 4 nm, Cu 4 nm | Ag 4 nm | Al 0.8 nm and Cu 4 nm | Ag 4 nm | Al 0.8 nm | WO_{3-x} 20 nm, shown in black red and blue respectively. All films are supported on mixed SAM derivatised glass substrates.

Figure 5.10 shows that the 0.8 nm Al layer successfully passivates Cu | Ag films from oxidation in air with or without a WO_{3-x} overlayer on the surface. This result in conjunction with the large increase in transparency for the Cu | Ag film with a WO_{3-x} overlayer bodes well for its potential as a window electrode for OPV.

It is often the case that part of the OPV fabrication process involves annealing of the substrate, and is therefore important to know how electrodes respond to annealing. Figure 5.11 illustrates the changes in sheet resistance for Glass | SAM | Cu | Ag electrodes with and without Al and WO_{3-x} overlayers upon annealing under nitrogen at various temperatures. Figure 5.11 shows that the Cu | Ag films exhibit good thermal stability. Whilst the thermal stability of these Cu | Ag films is still relatively high, with comparable or lower sheet resistance values up to 250 °C for all films shown, the thermal stability of the Cu films is higher still.

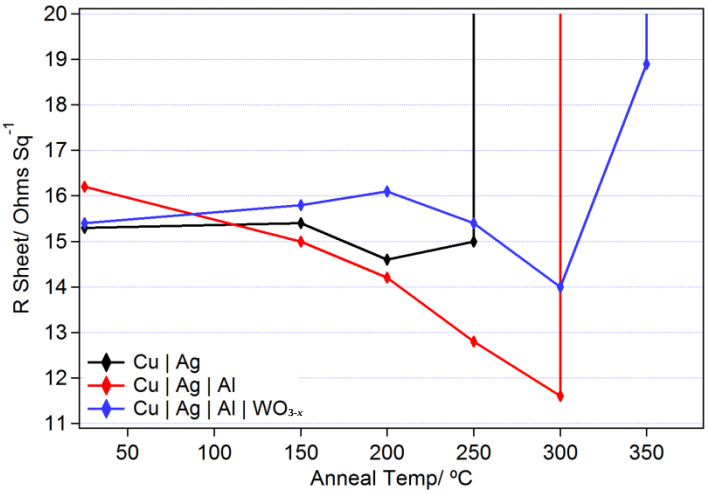

Figure 5.11: Sheet resistance of Cu 4 nm | Ag 4 nm, Cu 4 nm | Ag 4 nm | Al 0.8 nm, and Cu 4 nm | Ag 4 nm | Al 0.8 nm | WO_{3-x} 20 nm films after heating successively at varying temperatures under nitrogen, shown in black, red and blue respectively. Films are supported on mixed SAM derivatised glass, and all heating was carried out for 10 minutes under nitrogen.

5.5 Conclusions

The triple layer Cu | Al | WO_{3-x} electrode described in this chapter retains many of the advantages of the bilayer electrode described in Chapter 4 such as a low cost, high transparency, low sheet resistance and efficient OPV device characteristics. However, this electrode also has the advantage of air stability, which has been achieved through the use of an oxidised Al layer inserted between the Cu and WO_{3-x} layers. The disadvantage of the electrode is the extra complexity and cost associated with using an additional layer.

The transparency of Cu | Ag | WO_{3-x} electrodes is very promising, with higher transparency up to 600 nm than the Cu | WO_{3-x} films presented in Chapter 4. This combined with low sheet resistance, ability to be rendered air stable and relatively high thermal stability bodes well for its application as an electrode in OPVs.

Chapter 6 – Plasmon-active Cu Electrodes

6.1 Abstract

This chapter describes a method for forming ultra-thin Cu films on plastic (PET) substrates with and without a high density of sub-wavelength apertures. Experiments designed to investigate the possibility that these electrodes can serve as plasmon-active light trapping electrodes in both small molecule and polymeric OPVs are described. The results show that these electrodes have potential as low cost plasmon-active electrodes in OPVs.

6.2 Background

Optically thin, Au and Ag electrodes with a random array of sub-wavelength apertures supported on flexible plastic substrates were recently shown by Stec *et al.* to be a viable alternative to ITO in bulk-heterojunction and small molecule OPVs.[97] In that work the apertures were formed in a continuous optically thin metal thin film by rapid thermal annealing; a method that is both efficient and scalable. Whilst the high density of sub-wavelength apertures dramatically reduced the far-field transparency of the electrodes, they were shown to outperform those without apertures and ITO glass in both small molecule and polymer based OPV devices. That result has since been corroborated by Xu *et al.*[234] for Ag electrodes using a different approach to random aperture formation. The large reduction in far-field transparency occurs because apertures in a metal film that are much smaller than the wavelength of the incident light couple strongly with that light, much like nanoparticles of the same metal.[97] This strong optical absorption is due to the excitation of surface plasmon resonances that are localised on the aperture circumference. Just as for metal nanoparticles, the resonant frequency of aperture excitations is a

function of the metal, the size and the shape of the aperture. The coinage metals Ag, Au and Cu all support surface plasmons with frequencies in the visible part of the electromagnetic spectrum making them well matched to the solar spectrum. Since thermal annealing gives rise to a random distribution of aperture shapes and sizes, a broad range of photons can be absorbed, which is a further advantage for PV applications. Localised surface plasmon resonances are effectively light trapped as collective oscillations of conduction band electrons at the metal–dielectric interface, the intensity of which decays exponentially into the semiconductor and metal.[33] Ordinarily, these bound electromagnetic waves eventually dissipate their energy as Ohmic losses in the metal. However, if the electrode is in very close proximity to a semiconductor with a high absorption coefficient, such as an organic semiconductor, then these bound electromagnetic waves can dissipate their energy by exciting electrons from the HOMO to the LUMO in the adjacent organic semiconductor rather than as heat in the metal. In the context of an OPV this trapped light can therefore be harvested, provided the semiconductor is in close proximity to the nanostructured metal electrode. This beneficial effect must however be balanced against the need to prevent exciton quenching by the metal electrode and so it is expe cted that a charge selective layer of a few nm in thickness should be incorporated at the interface.[185] This proximity requirement combined with the relatively low absorption coefficient in crystalline silicon over a broad range of wavelengths rules out the effective use of plasmonics in conventional Si based PV technologies.

Reilly III *et al.* were the first to utilise a metal electrode with apertures as a plasmon-active electrode in OPVs. In that work the apertures were of uniform size and shape and were formed in a 30 nm Ag electrode using microsphere lithography. Figure 6.1 shows the data taken from that report which provides evidence for plasmon-enhanced

light absorption in OPVs.[235] The data is presented as the ratio between the incident-photon-to-converted-electron (IPCE) ratio and the far-field transparency. For a Ag electrode with a random array of 92 nm diameter circular apertures, the IPCE is highest over the wavelength range that the electrode is least transparent, which is indicative of light trapping as surface plasmon excitations.

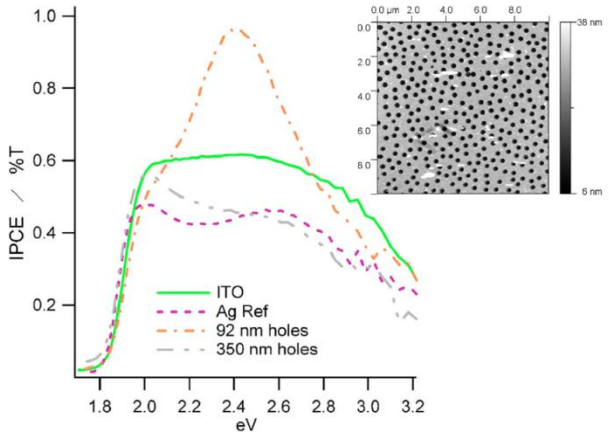

Figure 6.1: IPCE:transparency ratio against wavelength for OPVs using various window electrodes with and without circular apertures.[235] Inset: An AFM image of the plasmon-active metal electrode that proved most effective.

The work of Stec *et al.*[97] was a significant improvement on that of Reilly III *et al.*, because the electrodes reported by Stec *et al.* outperformed conventional ITO in OPV devices with the same structure, as well as their non-annealed counterparts. Figure 6.2 reproduces the most important figures from that work.

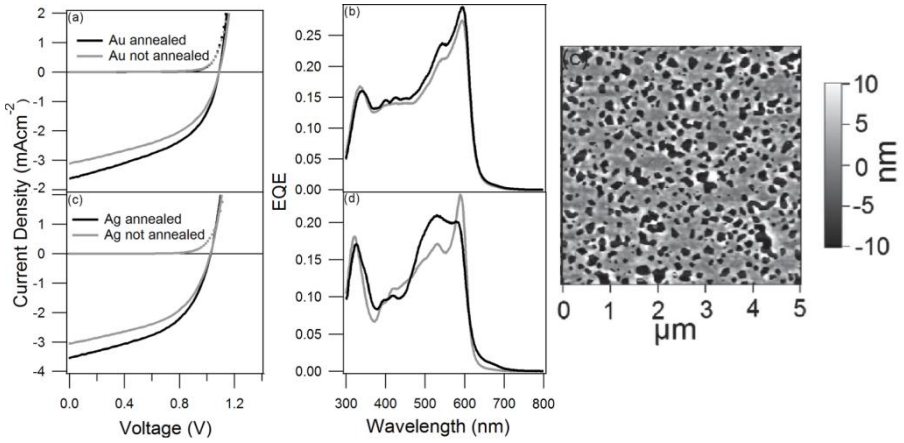

Figure 6.2: *JV* scans (left) and EQE spectra (middle) of model OPV devices fabricated on Ag and Au electrodes with and without apertures (denoted *annealed* and *non-annealed* respectively). AFM image of a Au electrode with apertures (right).[97]

It is evident from Figure 6.2 that the performance of model BHJ OPVs is improved when using a random aperture Ag electrode (denoted as *annealed*) as compared to devices using an electrode without apertures (denoted as *non-annealed*). The increase in exciton generation in close proximity to the nanostructured electrode gives rise to an increase in photocurrent, with the V_{oc} and *FF* mostly unaffected.[122] Importantly the spectral response of OPV devices with apertures is quite different to that without, with increased photocurrent generation occurring only for light frequencies at or below the surface plasmon frequency of the metal.[122,124]

Ag and Au are the most widely used materials for plasmonic applications because the SPR is in the visible range, they are relatively stable towards oxidation and they have the lowest Ohmic losses amongst metals.[115] However, Cu can also support SP resonances in the visible part of the spectrum, has Ohmic losses comparable to Au for

light wavelengths 600-750 nm[115] and is one hundredth of the cost of Ag.[93] Unfortunately Cu has the disadvantage that it is much more susceptible to oxidation than Ag. In principle, if Cu could be stabilised towards oxidation without deteriorating its optical properties it would be a low cost alternative to Ag and Au for plasmon-active electrodes for OPV.

PET is an attractive substrate material for OPVs because it is widely used in flexible electronics and has a high transparency between 400 and 900 nm (Figure 2.1). Importantly PET is also available with a very low roughness (Figure 6.3) making it suitable for thin film PVs such as OPVs. Low substrate roughness is essential for the formation of continuous ultra-thin metal films, because the metal film invariably forms as an array of interconnected islands when the substrate is rough which compromises the conductivity. It is also important to minimise the risk of shunt formation which is more likely to occur for substrates with high surface roughness as discussed in Section 1.8.

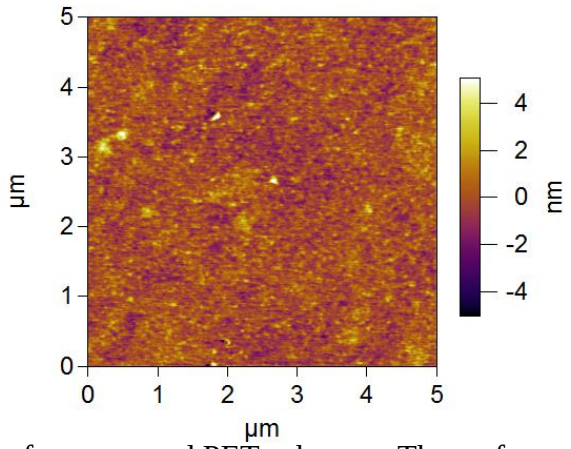

Figure 6.3: AFM image of an uncoated PET substrate. The surface roughness is 0.8 nm.

This chapter describes the results of experiments designed to investigate the potential of ultra-thin Cu and Cu | Ag bilayer films supported on PET for random

aperture array plasmon-active electrodes. The work presented in this chapter is on-going and has not yet been published.

6.3 Experimental

Preparation of ultra-thin electrodes on PET: PET slides were cut, cleaned and UV/O_3 treated where stated as described in Chapter 2. For Cu | Ag films the metal deposition was carried out consecutively by thermal evaporation without breaking the vacuum. This was not the case for Cu | Al films. Some substrates were then annealed in the glovebox at varying temperatures, either before or after Al or Ag deposition. 200 °C was chosen as the standard annealing temperature to form apertures because PET cannot withstand temperatures greater than ~250 °C and at lower temperatures annealing to introduce morphological change in the films would take much longer. All substrate annealing was carried out in a nitrogen filled glovebox with ≤5 ppm of O_2 and H_2O at 200 °C for 25 mins unless otherwise stated. For much of the initial electrode characterisation 0.8 nm of Al was deposited on Cu 8 nm films after annealing to prevent oxidation of the films, since the SEM, UV/visible spectroscopy and AFM require the films be exposed to the laboratory atmosphere.

PET orientation: The PET substrate had one side too rough for OPV electrode fabrication. The smooth side (Figure 6.3) was determined by AFM and subsequently used throughout.

Copper oxide etching: PET | Cu 8 nm | Annealed | Al 0.8 nm films were placed in glacial acetic acid for 20 seconds, rinsed with water and blown dry with nitrogen.

Sheet resistance measurement: The PET substrates were mounted using a glass backing slide to ensure they were flat.

AFM imaging: Imaging using the AFM proved to be very difficult due to movement of the PET whilst imaging. In order to alleviate this, PET substrates were taped to the stage to ensure stability whilst scanning.

Optical transparency measurement: The reference material was an uncoated PET substrate with the exception of Figure 6.12 where the reference is air. The incident beam passed through the PET first of all as is the case in an OPV device.

6.4 Results and Discussion

The transparent substrate that ultra-thin metal films are supported on has a strong influence on film morphology and transparency as shown in Figure 6.4.

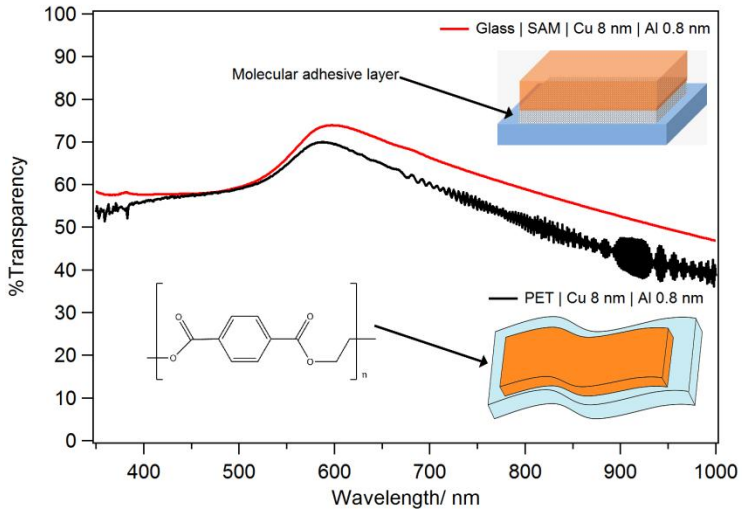

Figure 6.4: Far-field transparency spectra of a Cu 8 nm | Al 0.8 nm films supported on untreated PET (black) and glass modified with a mixed SAM (red). Inset: Schematic illustrations of substrates and film morphology for Cu on glass with a molecular adhesive layer (above) and untreated PET (below).

Figure 6.4 shows that the transparency of a Cu 8 nm | Al 0.8 nm film is higher when deposited onto glass modified with a molecular adhesive layer than on untreated

PET. On glass the molecular adhesive layer provides a reactive surface for the incoming Cu atoms, in contrast to the untreated PET where there are no such reactive moieties to which the Cu can bind strongly. PET can however be modified with the same molecular adhesive layer as used on glass so that the transparency of ultra-thin metal films are almost identical to that achieved on glass.[86] The difference in transparency of the films in Figure 6.4 is due to morphological differences in the films. The films on glass modified with a reactive SAM are more uniform and continuous because the incoming Cu atoms are immobilised on contact with the substrate. This is *in-contra,* to the films on untreated PET that have grown in an island-like manner in order to minimise surface energy in the absence of a strong interaction with the substrate. These rougher Cu films on PET result in plasmonic absorption losses in the metal film for light wavelengths >600 nm. Absorption in optically thin metal films due to surface plasmon excitation is ordinarily considered to be lost energy and can be suppressed using an overlayer that shifts the SPR frequency into the UV part of the spectrum i.e. away from the resonant condition.[87] Conversely, the work presented in this chapter focuses on trying to use this effect to concentrate light in OPVs, with particular emphasis on the utilisation of Cu for this purpose.

For reliable formation of a random array of sub-wavelength apertures in Cu films, a method for controlling adhesion of Cu to the PET substrate was required. Stec *et al.* have shown that for Ag films on PET, adhesion can be greatly improved by UV/O_3 treating the plastic prior to Ag deposition, and so by tuning the UV/O_3 treatment time and annealing under nitrogen plasmon-active films can be produced.[97] In the first instance the possibility of applying this method to Cu electrodes was investigated. UV/O_3 treatment introduces reactive moieties on the surface of the plastic substrate, causing the incoming

metal atoms to adhere more strongly than when untreated. These reactive moieties are oxygen based and include carboxylic acid moieties, a functional group that is known to bind with Cu.[97] UV/O_3 pre-treatment of PET results in more continuous Cu films, as is evident from the lower initial sheet resistance values given in Table 6.1.

	Initial / Ω sq^{-1} ±1 SD	**Final / Ω sq^{-1}** ±1 SD	**Optical Appearance**
No UV/O_3	26 ± 2	28 ± 3	Turned dull green upon heating
2 min UV/O_3	12 ± 2	9 ± 1	No Change
5 min UV/O_3	12.0 ± 0.3	8 ± 1	No Change

Table 6.1: Sheet resistance values of Cu 8 nm | Al 0.8 nm films on PET before and after annealing.

Testing the conductivity of films after heating is important to ensure that annealing to form apertures did not dramatically change the sheet resistance, since the sheet resistance of the window electrode is an important determinant of the performance of OPVs. The sheet resistance data given in Table 6.1 shows that Cu films on PET with 2 or 5 min UV/O_3 treatment prior to metal deposition are stable at 200 °C. In fact, the sheet resistance actually decreases upon annealing which is attributed to an increase in metal crystallinity, as has been observed for ultra-thin Au films on plastic substrates.[86] Conversely, for films with no UV/O_3 treatment the sheet resistance upon annealing is altered by two competing processes; (i) apertures formed in the film scatter electrons which serves to increase the resistance; (ii) the increase in crystallinity serves to decrease the resistance. Thus it is unsurprising that the sheet resistance of Cu films supported on

unoxidised PET remains essentially unchanged upon annealing. Importantly none of the Cu film electrodes exhibit a large enough sheet resistance change upon annealing to drastically alter device performance in the small area OPVs fabricated in this study. A sheet resistance of 28 Ω sq^{-1} is however too high for large area OPVs, although sufficient for this fundamental research.

The robustness of the Cu electrodes fabricated on PET with and without UV/O_3 pre-treatment was assessed by recording the sheet resistance before and after various tests and the results are summarised in Table 6.2. The results show that the films are very robust which is important for OPVs, as prior to organic semiconductor deposition electrodes are often cleaned by ultra-sonic agitation (denoted "10 min H_20 agitation") and UV/O_3 treatment. Applying sticky tape to the electrode and subsequently removal by pulling it off by hand (denoted *Tape test*) is a harsh adhesion test often used in research laboratories.[175,236,237]

UV/O_3	**Initial/ Ω sq^{-1}**	**Process**	**Final/ Ω sq^{-1}**
None	25.2	10 min H_2O agitation	28.9
None	24.4	UV/O_3 5 min	25.8
None	25.8	Tape test	26.5
5 min	13.9	10 min H_2O agitation	15.7
5 min	14.4	UV/O_3 5 min	15.2
5 min	15.2	Tape test	22.2

Table 6.2: Sheet resistance values of PET | Cu 8 nm | Al 0.8 nm films before and after various electrode cleaning methods used in OPV fabrication. The initial sheet resistance values in Table 6.2 do not match those in Table 6.1 because the data shown here was

recorded on older electrodes, with the data being recorded in air so some oxidation will have taken place.

Figure 6.5 shows the morphology changes upon annealing at 200 °C for 25 mins with and without UV/O_3 treatment for Cu films on PET. The images on the top row of Figure 6.5 (a & b) show the topography of Cu films on PET that underwent no UV/O_3 pre-treatment prior to Cu deposition. Upon annealing the surface roughness increases from ~1.3 nm to ~3.5 nm. This increase in roughness may have resulted from the formation of apertures as reported for annealed Ag films on UV/O_3 treated PET by Stec *et al*.[97] Figures 6.5 (c & d) show the topography of Cu films on UV/O_3 treated PET before and after annealing. In this case the surface roughness remains similar upon annealing, consistent with strong binding of the Cu to the underlying PET.

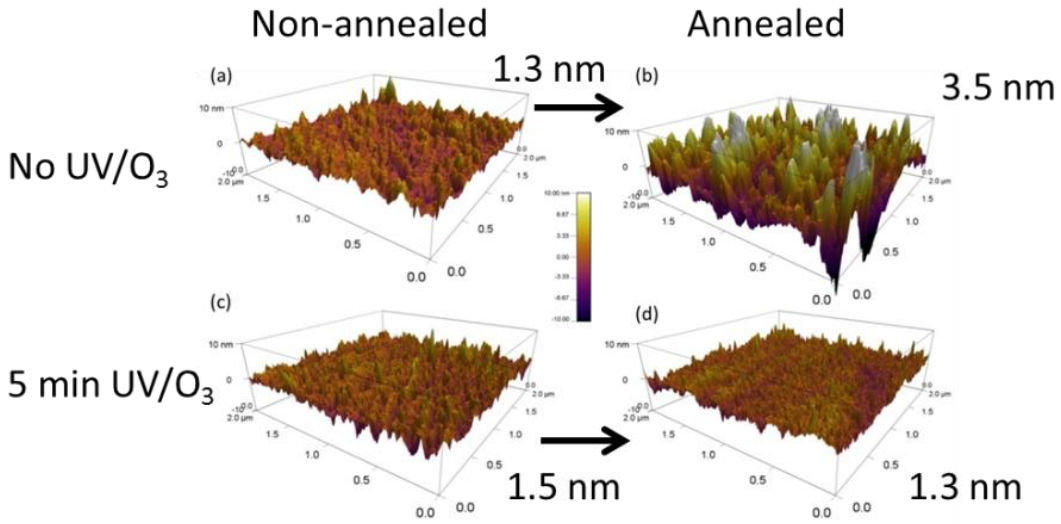

Figure 6.5: AFM images of Cu 8 nm | Al 0.8 nm films on PET with no UV/O_3 (a) and (b) and 5 minutes UV/O_3 treatment (c) and (d), with no annealing (a) and (c) and after annealing (b) and (d). The surface roughness is also given for each case.

There is no evidence of apertures in the AFM image Figure 6.5(d) despite annealing, showing that the adhesion to the substrate is too high to induce apertures upon annealing. Careful inspection of the 2-D AFM images of the films shown in Figures 6.5 (a & b), given in Figure 6.6, appear to show that apertures have formed in the films after annealing (white circles), since there are visible depressions or valleys below the 4 nm mark on the height scale. More convincing evidence for aperture formation is provided by the SEM images shown in Figure 6.7, where apertures correspond to the black areas. Evidence of sub-visible light wavelength apertures are key to justifying any observed plasmonic effects. To achieve aperture formation, Cu 8 nm films were evaporated onto untreated PET substrates and annealed at 200 °C for 25 mins.

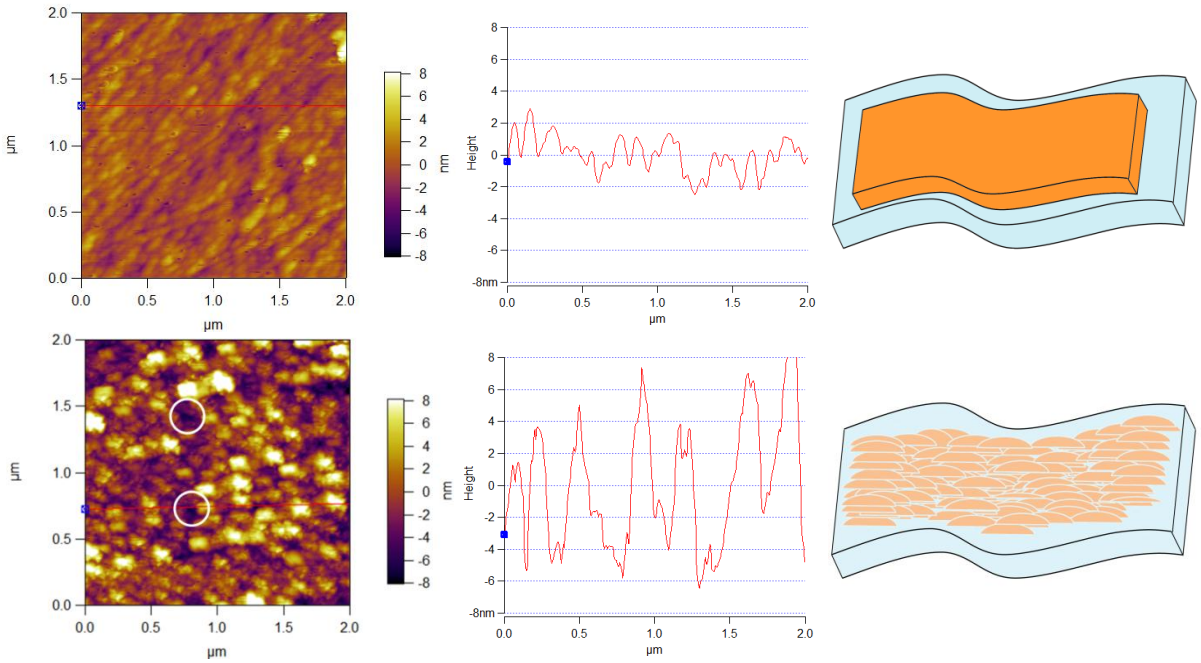

Figure 6.6: 2-D AFM images (left), and cross-sections of the same images (middle) of Cu 8 nm | Al 0.8 nm films on non-UV/O_3 treated PET substrates. The top scan shows a non-annealed film and the bottom scan shows a film that was annealed. The red lines on the images on the left show the lines where the cross sections were taken, and which apertures in dissects in the bottom scan. White circles illustrate two possible aperture

sites on the bottom AFM image. A schematic of film morphology is shown for each image (right).

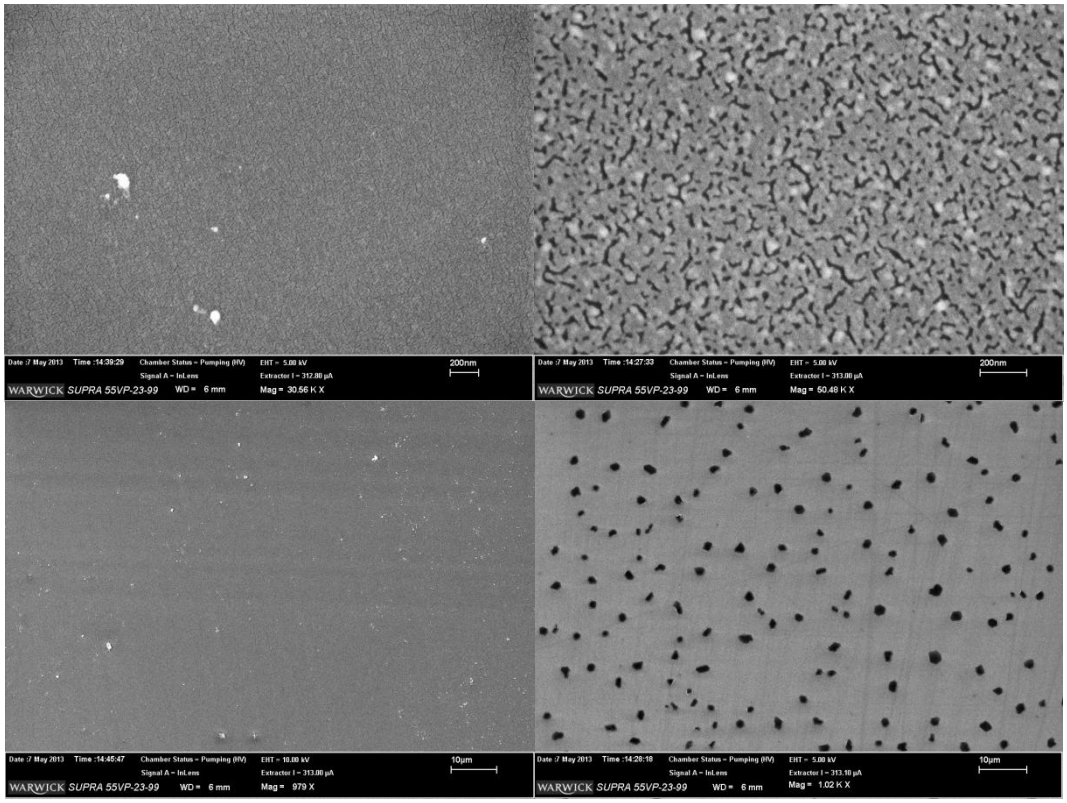

Figure 6.7: SEM images of Cu 8 nm | Al 0.8 nm films on PET before (left) and after (right) annealing at 200 °C for 25 mins. The upper images show fine structure (200 nm scale bars) and the lower images show larger structures (10 µm scale bar).

Importantly, it is evident from Figure 6.7 that the apertures (small features) formed upon annealing Cu films deposited onto untreated PET are not conjoined, so the sheet resistance is not drastically changed; 26 Ω sq^{-1} and 28 Ω sq^{-1} before and after annealing respectively. It is possible that these apertures may have formed as a result of grain boundaries opening up or by merger of smaller apertures. Importantly, they are

100s of nms in length and 10s of nms in width and so sub-optical wavelength in size, which means that they interact strongly with light. Formation of apertures by annealing Cu films deposited onto UV/O_3 treated PET was not possible because the films adhered too strongly to the substrate. UV/O_3 treatment is therefore a reliable way to form very robust Cu films. Unless otherwise stated plasmon-active electrodes were fabricated on PET substrates that were not UV/O_3 treated.

In addition to the sub-micron changes in Cu film morphology shown in Figure 6.7 (upper), large uniformly dispersed features also appear on the electrodes upon annealing, as shown in the SEM images in Figure 6.7 (lower). These structures grow in size when the annealing time is increased from 25 to 60 minutes, as shown in Figure 6.8. Assuming these structures are Cu based, the large spaces between them indicates that the Cu is highly mobile, possibly due to the low film thickness and elevated temperatures.[185]

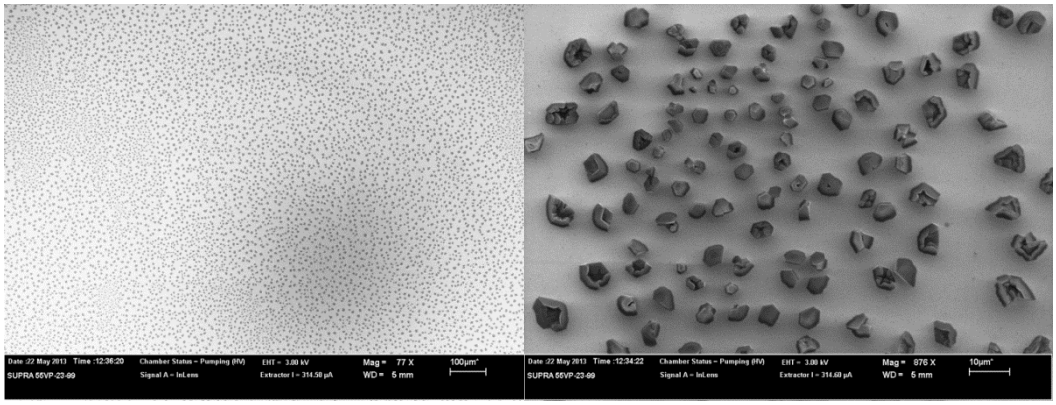

Figure 6.8: SEM images of Cu 8 nm | Al 0.8 nm films on PET after annealing at 200 °C for 60 minutes. The images show large structures (10 µm scale bar).

The height of these much larger flower-like structures was confirmed using AFM (Figure 6.9) to be ~ 250 nm, which is information that could not be gained using SEM.

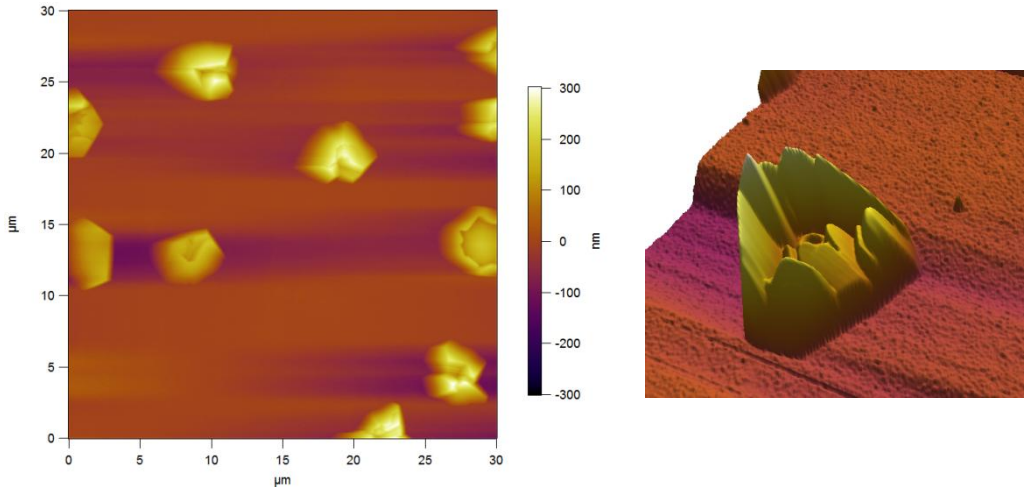

Figure 6.9: AFM scan (left) of an annealed (200 °C for 25 mins) Cu 8 nm | Al 0.8 nm film on PET. A 3-D plot of an individual structure from the same image revealing the shape (right). Some image artefacts are present, shown as the purple horizontal streaks on either side of the tall structures.

As discussed later in this chapter, these electrodes were successfully used in small molecule OPV devices. It is surprising that OPV devices with a semiconductor layer thickness of only ~60 nm could function on electrodes with structures as tall as those in Figure 6.9. A possible reason why these electrodes did not result in OPV devices that short circuit may be their relatively large aspect ratio, which reduces the likelihood of problems associated with shadowing effects when depositing the different layers that make up the device. Alternatively these structures are electrically insulating and so do not interfere with the electrical integrity of the device. Since there are trace amounts of oxygen present in the glovebox (≤5 ppm) it was proposed that these flower like structures

were most likely copper oxide. To test this hypothesis, annealed Cu electrodes were etched with acetic acid, since acetic acid is known to etch Cu(I) and Cu(II) oxides much more rapidly than Cu metal.[238] AFM images after this treatment are shown in Figure 6.10.

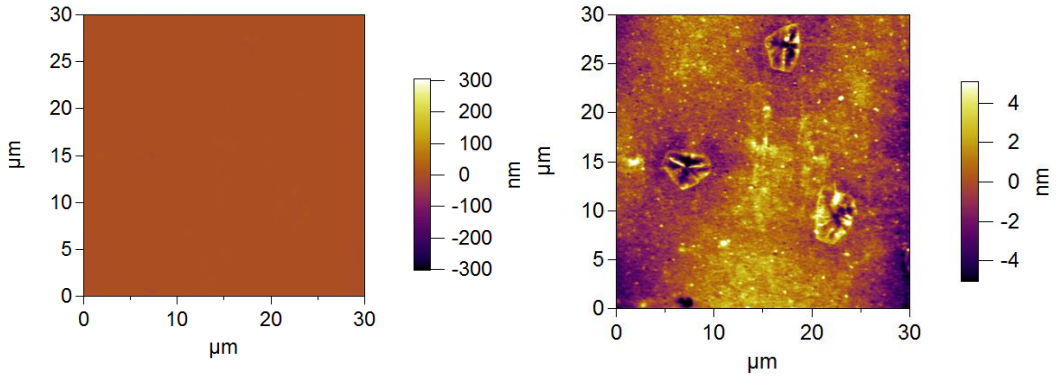

Figure 6.10: AFM images of an annealed Cu 8 nm | Al 0.8 nm film on PET after etching with acetic acid. The right image has a scale bar of 8 nm and the left has a scale bar of 600 nm to match the scale used in Figure 6.9.

Figure 6.10 shows that these structures have been removed by etching with acetic acid. The Cu films were still present after etching, since Cu metal is not rapidly etched by acetic acid.[238] This is strong evidence that they are copper oxide. The left hand image has the same height scale as used to image the flower-like structures before etching. A much smaller height scale is used for the right hand image, from which it is clear where the structures were initially located. Associated with the formation of apertures and the increase in roughness upon annealing is a large decrease in the transparency of the films as shown in Figure 6.11. This can be observed by eye, as the films are noticeably duller/ darker.

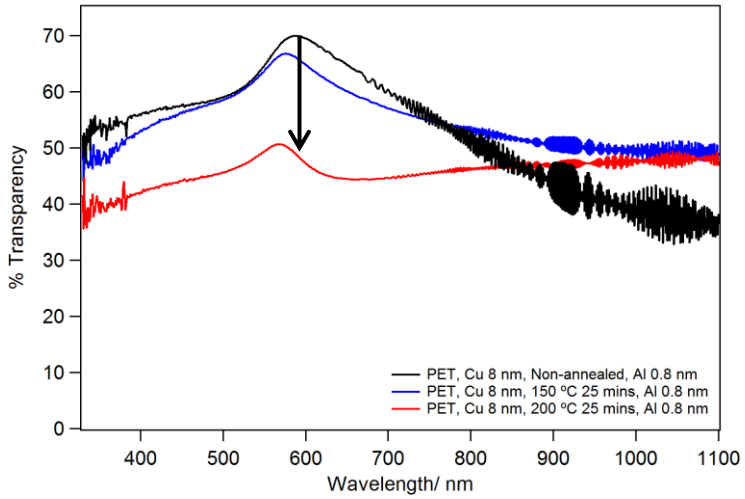

Figure 6.11: Far-field transparency spectra of Cu 8 nm | Al 0.8 nm films on PET, with and without annealing. The PET | Cu | Al films are coloured in black, blue and red for non-annealed, 150 °C for 25 min annealed and 200 °C for 25 min annealed respectively.

Notably, the transparency of these electrodes does not decrease uniformly across the spectrum and the annealed films have a much flatter response. In Figure 6.11, the decrease in transparency for a Cu film on PET is very small upon annealing at 150 °C and much larger upon annealing at 200 °C, with a decrease of 5-20% across the visible part of the spectrum where the solar flux is greatest. Interestingly, upon annealing at 200 °C the transparency of the films past ~800 nm actually increases. The reduced transparency likely originates from a combination of; (i) scattering of light caused by the large structures shown in Figure 6.7.; (ii) Absorption from these copper oxide structures;. (iii) Nano-scale changes in the morphology of the films, rendering them plasmonically active; the incoming light is coupled into the film after annealing. The change in the transparency of PET upon annealing at 100, 150 and 250 °C for 25 minutes is shown in Figure 6.12 from which it is clear that the observed changes in transparency are due to the morphology changes in the Cu film and not due to a reduced transparency of the substrate

itself, since upon annealing PET films at 200 °C for 25 mins the transparency only decreases by ~1%.

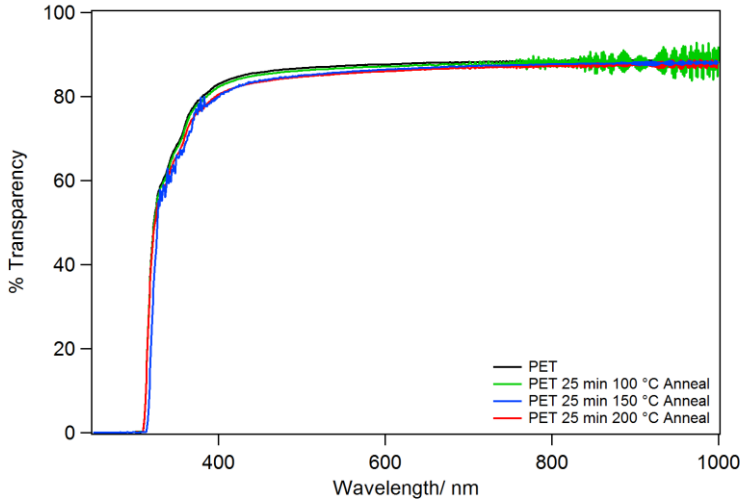

Figure 6.12: Far-field transparency spectra of uncoated PET without annealing, after annealing at 100 °C for 25 min, after annealing at 150 °C for 25 min and after annealing at 200 °C for 25 mins coloured black, green, blue and red respectively. These spectra are referenced against air.

To test the utility of these electrodes as plasmon-active electrodes in OPVs, model devices were fabricated using Cu electrodes with and without apertures, denoted *annealed* and *non-annealed* respectively. CuPc was chosen as a suitable electron donor material because it absorbs light with wavelengths as long as 750 nm (Figure 6.13) and its peak absorption is matched to the peak transparency of Cu window electrodes. An organic semiconductor that absorbs in the long wavelength region is needed to observe plasmonic effects because the SPR frequency for Cu is at a lower frequency than for Ag or Au.[120,87] Notably, the plasmon-active region for Cu electrodes is therefore well-

matched to the newest generation of BHJ polymer systems which harvest light in the near infra-red as well as the visible part of the solar spectrum.

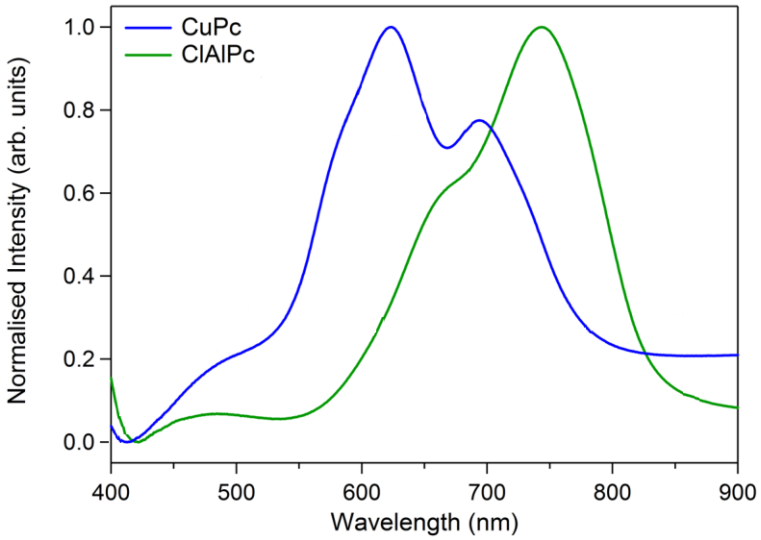

Figure 6.13: Normalized absorption spectra for thin films of the small molecule organic donor materials CuPc (blue) and ClAlPc (green).[69]

Figure 6.14 shows the *JV* response of model OPV devices fabricated on PET | Cu electrodes with and without annealing. The associated EQE spectra of these cells are shown in Figure 6.15.

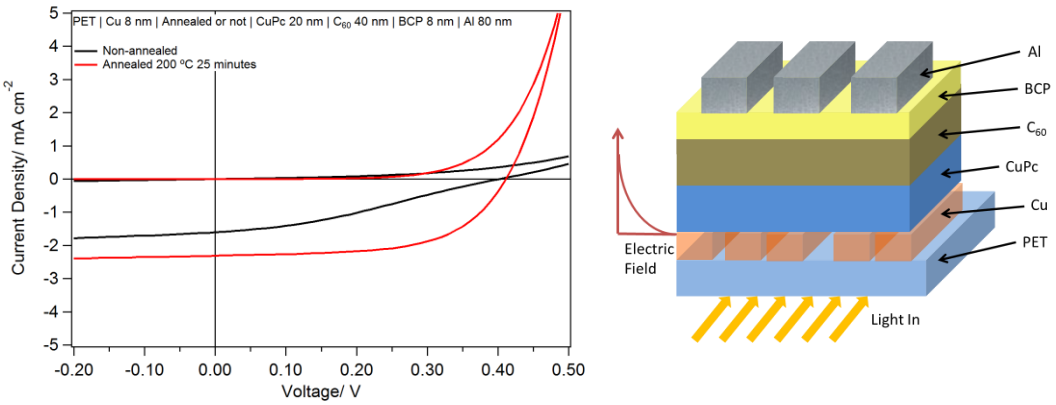

Figure 6.14: Left: Representative *JV* characteristics of OPV cells with the structure PET | Cu 8 nm | CuPc 20 nm | C_{60} 40 nm | BCP 8 nm | Al 80 nm with (red) and without (black) annealing of the Cu electrode.

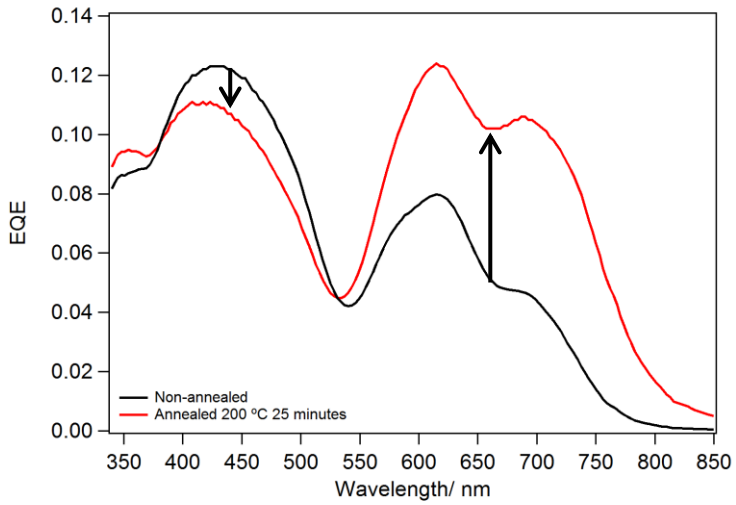

Figure 6.15: EQE spectra of OPV cells with the structure: PET | Cu 8 nm | CuPc 20 nm | C_{60} 40 nm | BCP 8 nm | Al 80 nm with (red) and without (black) annealing of the Cu electrode.

It is clear from Figure 6.14 that the photocurrent of OPVs fabricated on electrodes with apertures (i.e. annealed) is significantly greater than that without, despite the former having a much lower far-field transparency (Figure 6.11). It is evident from

Figure 6.15 that OPVs fabricated on electrodes with apertures have a much higher EQE response in the long wavelength part of the spectrum, which is the reason for the higher J_{sc}. It is in this wavelength region that CuPc is absorbing photons, and thus in the devices fabricated on electrodes with apertures (red) the extra photocurrent is generated by the CuPc layer. Plasmon assisted light absorption is localised near to the electrode, because the SPR is trapped at the electrode-semiconductor interface and so the optical field intensity decays exponentially into the semiconductor. Since the CuPc layer is spatially closest to the Cu electrode it is best placed to benefit from the high optical field intensity associated with SPRs. The JV characteristic and spectral response are therefore consistent with plasmon enhanced absorption. There is no significant enhancement in the region over which C_{60} absorbs (< 550 nm) because this corresponds to light frequencies above the SPR frequency associated with the apertures in the Cu film and the C_{60} layer is located away from the region of highest optical intensity. It is not possible to rule out the possibility that the lower *JV* performance of the devices fabricated on non-annealed electrodes may be due, in part, to a thin oxide layer formed on the electrode that is not present on non-annealed electrodes, causing the CuPc layer to adopt a different orientation on the electrode surface which would alter the interfacial energetics.[239] To exclude this possibility, and to test the generality of the result obtained in Figure 6.14, OPV cells were fabricated using another donor material; ClAlPc, in conjunction with a MoO_3 hole-extraction layer. ClAlPc was chosen as the electron donor because it absorbs light with wavelengths up to ~850 nm (Figure 6.13) so any plasmon enhanced absorption at low frequencies will be maximised. The *JV* characteristics for these devices are shown in Figure 6.16. The diagram on the right of Figure 6.16 depicts how the intensity of trapped light (and thus optical field) decays exponentially into the photoactive layer. Device data for the devices shown in Figure 6.16 is shown below in Table 6.3.

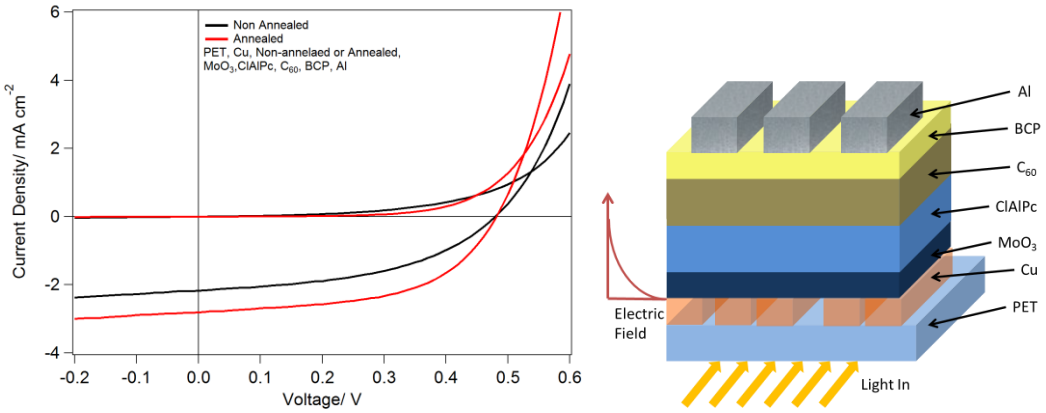

Figure 6.16: Left: Representative *JV* characteristics of OPV cells with the structure PET | Cu 8 nm | MoO_3 5 nm | ClAlPc 20 nm | C_{60} 40 nm | BCP 8 nm | Al 90 nm with (red) and without (black) annealing of the Cu electrode. Right: Schematic of the structure of the device showing the decay of the optical field intensity.

	J_{sc} / mA cm^{-2} ±1 SD	V_{oc} / V ±1 SD	*FF* ±1 SD	*PCE* ±1 SD
Non-annealed	2.3 ± 0.1	0.33 ± 0.09	0.39 ± 0.04	0.3 ± 0.1
Annealed	2.6 ± 0.1	0.45 ± 0.05	0.51 ± 0.05	0.6 ± 0.1

Table 6.3: *JV* data of OPV cells with the structure PET | Cu 8 nm | MoO_3 5 nm | ClAlPc 20 nm | C_{60} 40 nm | BCP 8 nm | Al 90 nm with and without annealing of the Cu electrode.

Table 6.3 shows a lower V_{oc} than is normally observed for the ClAlPc/C_{60} system which can be rationalised in terms of diffusion of Cu into the MoO_3 interlayer where it acts as an *n*-type dopant, thus reducing its work function and lowering the built in field in the device.[86] The figure also shows that the devices fabricated on electrodes with apertures generate a higher J_{sc} despite the lower transparency of the window electrode as was observed for OPVs using a CuPc donor layer without a hole extraction layer. The EQE spectra for devices using a ClAlPc donor layer are given in Figure 6.17.

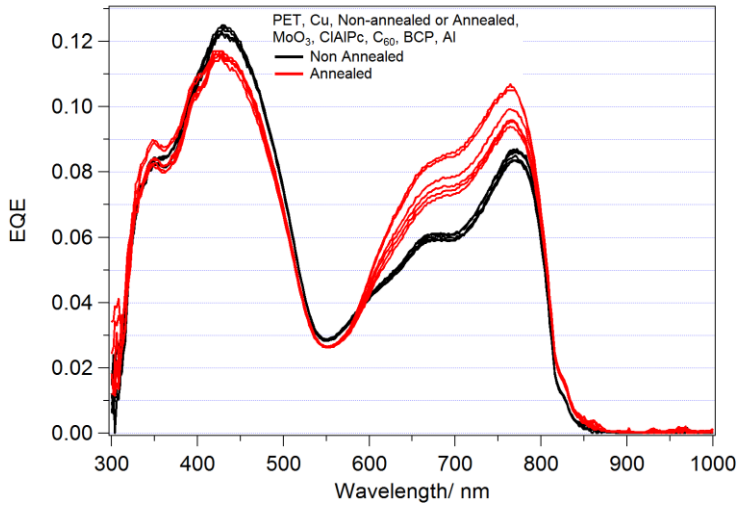

Figure 6.17: EQE spectra of OPV cells with the structure PET | Cu 8 nm | MoO_3 5 nm | ClAlPc 20 nm | C_{60} 40 nm | BCP 8 nm | Al 90 nm with (red) and without (black) annealing of the Cu electrode. All data sets are shown to demonstrate the reproducibility of the effect.

An increase in the spectral response beyond ~600 nm is observed for devices using electrodes with apertures, which corresponds to where the ClAlPc absorbs most strongly (Figure 1.13). As observed with devices using CuPc as the donor layer, this is the reason why OPV devices fabricated on electrodes with apertures generate more photocurrent. Notably, the EQE in the 400-600 nm wavelength region is not significantly lower for devices using an electrode with apertures, as would be expected considering the decrease in transparency upon annealing. This may be explained by light scattering by the flower-like copper oxide particles, particularly at short wavelengths giving rise to increase absorption at those wavelengths. To investigate this possibility, scattering spectra were collected using a dark field microscope (Figure 6.18). Unfortunately the light source did not extend below 450 nm or above 700 nm.

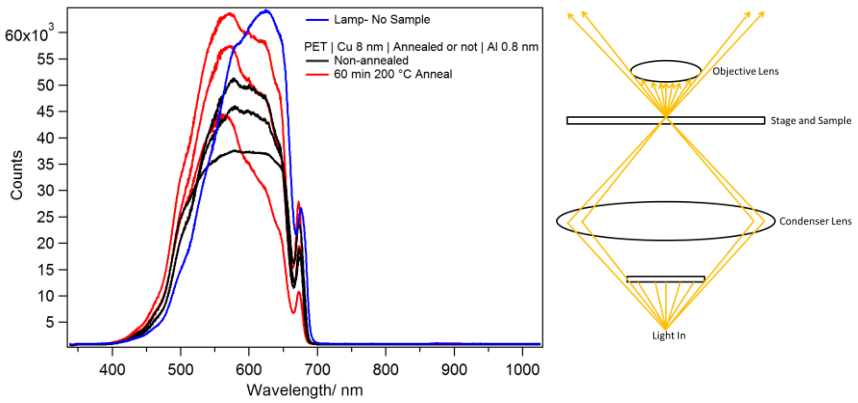

Figure 6.18: Left: Dark field microscope scattering spectra of PET | Cu 8 nm | Al 0.8 nm films. Films that were annealed at 200 °C for 60 minutes are shown in red, with reference films shown in black and the reference spectra of the lamp with no film shown in blue. Right: Schematic of operation of the dark field microscope.

Figure 6.18 shows that the annealed films scatter more light at short wavelengths than non-annealed films, thus explaining the similar performance in the 400-600 nm wavelength region of the EQE spectra in Figure 6.17. However, light scattering by the large flower-like structures does not explain the increase in spectral response for longer wavelengths of light, because there is no evidence for light scattering for wavelengths > 600 nm. The reason for higher photocurrent in devices fabricated on electrodes with apertures is therefore attributed primarily to a plasmon enhanced light absorption in the donor layer.

The data in Figures 6.19 and 6.20, and in Table 6.4 show that the plasmon enhancement of photocurrent shown in Figure 6.14 is also achieved when a Cu | Al (0.8 nm) electrode is used. Figure 6.19 and Table 6.4 show the typical *JV* response of OPV devices using a Cu | Al electrodes with and without apertures and Figure 6.20 shows the EQE spectra for these devices. This Al layer was used to hinder oxidation of the Cu

electrode and was deposited after annealing. Importantly, the ultra-thin Al layer does not suppress the plasmon enhancement in the ClAlPc/C_{60} system despite the SPR frequency of Al being in the UV range, which indicates that it is almost fully oxidised. This is not however unsurprising due to its very low thickness and very high reactivity towards O_2, which is present at a level of up to 5 ppm in the glove box. If the layer was thicker, then it would be expected to have an adverse effect on device performance, as Al layers have previously been utilised as plasmon frequency conversion layers to suppress plasmon enhanced absorption in ultra-thin Ag films.[87]

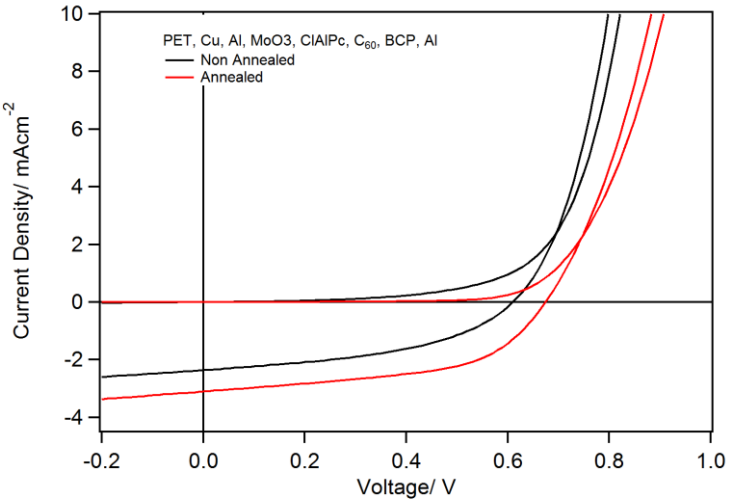

Figure 6.19: Typical *JV* plots of PET | Cu 8 nm | Al 0.8 nm | MoO_3 5 nm | ClAlPc 20 nm | C_{60} 40 nm | BCP 8 nm | Al 90 nm devices with (red) and without (black) annealing of the Cu electrode.

	J_{sc} / mA cm^{-2} ±1 SD	V_{oc} / V ±1 SD	*FF* ±1 SD	*PCE* ±1 SD
Cu | Al Non-annealed	2.3 ± 0.3	0.51 ± 0.2	0.41 ± 0.06	0.5 ± 0.2
Cu | Al Annealed	2.8 ± 0.2	0.66 ± 0.03	0.51 ± 0.05	1.0 ± 0.1

Table 6.4: Average J_{sc}, V_{oc}, *FF* and *PCE* values with standard deviations for PET | Cu 8 nm | Al 0.8 nm | MoO_3 5 nm | ClAlPc 20 nm | C_{60} 40 nm | BCP 8 nm | Al 90 nm devices with and without annealing of the Cu electrode.

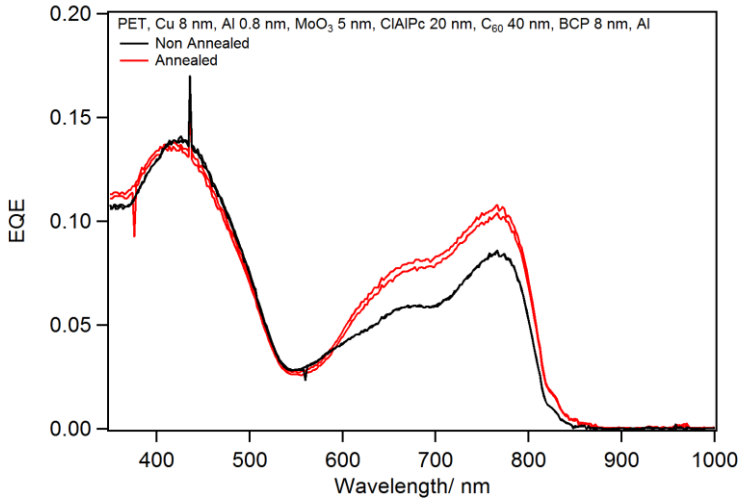

Figure 6.20: EQE spectra of OPVs fabricated on Cu | Al electrodes. Full device structures are: PET | Cu 8 nm | Al 0.8 nm | MoO_3 5 nm | ClAlPc 20 nm | C_{60} 40 nm | BCP 8 nm | Al 90 nm with (red) and without (black) annealing of the Cu electrode.

Figure 6.19 shows that OPV devices fabricated on electrodes with apertures exhibit increased J_{sc}, V_{oc} and *FF* as compared to those without. The increase in J_{sc} can be attributed to a plasmon enhanced light absorption in the ClAlPc layer (Figure 6.20) combined with light scattering, however this does not account for the increase in V_{oc}. It is possible that the improvement in V_{oc} is due to geometric electric field enhancement

resulting from the increase in electrode roughness upon annealing.[240] This effect can also give rise to increased J_{sc} in OPVs, although is wavelength independent and thus cannot account for the change in shape of the EQE spectra.

The microcavity effects demonstrated previously in Chapter 4 rely on the reflection of light from the opaque contact in the OPV device. To investigate the extent to which this effect is important in the current context, the opaque Al electrode was substituted with Ag. Figure 6.21 and Table 6.5 show the *JV* response for these OPVs.

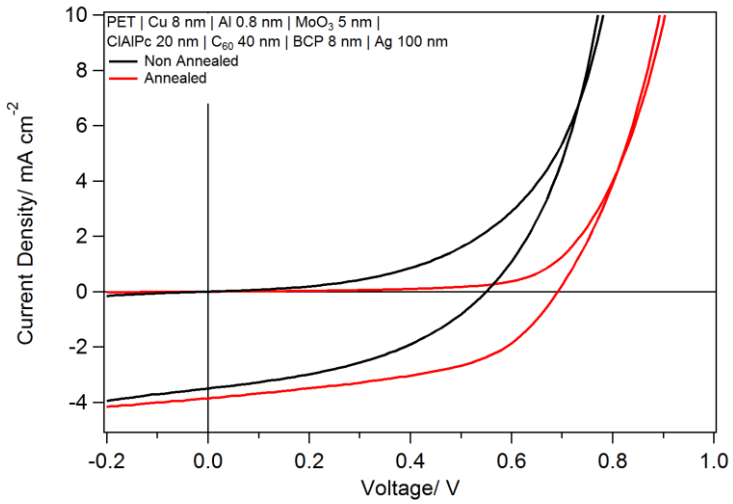

Figure 6.21: *JV* characteristics for OPVs with the structure: PET | Cu 8 nm | Al 0.8 nm | MoO_3 5 nm | ClAlPc 20 nm | C_{60} 40 nm | BCP 8 nm | Ag 100 nm with (red) and without (black) annealing of the Cu electrode.

	J_{sc}/ mA cm^{-2} ±1 SD	V_{oc}/ V ±1 SD	*FF* ±1 SD	*PCE* ±1 SD
Non-annealed	3.0 ± 0.3	0.3 ± 0.2	0.33 ± 0.05	0.3 ± 0.2
Annealed	3.3 ± 0.3	0.6 ± 0.1	0.47 ± 0.05	0.9 ± 0.3

Table 6.5: J_{sc}, V_{oc}, *FF* and *PCE* values with standard deviations for PET | Cu 8 nm | Al 0.8 nm | MoO_3 5 nm | ClAlPc 20 nm | C_{60} 40 nm | BCP 8 nm | Ag 100 nm devices with (red) and without (black) annealing of the Cu electrode.

Figure 6.22 shows the EQE spectra for the cells shown in Figure 6.21.

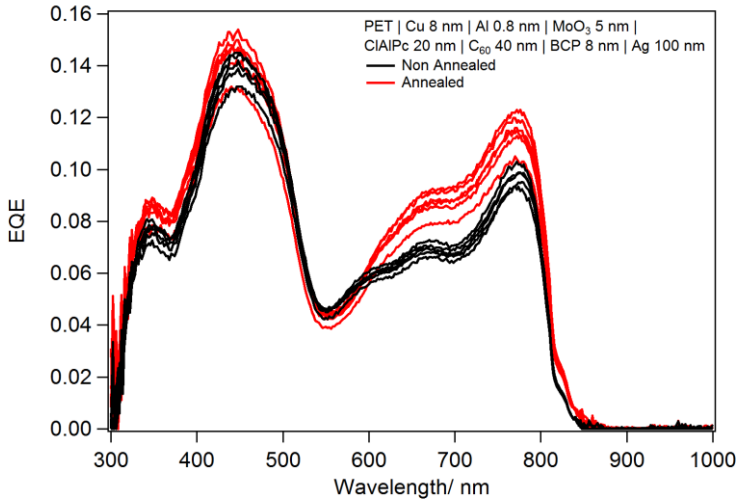

Figure 6.22: EQE spectra for PET | Cu 8 nm | Al 0.8 nm | MoO_3 5 nm | ClAlPc 20 nm | C_{60} 40 nm | BCP 8 nm | Ag 100 nm devices with (red) and without (black) annealing of the Cu electrode. All data sets are shown to demonstrate the reproducibility of the effect.

Figure 6.22 shows that the devices fabricated on electrodes with apertures generated more photocurrent in the ClAlPc region (600-850 nm), which is spatially close to the window electrode and there is no significant enhancement in current generation in the C_{60} region. This result is essentially the same as that observed for OPVs using an Al

electrode and is consistent with plasmon enhanced light absorption in the ClAlPc layer. However, a reduction in photocurrent in the C_{60} region would be expected due to a lower transparency in devices fabricated on electrodes with apertures. Again, this is not the case, consistent with light scattering by the flower like structures at short wavelengths. It is also possible that there is some enhancement in the C_{60} region, as the ClAlPc layer is only 20 nm thick, and there may be some shadowing effects present when evaporating onto the large structures seen in Figure 6.9. The devices illustrated in Figure 6.21 and Table 6.5 preformed relatively poorly, with the only difference between the structures being substitution of the opaque electrode material. A difference in the magnitude of J_{sc} was expected when replacing Al with Ag because the reflectivity of Ag is 5-15% higher across most of the region as shown in Figure 6.23. However, further investigations would be required to ascertain the reason for the poor V_{oc} and *FF* in the devices using electrodes without apertures.

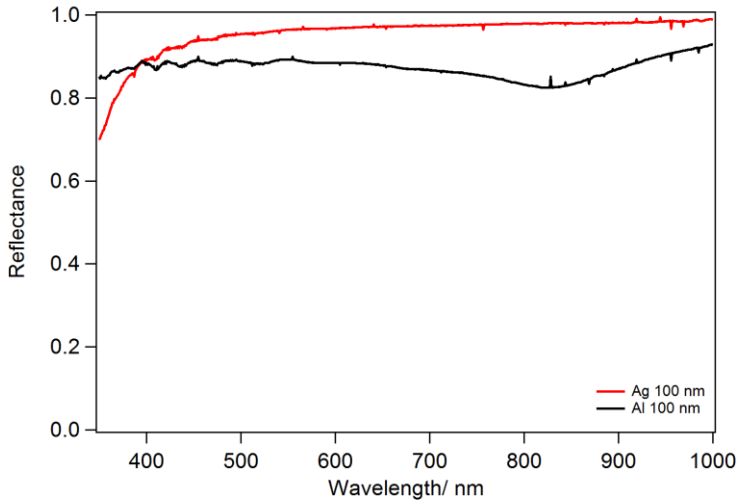

Figure 6.23: Reflectance of Ag 100 nm (red) and Al 100 nm (black) films at an angle of incidence of 39.5°.

In addition to Cu and Cu | Al films, Cu | Ag films were investigated as possible plasmon-active window electrodes. As the SPR frequency of Ag is higher frequency than Cu,[87] the onset of plasmon enhanced absorption would be expected to begin at shorter wavelengths, yielding enhanced performance increases. The use of this Ag layer does however incur extra materials expense and the electrode is more complex to fabricate. Similar morphologies to the Cu films with apertures were achieved in Cu | Ag films via annealing, as shown in Figure 6.24.

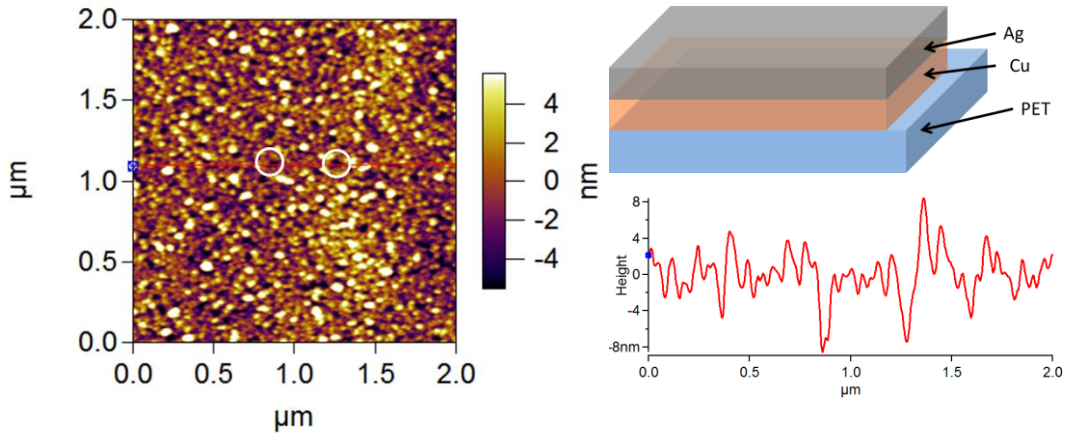

Figure 6.24: AFM morphology of a Cu 4 nm | Ag 4 nm film on PET with no UV/O_3, that has been annealed. Annealing was carried out after deposition of both layers. The roughness is 2.8 nm. A cross section graph is shown on the bottom right with a schematic of the electrode shown in the top right. The red line on the left scans show the lines where the cross sections were taken, and which apertures in dissects in the bottom scan. White circles illustrate two possible aperture sites on the AFM image.

The change in transparency upon annealing Cu | Ag films, along with the sheet resistance of these films is given in Figure 6.25. In this case the sheet resistance decreases with annealing.

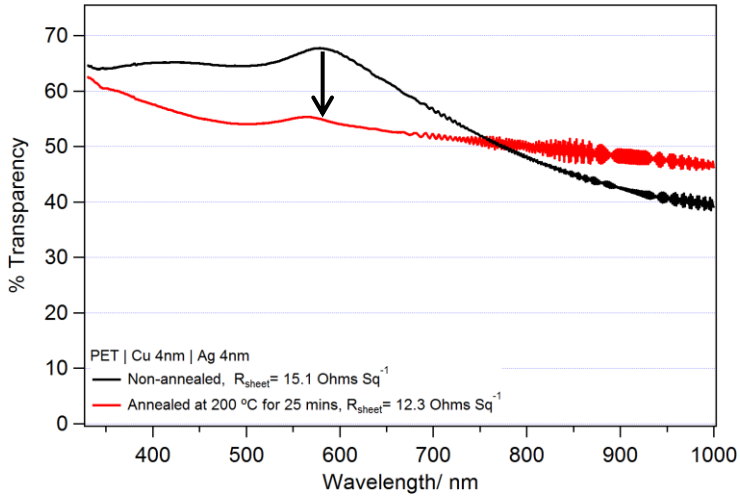

Figure 6.25: Transparency of PET | Cu 4 nm | Ag 4 nm films with and without annealing. Non-annealed and annealed films are shown in black and red respectively. Sheet resistance values for individual films are also stated.

The Cu | Ag films have favourable characteristics, with high transparency and low sheet resistance. As the Cu 4 nm | Ag 4 nm films yielded promising results, Cu 5 nm | Ag 3 nm were also investigated, to try to reduce the reliance on Ag. Figure 6.26 illustrates the transparency of Cu 5 nm | Ag 3 nm films on PET before and after annealing. The transparency of these films is decreased upon annealing as observed previously for the Cu | Al films. Figure 6.12 illustrates that the observed changes in transparency are due to morphological differences observed in the metal films and not the PET substrate.

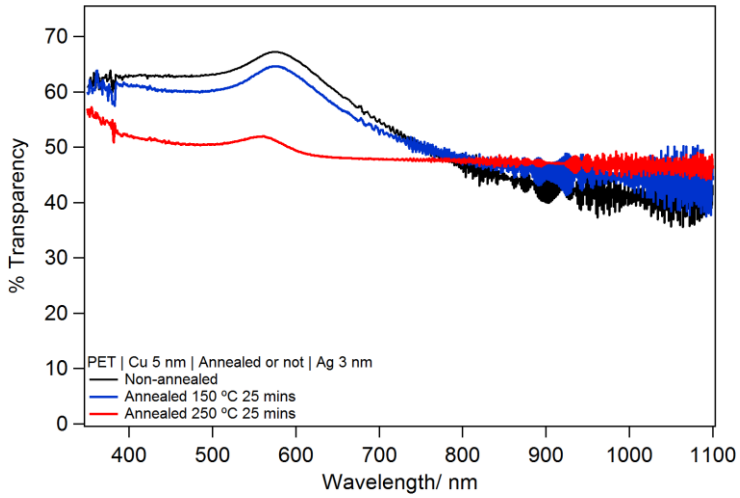

Figure 6.26: Transparency of Cu 5 nm | Ag 3 nm films on PET without annealing, with annealing at 150 °C for 25 minutes and with annealing at 250 °C for 25 minutes are shown in black, blue and red respectively.

Figure 6.27 shows the *JV* response from OPVs with Cu | Ag electrodes. The devices fabricated on Cu | Ag electrodes with apertures yield marginally enhanced performance, with increases in J_{sc}, V_{oc} and *FF*, resulting in a higher *PCE*. Table 6.6 shows OPV performance characteristics devices using Cu | Ag electrodes with and without apertures and a conventional ClAlPc/C_{60} architecture. Figure 6.28 shows the EQE spectra for the devices shown in Figure 6.27.

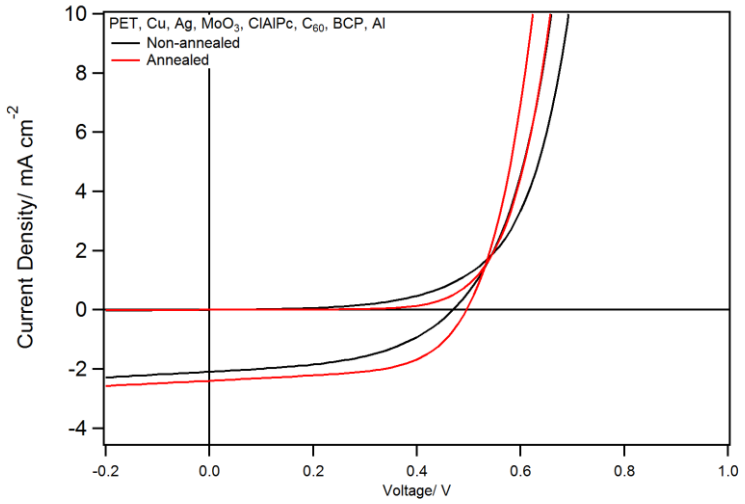

Figure 6.27: Typical *JV* plots of PET | Cu 5 nm | Ag 3 nm | MoO_3 5 nm | ClAlPc 20 nm | C_{60} 40 nm | BCP 8 nm | Al 90 nm devices with (red) and without (black) annealing of the Cu electrode. Annealing under nitrogen was carried out after Cu deposition and before Ag deposition.

	J_{sc} / mA cm^{-2} ±1 SD	V_{oc} / V ±1 SD	*FF* ±1 SD	*PCE* ±1 SD
Cu | Ag Non-annealed	2.2 ± 0.2	0.43 ± 0.04	0.46 ± 0.02	0.44 ± 0.08
Cu | Ag Annealed	2.5 ± 0.2	0.5 ± 0.1	0.49 ± 0.09	0.7 ± 0.2

Table 6.6: J_{sc}, V_{oc}, *FF* and *PCE* values with standard deviations for PET | Cu 5 nm | Ag 3 nm | MoO_3 5 nm | ClAlPc 20 nm | C_{60} 40 nm | BCP 8 nm | Al 90 nm devices. Annealing was carried out after Cu deposition and before Ag deposition.

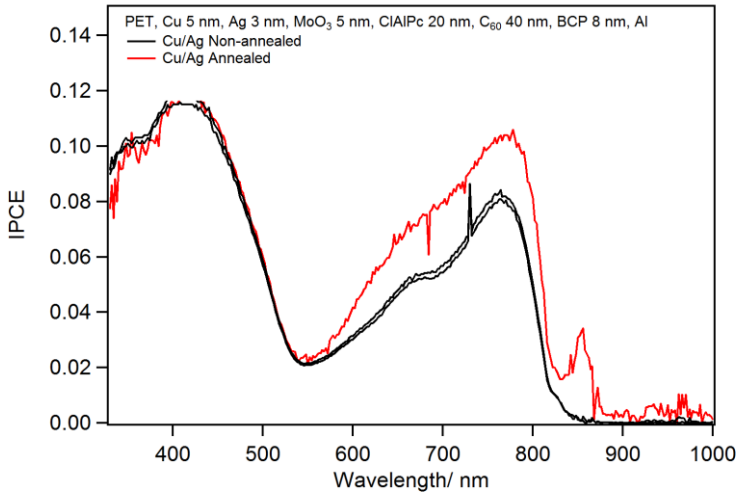

Figure 6.28: EQE spectra of PET | Cu 5 nm | Ag 3 nm | MoO_3 5 nm | ClAlPc 20 nm | C_{60} 40 nm | BCP 8 nm | Al 90 nm OPV devices with (red) and without (black) annealing of the Cu electrode.

Figure 6.28 is consistent with plasmon enhanced absorption in the ClAlPc layer and some scattering in the devices fabricated on electrodes with apertures. There is some evidence that the onset of plasmon enhanced absorption has been shifted to lower wavelength in Figure 6.28. In OPV devices based on Cu electrodes (Figures 6.17, 6.20 and 6.22), the onset of increased EQE occurs at ~600 nm, and in Figure 6.28 where a Cu | Ag electrode is used the onset occurs at ~550 nm, consistent with the higher SPR frequency of Ag.[87]

To test the generality of this result, OPV devices were fabricated with a PCDTBT/PC_{70}BM BHJ architecture. The PCDTBT/PC_{70}BM system was chosen due to its broad response over a large wavelength range. The champion *JV* characteristics and EQE data of these cells fabricated on Cu | Ag electrodes is shown in Figures 6.29 and 6.30 respectively. The *JV* data of the cells shown in Figure 6.29 is summarised in Table 6.7.

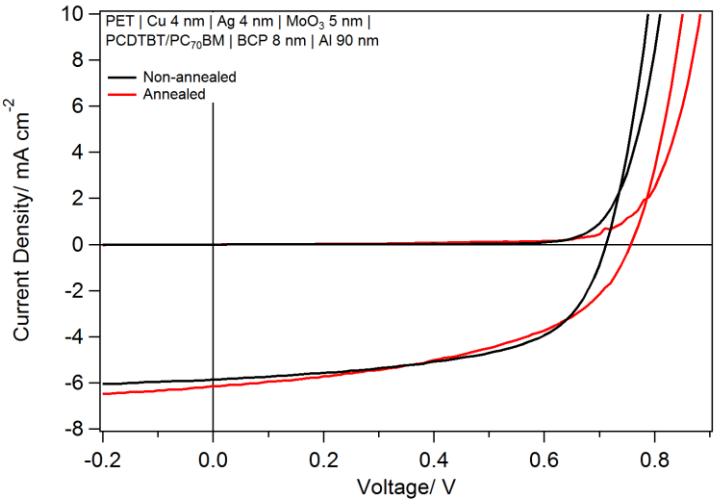

Figure 6.29: Champion *JV* data for OPV cells with the structure: PET | Cu 4 nm | Ag 4 nm | MoO_3 5 nm | PCDTBT/$PC_{70}BM$ | BCP 8 nm | Al 90 nm with (red) and without (black) annealing of the Cu electrode.

	J_{sc}/ mA cm^{-2} ±1 SD	V_{oc}/ V ±1 SD	*FF* ±1 SD	*PCE* ±1 SD
Cu | Ag Non-annealed	4.2 ± 0.6	0.70 ± 0.01	0.52 ± 0.06	1.5 ± 0.3
Cu | Ag Annealed	4.2 ± 0.5	0.75 ± 0.01	0.52 ± 0.02	1.6 ± 0.1

Table 6.7: J_{sc}, V_{oc}, *FF* and *PCE* averages with standard deviations for PET | Cu 4 nm | Ag 4 nm | MoO_3 5 nm | PCDTBT/$PC_{70}BM$ | BCP 8 nm | Al 90 nm devices with and without annealing of the Cu electrode.

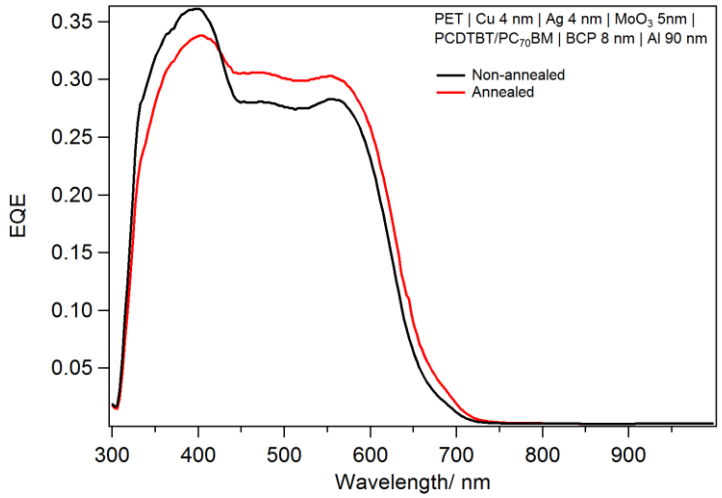

Figure 6.30: EQE spectra for the champion OPVs with the structure: PET | Cu 4 nm | Ag 4 nm | MoO_3 5 nm | PCDTBT/$PC_{70}BM$ | BCP 8 nm | Al 90 nm with (red) and without (black) annealing of the Cu electrode.

A large increase in EQE response in the high wavelength region, as seen for ClAlPc/C_{60} based OPVs, is not observed in Figure 6.30. The EQE spectra for these cells are more variable due to the active layer being solution processed, *in-contra* to the evaporated bilayer devices where a higher degree of accuracy and consistency with respect to layer thickness is achievable. As Table 6.7 shows, the spread of the *JV* data is too large to draw reliable conclusions about the impact of annealing. This is due to the higher degree of variability in polymer film thickness, leading to large variations in device performance. However, a decrease in the J_{sc} would be expected for devices using an electrode with apertures if plasmon enhanced light absorption did not occur, since the transparency of the electrode with apertures is greatly reduced as compared to that without. This indicates a plasmonic effect is still occurring, consistent with the EQE spectra. However, the large copper oxide flower-like structures mean that it is not

possible to draw firm conclusions, as these structures will affect the film crystallinity and thickness in addition to generating some scattering in the devices.

Finally, the sheet resistance of the Cu | Al films investigated for plasmonic properties was recorded in air and the results are summarised in Figure 6.31.

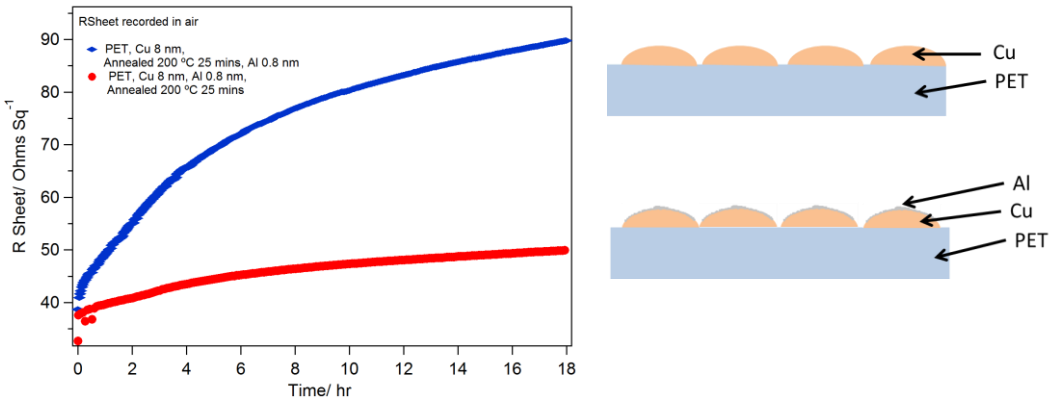

Figure 6.31: Sheet resistance with time (left) in air for a PET | Cu 8 nm | Al 0.8 nm films with annealing before (blue diamonds) and after (red circles) Al deposition. Schematic of Al on Cu (right) showing incomplete coverage.

Figure 6.31 shows that the annealed films are not air stable, even with the top Al layer. Annealing prior to deposition of the Al leads to larger increases in the sheet resistance upon air exposure compared to annealing after deposition of both layers. Unfortunately however, even the initial sheet resistance values shown here are too high to use in scalable OPV. Due to the less continuous nature of these films, the Al layer may not cover the Cu completely as shown on the right of Figure 6.31. A slightly thicker Al layer may be enough to render them air stable, although this is likely to hinder the observed plasmonic effect.[87] Obtaining surface passivation of plasmon active ultra-thin Cu electrodes is therefore very taxing.

6.5 Conclusions

Plasmon active Cu, Cu | Al, and Cu | Ag electrodes have been fabricated and incorporated into bilayer and BHJ OPVs. The fabricated OPV cells on Cu, Cu | Al and Cu | Ag electrodes exhibit increased performance on electrode annealing in CuPc/C_{60} and ClAlPc/C_{60} bilayer devices. This increase in performance is mainly due to an increased photocurrent. The enhancement in device performance is not due to a greatly altered sheet resistance or a higher transparency. In fact, the transparency is significantly lower. EQE spectra show that this increase in photocurrent originates from the ClAlPc/CuPc layer, which is spatially close to the window electrode, and this constitutes clear evidence to show that these electrodes are plasmon active. Improvements in the lower wavelength region of the EQE spectra vary, consistent with the presence of some scattering. Geometric electric field enhancement may be contributing to the increased *PCE*, but this effect is wavelength independent and cannot account for the enhancement in EQE spectra. The observed enhancements in bilayer devices were not observed reliably for polymeric systems and a large change in the shape of the EQE spectra at high wavelength was not observed. Clear determination of plasmon enhanced light absorption is hindered in these systems by higher variability of the EQE spectra due to larger variations in film thickness and morphology. However if a strong plasmonic enhancement was present in these systems, analogous to the bilayer devices, then it would still be detectable.

7. Conclusions and Future Work

This thesis has described progress towards development of Cu based window electrodes for application in OPVs. Chapter 3 described the fabrication of ultra-thin Cu films on glass using a mixed SAM and their passivation towards oxidation in air using an ultra-thin Al layer. This electrode simultaneously removes the requirement for a conducting oxide window electrode and a reactive low work function metal electrode such as Ca. Evidence that these electrodes can scavenge oxygen/water that permeates into the photoactive layer, without any change in surface roughness or an increase in the electrode's sheet resistance is presented. It is shown that upon oxidation the sheet resistance of this electrode actually decreases by up to ~15%, an effect that is attributed to room temperature de-alloying. Crucially, the evolution of the electrode work function upon *in-situ* oxidation of the electrode surface does not adversely impact the process of electron-extraction to the external circuit. The oxygen desiccant property of this electrode is particularly important for OPVs, since organic semiconductors are particularly susceptible to damage by low levels of molecular oxygen and the desiccant layer is in direct contact with the organic semiconductor. The disadvantage of this window electrode is the low far-field transparency compared to the industry standard of ITO. The key areas for further investigation on this electrode are: (i) a more comprehensive study of the desiccant properties of this electrode; specifically device lifetime studies in N_2 with controlled amounts of O_2 and H_20 separately introduced to determine how the electrode responds to these different oxidants. (ii) Experiments to understand the reason for the decrease in reverse saturation current upon oxidation of the electrode surface, specifically aimed at decoupling the change in work function and the change in oxide layer thickness.

Chapter 4 described a window electrode fabricated by sequential deposition of Cu and WO_{3-x} onto a SAM modified glass substrate. This electrode addresses the issue of the lower transparency of the electrode presented in Chapter 3, as the electrode has excellent far-field transparency over a broad range of wavelengths combined with a low reflectivity over a range of angles of incidence. The exceptional properties of this electrode result from rapid diffusion of Cu into the oxide overlayer at room temperature which renders the oxide layer highly electrically conductive towards the transport of electrons. This electrode performs well with WO_{3-x} layers up to 20 nm in thickness. As the window electrode in efficient OPVs this electrode is shown to perform as well as ITO glass. Future work for this chapter could concentrate on the extent to which the properties of the electrode depend on the WO_{3-x} deposition conditions, e.g. the amount of source preheating, evaporation rate and deposition method (i.e. by vacuum evaporation or spin coating from an organic metallic precursor). The upper thickness limit of the Cu doped WO_{3-x} layer could also be investigated as an optical spacer layer.

Chapter 5 describes attempts to integrate the approaches described in Chapters 3 & 4, including partial substitution of Cu with Ag which is less susceptible to oxidation. Cu | Al | WO_{3-x} electrodes are shown to retain many of the advantages of the electrode presented in Chapter 4 such as a low cost, high transparency, low sheet resistance, and efficient OPV device characteristics which are comparable to that of devices fabricated on ITO. This electrode also has the advantage of air stability, which has been achieved through the use of an oxidised Al layer inserted between the Cu and WO_{3-x} layers. The disadvantage of the electrode is the extra complexity and the cost incurred in the additional layer. Cu | Ag | WO_{3-x} electrodes were also investigated, and are very promising, with higher transparency up to 600 nm than the Cu | WO_{3-x} films presented in

Chapter 4. This coupled with low sheet resistance, ability to be rendered air stable and high thermal stability is promising for further work on the Cu | Ag electrode system. Further work on this chapter would involve studying the evolution of transparency of Glass | Cu | Al | WO_{3-x} electrodes with oxidation, which most likely results from an increase in refractive index, a demonstration of the Glass | Cu | Ag | Al electrode functioning in a high performance OPV system and a comparison with ITO glass would also be a promising area for further study.

Chapter 6 described the fabrication, characterisation and incorporation into OPVs of Cu, Cu | Al, and Cu | Ag electrodes with a dense array of sub-optical wavelength apertures supported on PET. Small molecule OPVs on Cu, Cu | Al and Cu | Ag electrodes with apertures exhibit greatly improved performance compared to identical devices fabricated on electrodes without apertures and with much greater far-field transparency. This increase in performance is mainly due to increased photocurrent over the part of the spectrum which the electrode with apertures is capable of supporting surface plasmon excitations. The results presented in Chapter 6 provide compelling evidence that a Cu electrode with a random array of sub-optical wavelength sized apertures support surface plasmon excitations which increase light absorption in the adjacent organic semiconductor in an OPV. Further work on this class of electrodes should include a more thorough look at scattering of light for the annealed and non-annealed electrodes, with and without the larger structures apparent on the electrode surface after annealing. OPVs could also be fabricated without these larger features to further simplify the electrode.

References

1. United Nations Department of Economic and Social Affairs/Population Division, World Population to 2300, **2004,** Page 145.

2. UK Renewable Energy Roadmap Update 2013, Department of Energy and Climate Change, URN: 13D/259, **2013**.

3. S. Chowdhury, U. Sumita, A. Islam, I. Bedja, *Energy Policy*, **2014**, *68*, 285.

4. C. Michaels, W. Spry, J. Hemingway, Energy Trends, Department of Energy and Climate Change, National Statistics, ISSN 2040-6029, **2014,** 4.

5. F. Manzano-Agugliaro, A. Alcayde, F.G. Montoya, A. Zapata-Sierra, C. Gil, *Renew. Sustain. Energy Rev.*, **2013**, *18*, 134–143.

6. J. Christians, R.C.M. Fung, P. V Kamat, *J. Am. Chem. Soc.*, **2014**, *136*, 758.

7. O. Inganäs, S. Admassie, *Adv. Mater.*, **2013**, *26*, 830.

8. M.A. Green, K. Emery, Y. Hishikawa, W. Warta, E.D. Dunlop, *Prog. Photovolt: Res. Appl.*, **2012**, *20*, 12.

9. R. M. Swanson, *Prog. Photovolt: Res. Appl.*, **2006**, 14, 443.

10. J.A. Chang, J.H. Rhee, S.H. Im, Y.H. Lee, H. Kim, S. Il Seok, M.K. Nazeeruddin, M. Gratzel, *Nano Lett.*, **2010**, *10*, 2609.

11. J. Weickert, R.B. Dunbar, H.C. Hesse, W. Wiedemann, L. Schmidt-Mende, *Adv. Mater.*, **2011**, *23*, 1810.

12. Y. Hirai, Y. Kurokawa, A. Yamada, *Jpn. J. Appl. Phys.*, **2014,** *53, 012301*.

13. O.E. Semonin, J.M. Luther, S. Choi, H.-Y. Chen, J. Gao, A.J. Nozik, M.C. Beard, *Science,* **2011**, *334*, 1530.

14. B. Ehrler, K.P. Musselman, M.L. Böhm, F.S.F. Morgenstern, Y. Vaynzof, B.J. Walker, J.L. Macmanus-Driscoll, N.C. Greenham, *ACS Nano*, **2013**, *7*, 4210.

15. H.J. Kim, V. Depauw, G. Agostinelli, G. Beaucarne, J. Poortmans, *Thin Solid Films*, **2006**, *411*, 511.

16. R. Søndergaard, M. Hösel, D. Angmo, T.T. Larsen-Olsen, F.C. Krebs, *Mater. Today,* **2012**, *15*, 36.

17. N. Espinosa , M. Hösel , D. Angmo , F. C. Krebs . *Energy Environ. Sci.*, **2012,** *5*, 5117.

18. F.C. Krebs, T. Tromholt, M. Jørgensen, *Nanoscale,* **2010**, *2*, 873.

19. C.J.M. Emmott, A. Urbina, J. Nelson, *Sol. Energy Mater. Sol. Cells.*, **2012**, *97*, 14.

20. B.H. Ishii, K. Sugiyama, E. Ito, K. Seki, *Adv. Mater.*, **1999**, *11*, 605.

21. Y. Sun, J.H. Seo, C.J. Takacs, J. Seifter, A.J. Heeger, *Adv. Mater.*, **2011**, *23*, 1679.

22. C.W. Tang, *Appl. Phys. Lett.*, **1986**, *48*, 183.

23. M.C. Scharber, N.S. Sariciftci, *Prog. Polym. Sci.*, **2013**, *38*, 1929.

24. L. Dou, J. You, Z. Hong, Z. Xu, G. Li, R. Street, Y. Yang, *Adv. Mater.*, **2013**, *46*, 6642.

25. A.J. Medford, M.R. Lilliedal, M. Jørgensen, D. Aarø, H. Pakalski, J. Fyenbo, F.C. Krebs, *Opt. Express,* **2010**, *18*, A272.

26. N. Grossiord, J.M. Kroon, R. Andriessen, P.W.M. Blom, *Org. Electron.*, **2012**, *13*, 432.

27. A. Cravino, P. Schilinsky, C.J. Brabec, *Adv. Funct. Mater.*, **2007**, *17*, 3906.

28. R. García-Valverde, J. Cherni, A. Urbina, *Prog. Photovoltaics Res. Appl.*, **2010**, *18*, 535.

29. F.C. Krebs, N. Espinosa, M. Hösel, R.R. Søndergaard, M. Jørgensen, *Adv. Mater.*, **2013**, *26*, 29.

30. L. Dou, J. You, J. Yang, C. Chen, Y. He, S. Murase, T. Moriarty, K. Emery, G. Li, Y. Yang, *Nat. Photonics*, **2012**, *6*, 180.

31. C.A. Gueymard, D. Myers, K. Emery, *Solar Energy*, **2003**, *73*, 443.

32. M.N. Kozicki, C. Gopalan, M. Balakrishnan, M. Mitkova, *IEEE Trans. Nanotechnol.*, **2006**, *5*, 535.

33. H. Atwater, A. Polman, *Nat. Mater.*, **2010**, *9*, 205.

34. B. A. Collins, Z. Li, J.R. Tumbleston, E. Gann, C.R. McNeill, H. Ade, *Adv. Energy Mater.*, **2013**, *3*, 65.

35. Z. He, C. Zhong, S. Su, M. Xu, H. Wu, Y. Cao, *Nature Photon.*, **2012**, *6*, 591.

36. T.-H. Lai, S.-W. Tsang, J.R. Manders, S. Chen, F. So, *Mater. Today*, **2013**, *16*, 424.

37. A.L. Burin, M. Ratner, *J. Phys. Chem. A*, **2000**, *104*, 4704.

38. J. C. Bernède, Y. Berredjem, L. Cattin, M. Morsli, *App. Phys. Lett.*, **2008**, *92*, 083304.

39. Y. Zhou, C. Fuentes-Hernandez, J. Shim, J. Meyer, A.J. Giordano, H. Li, P. Winget, T. Papadopoulos, H. Cheun, J. Kim, M. Fenoll, A. Dindar, W. Haske, E. Najafabadi, T.M. Khan, H. Sojoudi, S. Barlow, S. Graham, J.-L. Brédas, S.R. Marder, A. Kahn, B. Kippelen, *Science*, **2012**, *336*, 327.

40. M.T. Greiner, Z.-H. Lu, *NPG Asia Mater.*, **2013**, *5*, e55.

41. A. Kumar, S. Sista, Y. Yang, *J. Appl. Phys.*, **2009**, *105*, 094512.

42. B.P. Rand, J. Li, J. Xue, R.J. Holmes, M.E. Thompson, S.R. Forrest, *Adv. Mater.*, **2005**, *17*, 2714.

43. M.Y. Chan, C.S. Lee, S.L. Lai, M.K. Fung, F.L. Wong, H.Y. Sun, K.M. Lau, S.T. Lee, *J. Appl. Phys.*, **2006**, *100*, 094506.

44. M.O. Reese, M.S. White, G. Rumbles, D.S. Ginley, S.E. Shaheen, *Appl. Phys. Lett.*, **2008**, *92*, 053307.

45. B. Ray, M.A. Alam, *IEEE J. Photovolt.*, **2012**, *3*, 310.

46. S. Choi, W.J. Potscavage, B. Kippelen, *J. Appl. Phys.*, **2009**, *106*, 054507.

47. M. Hermenau, S. Schubert, H. Klumbies, J. Fahlteich, L. Müller-Meskamp, K. Leo, M. Riede, *Sol. Energy Mater. Sol. Cells*, **2012**, *97*, 102.

48. S. Bertho, I. Haeldermans, A. Swinnen, W. Moons, T. Martens, L. Lutsen, D. Vanderzande, J. Manca, A. Senes, A. Bonfiglio, *Sol. Energy Mater. Sol. Cells*, **2007**, *91*, 385.

49. M. Hermenau, M. Riede, K. Leo, S. Gevorgyan, F.C. Krebs, K. Norrman, *Sol. Energy Mater. Sol. Cells*, **2011**, *95*, 1268.

50. B.M. Schaer, F. Nüesch, D. Berner, W. Leo, L. Zuppiroli, *Adv. Funct. Mater.*, **2001**, *11*, 116.

51. H.-H. Liao, C.-M. Yang, C.-C. Liu, S.-F. Horng, H.-F. Meng, J.-T. Shy, *J. Appl. Phys.*, **2008**, *103*, 104506.

52. K. Norrman, M. V Madsen, S. Gevorgyan, F.C. Krebs, *J. Am. Chem. Soc.*, **2010**, *132*, 16883.

53. E.D. Gomez, Y.-L. Loo, *J. Mater. Chem.*, **2010**, *20*, 6604.

54. R. Søndergaard, M. Helgesen, M. Jørgensen, F.C. Krebs, *Adv. Energy Mater.*, **2011**, *1*, 68.

55. C.H. Peters, I.T. Sachs-Quintana, J.P. Kastrop, S. Beaupré, M. Leclerc, M.D. McGehee, *Adv. Energy Mater.*, **2011**, *1*, 491.

56. M.T. Lloyd, D.C. Olson, P. Lu, E. Fang, D.L. Moore, M.S. White, M.O. Reese, D.S. Ginley, J.W.P. Hsu, *J. Mater. Chem.*, **2009**, *19*, 7638.

57. D.S. Hecht, R.B. Kaner, *MRS Bull.*, **2011**, *36*, 749.

58. T.P. Osedach, T.L. Andrew, V. Bulović, *Energy Environ. Sci.*, **2013**, *6*, 711.

59. N. Formica, D. Sundar Ghosh, T.L. Chen, C. Eickhoff, I. Bruder, V. Pruneri, *Sol. Energy Mater. Sol. Cells*, **2012**, *107*, 63.

60. Y. Liang, L. Yu, *Accounts Chem. Res.*, **2010**, *43*, 1227.

61. W. Li, L. Yang, J.R. Tumbleston, L. Yan, H. Ade, W. You, *Adv. Mater.*, **2014**, *26*, 4456.

62. J.M. Szarko, J. Guo, Y. Liang, B. Lee, B.S. Rolczynski, J. Strzalka, T. Xu, S. Loser, T.J. Marks, L. Yu, L.X. Chen, *Adv. Mater.*, **2010**, *22*, 5468.

63. Z. He, C. Zhong, X. Huang, W.-Y. Wong, H. Wu, L. Chen, S. Su, Y. Cao, *Adv. Mater.*, **2011**, *23*, 4636.

64. T. Chu, J. Lu, S. Beaupr, Y. Zhang, *J. Am. Chem. Soc.*, **2011**, *133*, 4250.

65. P. A. Cox, D. Waldow, T.J. Dupper, S. Jesse, D.S. Ginger, *ACS Nano,* **2013,** *7*, 10405.

66. Y.W. Soon, H. Cho, J. Low, H. Bronstein, I. McCulloch, J.R. Durrant, *Chem. Commun. (Camb).*, **2013**, *49*, 1291.

67. T.T. Larsen-Olsen, E. Bundgaard, K.O. Sylvester-Hvid, F.C. Krebs, *Org. Electron.*, **2011**, *12*, 364.

68. S. Kouijzer, S. Esiner, C.H. Frijters, M. Turbiez, M.M. Wienk, R. J. Janssen, *Adv. Energy Mater.*, **2012**, *2*, 945.

69. L-J. Pegg, *Controlling Hole Extraction in Organic Photovoltaics*, PhD thesis, University of Warwick, **2012**

70. Z. Li, H.C. Wong, Z. Huang, H. Zhong, C.H. Tan, W.C. Tsoi, J.S. Kim, J.R. Durrant, J.T. Cabral, *Nat. Commun.*, **2013**, *4*, 2227.

71. A. Ito, T. Morikawa, T. Takahashi, *Chem. Phys. Lett.*, **1993**, *211*, 333.

72. H.R. Barzegar, C. Larsen, L. Edman, T. Wågberg, *Part. Part. Syst. Charact.*, **2013,** *30*, 715.

73. X. Xi, W. Li, J. Wu, J. Ji, Z. Shi, G. Li, *Sol. Energy Mater. Sol. Cells*, **2010**, *94*, 2435.

74. L.M. Andersson, Y. Te Hsu, K. Vandewal, A.B. Sieval, M.R. Andersson, O. Inganäs, *Org. Electron. Physics, Mater. Appl.*, **2012**, *13*, 2856.

75. C.R. McNeill, N.C. Greenham, *Adv. Mater.*, **2009**, *21*, 3840.

76. J.-Y. Lee, S.T. Connor, Y. Cui, P. Peumans, *Nano Lett.*, **2008**, *8*, 689.

77. F. Yang, S.R. Forrest, *Adv. Mater.*, **2006**, *18*, 2018.

78. E.F. Fernández, P. Rodrigo, F. Almonacid, P. Pérez-Higueras, *Sol. Energy Mater. Sol. Cells*, **2014**, *124*, 159.

79. Y.-J. Noh, S.-S. Kim, T.-W. Kim, S.-I. Na, *Semicond. Sci. Technol.*, **2013**, *28*, 125008.

80. J.D. Servaites, S. Yeganeh, T.J. Marks, M. Ratner, *Adv. Funct. Mater.*, **2010**, *20*, 97.

81. M.G. Helander, Z.B. Wang, J. Qiu, M.T. Greiner, D.P. Puzzo, Z.W. Liu, Z.H. Lu, *Science*, **2011**, *332*, 944.

82. N.P. Sergeant, A. Hadipour, B. Niesen, D. Cheyns, P. Heremans, P. Peumans, B.P. Rand, *Adv. Mater.*, **2012**, *24*, 728.

83. K.-S. Lee, J.-W. Lim, H.-K. Kim, T.L. Alford, G.E. Jabbour, *Appl. Phys. Lett.*, **2012**, *100*, 213302.

84. U.S. Geological Survey, Mineral Commodity Summaries., 2014, p. 74, 48 and 146.

85. J. Zou, C.-Z. Li, C.-Y. Chang, H.-L. Yip, A.K.-Y. Jen, *Adv. Mater.*, **2014**, 1.

86. H.M. Stec, R.A. Hatton, *ACS Appl. Mater. Interfaces*, **2012**, *4*, 6013.

87. B. Koo, S. Kim, J.-L. Lee, *J. Mater. Chem. C*, **2013**, *1*, 246.

88. F.C. Krebs, K. Norrman, *Prog. Photovolt: Res. Appl.*, **2007,** 15, 697.

89. D.-J. Kwak, B.-H. Moon, D.-K. Lee, C.-S. Park, Y.-M. Sung, *J. Electr. Eng. Technol.,* **2011**, *6*, 684.

90. D. S. Hecht, L. Hu, G. Irvin, *Adv. Mater.,* **2011,** *23*, 1482.

91. Z. Liu, J. Li, F. Yan, *Adv. Mater.*, **2013**, *25*, 4296.

92. W. Zhang, B. Zhao, Z. He, X. Zhao, H. Wang, S. Yang, H. Wu, Y. Cao, *Energy Environ. Sci.,* **2013**, *6*, 1956.

93. A. R. Rathmell, S. M. Bergin, Y-L. Hua, Z-Y. Li, B. J. Wiley, *Adv. Mater.,* **2010,** *22*, 3558.

94. D.S. Ghosh, T.L. Chen, V. Mkhitaryan, N. Formica, V. Pruneri, *Appl. Phys. Lett.,* **2013**, *102*, 221111.

95. H. Wu, D. Kong, Z. Ruan, P.-C. Hsu, S. Wang, Z. Yu, T.J. Carney, L. Hu, S. Fan, Y. Cui, *Nat. Nanotechnol.,* **2013**, *8*, 421.

96. F.C. Krebs, M. Hösel, M. Corazza, B. Roth, M. V. Madsen, S. Gevorgyan, R.R. Søndergaard, D. Karg, M. Jørgensen, *Energy Technol.,* **2013**, *1*, 378.

97. H.M. Stec, R.A. Hatton, *Adv. Energy Mater.,* **2012**, *3*, 193.

98. N. Formica, D.S. Ghosh, A. Carrilero, T.L. Chen, R.E. Simpson, V. Pruneri, *ACS Appl. Mater. Interfaces*, **2013**, *5*, 3048.

99. K. Hong, K. Kim, S. Kim, I. Lee, H. Cho, S. Yoo, H.W. Choi, N. Lee, Y. Tak, J. Lee, *J. Phys. Chem. C*, **2011**, *115*, 3453.

100. E. Itoh, Y. Higuchi, D. Furuhata, T. Shirotori, *Jpn. J. Appl. Phys.,* **2011**, *50*, 01BC14.

101. K. Zilberberg, J. Meyer, T. Riedl, *J. Mater. Chem. C*, **2013**, *1*, 4796.

102. M.T. Greiner, L. Chai, M.G. Helander, W.-M. Tang, Z.-H. Lu, *Adv. Funct. Mater.*, **2013**, *23*, 215.

103. K. Kanai, K. Koizumi, S. Ouchi, Y. Tsukamoto, K. Sakanoue, Y. Ouchi, K. Seki, *Org. Electron.*, **2010**, *11*, 188.

104. M.T. Greiner, M.G. Helander, W.-M. Tang, Z.-B. Wang, J. Qiu, Z.-H. Lu, *Nat. Mater.*, **2012**, *11*, 76.

105. N.N. Lal, H. Zhou, M. Hawkeye, J.K. Sinha, P.N. Bartlett, G. J. Amaratunga, J.J. Baumberg, *Phys. Rev. B*, **2012**, *85*, 245318.

106. K. Von Rottkay, M. Rubin, S. Wen, *Thin Solid Films*, **1997**, *306*, 10.

107. T. He, J. Yao, *J. Mater. Chem.*, **2007**, *17*, 4547.

108. J.C. Bernède, L. Cattin, T. Abachi, Y. Lare, M. Morsli, M. Makha, Mater. Lett., **2013,** *112*, 187.

109. H. Zheng, J.Z. Ou, M.S. Strano, R.B. Kaner, A. Mitchell, K. Kalantar-zadeh, *Adv. Funct. Mater.*, **2011**, *21*, 2175.

110. M. Gillet , K. Aguir , C. Lemire , E. Gillet , K. Schierbaum, *Thin Solid Films*, **2004,** *467*, 239.

111. J. Meyer, M. Kroger, S. Hamwi, F. Gnam, T. Riedl, W. Kowalsky, A. Kahn, *Appl. Phys. Lett.*, **2010**, *96*, 193302.

112. H. Demiryont, K.E. Nietering, *Appl. Opt.*, **1989**, *28*, 1494.

113. M. Kröger, S. Hamwi, J. Meyer, T. Riedl, W. Kowalsky, A. Kahn, *Appl. Phys. Lett.*, **2009**, *95*, 123301.

114. D. Cheyns, B. Kam, K. Vasseur, P. Heremans, B.P. Rand, *J. Appl. Phys.*, **2013**, *113*, 043109.

115. P.R. West, S. Ishii, G.V. Naik, N.K. Emani, V.M. Shalaev, A. Boltasseva, *Laser Photon. Rev.*, **2010**, *4*, 795.

116. T. Rindzevicius, Y. Alaverdyan, A. Dahlin, F. Höök, D.S. Sutherland, M. Käll, *Nano Lett.*, **2005**, *5*, 2335.

117. L.H. Smith, J.E. Wasey, I.D.W. Samuel, W.L. Barnes, *Adv. Funct. Mater.*, **2005**, *15*, 1839.

118. S.-W. Baek, J. Noh, C.-H. Lee, B. Kim, M.-K. Seo, J.-Y. Lee, *Sci. Rep.*, **2013**, *3*, 1726.

119. H.-A. Chen, J.-L. Long, Y.-H. Lin, C.-J. Weng, H.-N. Lin, *J. Appl. Phys.*, **2011**, *110*, 054302.

120. G.H. Chan, J. Zhao, E.M. Hicks, G.C. Schatz, R.P. Van Duyne, *Nano Lett.*, **2007**, *7*, 1947.

121. H. Shiba, M. Haraguchi, M. Fukui, *J. Phys. Soc. JPN.*, **1994,** 63, 1400.

122. B. Wu, T.Z. Oo, X. Li, X. Liu, X. Wu, E.K.L. Yeow, H.J. Fan, N. Mathews, T.C. Sum, *J. Phys. Chem. C*, **2012**, *116*, 14820.

123. T. Rindzevicius, Y. Alaverdyan, A. Dahlin, F. Höök, D.S. Sutherland, M. Käll, *Nano Lett.*, **2005**, *5*, 2335.

124. M.-G. Kang, T. Xu, H.J. Park, X. Luo, L.J. Guo, *Adv. Mater.*, **2010**, *22*, 4378.

125. B. Niesen, B.P. Rand, P. Van Dorpe, D. Cheyns, E. Fron, M. Van der Auweraer, P. Heremans, *J. Phys. Chem. C*, **2012**, *116*, 24215.

126. J. Szeremeta, M. Nyk, A. Chyla, W. Strek, M. Samoc, *Opt. Mater. (Amst).*, **2011**, *33*, 1372.

127. R.M. Cook, L. Pegg, S.L. Kinnear, O.S. Hutter, R.J.H. Morris, R.A. Hatton, *Adv. Energy Mater.*, **2011**, *1*, 440.

128. M. Aslam, G. Gopakumar, T. L. Shoba, I. S. Mulla, K. Vijayamohanan, S. K. Kulkarni, J. Urban, W. Vogel, *J. Colloid Interface Sci.,* **2002,** *255*, 79.

129. H. M. Stec, R. J. Williams, T. S. Jones, R. A. Hatton, *Adv. Funct. Mater.,* **2011,** *21*, 1709.

130. D.D. Gandhi, M. Lane, Y. Zhou, A.P. Singh, S. Nayak, U. Tisch, M. Eizenberg, G. Ramanath, *Nature*, **2007**, *447*, 299.

131. A. Inberg, E. Glickman, T. Asher, N. Fishelson, Y. Shacham-Diamand, *Surf. Coatings Technol.,* **2009**, *204*, 520.

132. T. Asher, A. Inberg, E. Glickman, N. Fishelson, Y. Shacham-Diamand, *Electrochim. Acta,* **2009**, *54*, 6053.

133. C. Kasl, M.J.R. Hoch, *Rev. Sci. Instrum.,* **2005**, *76*, 033907.

134. L.J. van der Pauw, *Philips Technical Review,* **1958,** *20*, 220

135. H.K. Raut, V.A. Ganesh, A.S. Nair, S. Ramakrishna, *Energy Environ. Sci.,* **2011**, *4*, 3779.

136. W.N. Hansen, G.J. Hansen, *Surf. Sci.,* **2001**, *481*, 172.

137. G. Binnig, C. F. Quate, C. Gerber, *Phys. Rev. Let.,* **1986**, *56,* 930.

138. B. Cappella, G. Dietler, *Surf. Sci. Rep.,* **1999**, *34*, 1.

139. E.J. Luber, J.M. Buriak, *ACS Nano*, **2013**, 7, 4708.

140. J. Kalowekamo, E. Baker, *Sol. Energy*, **2009,** *83,* 1224.

141. C. Niu, *MRS Bull.,* **2011,** *36,* 766.

142. M. O. Reese, A. J. Morfa, M. S. White, N. Kopidakis, S. E. Shaheen, G. Rumbles, D.S. Ginley, *Sol. Energy Mater. Sol. Cells,* **2008**, *92,* 746.

143. M. Jørgensen, K. Norrman, S. A. Gevorgyan, T. Tromholt, B. Andreasen, F. C. Krebs, *Adv. Mater.,* **2012,** *24,* 580.

144 . Y. Matsuo, A. Ozu, N. Obata, N. Fukuda, H. Tanaka, E. Nakamura, *Chem. Commun.,* **2012**, *48,* 3878.

145 . C. H. Peters, I. T. Sachs-Quintana, W. R. Mateker, T. Heumueller, J. Rivnay, R. Noriega, Z. M. Beiley, E. T. Hoke, A. Salleo, M. D. McGehee, *Adv. Mater.,* **2012**, *24,* 663.

146. Y. Jin, J. Feng, X-L. Zhang, Y. Bi, Y. Bai, L. Chen, T. Lan, Y-F. Liu, Q-D. Chen, H-B. Sun, *Adv. Mater.,* **2012,** *24,* 1187.

147. B. O' Connor, C. Haughn, K. H. An, K. P. Pipe, M. Shtein, *Appl. Phys. Lett.,* **2008,** *93,* 223304.

148. G. H. Jung, K. Hong, W. J. Dong, S. Kim, J-L. Lee, *Adv. Energy Mater.,* **2011,** *1,* 1023.

149. L. Hu, H. Wu, Y. Cui, *MRS Bull.,* **2011,** *36,* 760.

150. D. S. Ghosh, R. Betancur, T. L. Chen, V. Pruneri, J. Martorell, *Sol. Energy Mater. Sol. Cells,* **2011,** *95,* 1228.

151. V. J. Logeeswaran, N. P. Kobayashi, M. S. Islam, W. Wu, P. Chaturvedi, N. X. Fang, S. Y. Wang, R. S. Williams, *Nano Lett.*, **2009,** *9*, 178.

152. R. A. Hatton, M. R. Willis, M. A. Chesters, D. Briggs, *J. Mater. Chem.,* **2003,** *13,* 722.

153. L. Lange, Y. Wyser, *Packag. Technol. Sci.,* **2003,** *16,* 149.

154. A. R. Rathmell, B. J. Wiley, *Adv. Mater.,* **2011,** *23,* 4798.

155. D. Save, F. Braud, J. Torres, F. Binder, C. Muller, J. O. Weidner, W. Hasse, *Microelectron. Eng.,* **1997,** *33,* 75.

156. W. Li, D. Y. Li, *J. Chem. Phys.,* **2005,** *122,* 064708 and measured using the Kelvin probe.

157. S. Lim, D. Han, H. Kim, S. Lee, S. Yoo, *Sol. Energy Mater. Sol. Cells*, **2012,** *101,* 170.

158. W. Wang, W. A. Lanford, S. P. Murarka, *Appl. Phys. Lett.,* **1996,** *68,* 1622.

159. I. Pérez Lopéz, L. Cattin, D. T. Nguyen, M. Morsli, J. C. Bernède, *Thin Solid Films*, **2012**, *520,* 6419.

160. W. I. Jeong, J. Lee, S. Y. Park, J. W. Kang, J. J. Kim, *Adv. Funct. Mater.,* **2011,** *21,* 343.

161. A. Manor, E. A. Katz, T. Tromholt, B. Hirsch, F. C. Krebs, *J. App. Phys.,* **2011,** *109*, 074508.

162. C-H. Choi, K-Y. Nam, Z. Yu, R. W. Dutton, *IEEE Trans. Electron Devices,* **2001**, *48*, 2823.

163. W. M. Haynes, in *CRC Handbook of Chemistry and Physics 91st Edition*, CRC Press, **2010.**

164. M. Wang, F. Xie, J. Du, Q. Tang, S. Zheng, Q. Miao, J. Chen, N. Zhao, J. B. Xu, *Sol. Energy Mater. Sol. Cells*, **2011,** *95*, 3303.

165. B. Paci, A. Generosi, V. R. Albertini, P. Perfetti, R. de Bettignies, C. Sentein, *Chem. Phys. Lett.*, **2008,** *461*, 77.

166. E. Voroshazi, B. Verreet, A. Buri, R. Müller, D. D. Nuzzo, P. Heremans, *Org. Electron.*, **2011**, *5*, 736.

167. V. Bhosle, J. T. Prater, F. Yang, D. Burk, S. R. Forrest, J. Narayan, *J. App. Phys.*, **2007,** *102*, 023501.

168. G. Dennler, C. Lungenschmied, H. Neugebauer, N. S. Sariciftci, M. Latrèche, G. Czeremuszkin, M. R. Wertheimer, *Thin Solid Films*, **2006**, *349*, 511.

169. S. Cho, K. Lee, A.J. Heeger, *Adv. Mater.*, **2009**, *21*, 1941.

170. K. Lee, J. Y. Kim, S. H. Park, S. H. Kim, S. Cho, A. J. Heeger, *Adv. Mater.*, **2007,** *19*, 2445.

171. M. Wang, Q. Tang, J. An, F. Xie, J. Chen, S. Zheng, K. Y. Wong, Q. Miao, J. Xu, *Appl. Mater. Interfaces*, **2010**, *2*, 2699.

172. J. Fahlteich, M. Fahland, W. Schönberger, N. Schiller, *Thin Solid Films*, **2009**, *517*, 3075.

173. W. J. Potscavage, S. Yoo, B. Domercq, B. Kippelen, *App. Phys. Lett.*, **2007**, *90*, 253511.

174. L. Gan, R. D. Gomez, A. Castillo, P. J. Chen, C. J. Powell, W. F. Egelhoff Jr., *Thin Solid Films*, **2002,** *415*, 219.

175. A. Maestre Caro, G. Maes, G. Borghs, C.M. Whelan, *Microelectron. Eng.*, **2008**, *85*, 2047.

176. D. Rébiscoul, V. Perrut, T. Morel, C. Jayet, R. Cubitt, P.-H. Haumesser, *Langmuir*, **2010**, *26*, 8981.

177. H. Kawazoe, M. Yasukawa, H. Hyodo, M. Kurita, H. Yanagi, H. Hosono, *Nature*, **1997,** *389*, 939.

178. H. Gong, Y. Wang, Y. Luo, *Appl. Phys. Lett.*, **2000**, *76*, 3959.

179. B. K. Park, D. Kim, S. Jeong, J. Moon, J. S. Kim, *Thin Solid Films*, **2007,** *515*, 7706.

180. Y. Zhou, S. Sreekala, P. M. Ajayan, S. K. Nayak, *J. Phys. Condens. Matter*, **2008,** *20*, 095209.

181. P.J. Dingb, W. Wangb, S. Hymesc, S.P. Murakac, *Thin Solid Films*, **1995**, *262*, 234.

182. W. A. Lanford, P. J. Ding, W. Wang, S. Hymes, S. P. Muraka, *Thin Solid Films*, **1995,** *262*, 234.

183. W. A. Lanford, S. Bedell, P. Isberg, B. Hjorvarsson, S. K. Lakshmana, W. N. Gill, *J. Appl. Phys.*, **1999,** *85*, 1487.

184. A. Satta, D. Shamiryan, M.R. Baklanov, C.M. Whelan, Q. Toan Le, G.P. Beyer, A. Vantomme, K. Maex, *J. Electrochem. Soc.*, **2003**, *150*, G300.

185. D. G. Gromov, S. A. Gavrilov, E. N. Redichev, R. M. Ammosov, *Phys. Solid State*, **2007**, *49*, 178.

186. M. Frerichs, F. Voigts, W. Maus-Friedrichs, *App. Surf. Sci.*, **2006,** *253*, 950.

187. E. McCafferty, J. P. Wightman, *J. Colloid Interface Sci.*, **1997**, *194*, 344.

188. S. Lattante, A. Perulli, M. Anni, *Synth. Met.*, **2011,** *161***,** 949.

189. S. Verdier, J.B. Metson, H.M. Dunlop, *J. Mass Spectrom.*, **2007,** *42*, 11.

190. M.S. Tyler, O.S. Hutter, M. Walker, R.A. Hatton, *ChemPhysChem*, **2015**, DOI: 10.1002/cphc.201402880

191. J. Kim, J. J. Weimer, M. Zukic and D. G. Torr, *J. Vac. Sci. Technol. A,* **1994**, *12*, 3062.

192. J. W. Lee, J. Park, D. W. Kim, J. C. Noh, J. S. Choi, *Mol. Cryst. Liq. Cryst.*, **2010**, *519*, 187.

193. M.O. Reese, S.A. Gevorgyan, M. Jørgensen, E. Bundgaard, S.R. Kurtz, D.S. Ginley, D.C. Olson, M.T. Lloyd, P. Morvillo, E. Katz, A. Elschner, O. Haillant, T.R. Currier, V. Shrotriya, M. Hermenau, M. Riede, K. R. Kirov, G. Trimmel, T. Rath, O. Inganäs, F. Zhang, M. Andersson, K. Tvingstedt, M. Lira-Cantu, D. Laird, C. McGuiness, S. (Jimmy) Gowrisanker, M. Pannone, M. Xiao, J. Hauch, R. Steim, D.M. DeLongchamp, R. Rösch, H. Hoppe, N. Espinosa, A. Urbina, G. Yaman-Uzunoglu, J.-B. Bonekamp, A.J.J.M. van Breemen, C. Girotto, E. Voroshazi, F.C. Krebs, *Sol. Energy Mater. Sol. Cells*, **2011**, *95*, 1253.

194. M. D. Perez, C. Borek, S. R. Forrest, M. E. Thompson, *J. Am. Chem. Soc.***, 2009**, *131*, 9281.

195. S.R. Cowan, J. V. Li, D.C. Olson, E.L. Ratcliff, *Adv. Energy Mater.*, **2014**, *5*, 1400549.

196. E. L. Ratcliff, J. Meyer, K. X. Steirer, N. R. Armstrong, D. Olson, A. Kahn, *Organ. Electron.*, **2012**, *13*, 744.

197. C. Zhang, D. Zhao, D. Gu, H. Kim, T. Ling, Y.-K.R. Wu, L.J. Guo, *Adv. Mater.*, **2014,** *26*, 5696.

198. R.F. Bailey-Salzman, B.P. Rand, S.R. Forrest, *Appl. Phys. Lett.*, **2006**, *88*, 233502.

199. J. Lewis, S. Grego, B. Chalamala, E. Vick, D. Temple, *Appl. Phys. Lett.*, **2004**, *85*, 3450.

200. G. V Naik, V.M. Shalaev, A. Boltasseva, *Adv. Mater.*, **2013**, *25*, 3264.

201. L. Cao, L. Zhu, J. Jiang, R. Zhao, Z. Ye, B. Zhao, *Sol. Energy Mater. Sol. Cells*, **2011**, *95*, 894.

202. M. Urbańczyk, E. Maciak, K. Gut, T. Pustelny, W. Jakubik, *Bull. Polish Acad. Sci. Tech. Sci.*, **2011**, *59*, 401.

203. O. S. Hutter, H.M. Stec, R. A. Hatton, *Adv. Mater.*, **2013**, *25*, 284.

204. A. Pokaipisit, M. Horprathum, P. Limsuwan, *Nat. Sci.*, **2007,** *41*, 255.

205. M. K. Fung, K. Y. Cheung, Y. C. Sun, A. B. Djurišić and W. K. Chan, *Mater. Res. Soc. Symp. Proc.*, **2010,** *2*, 1212.

206. C. Gopalan, M.N. Kozicki, S. Bhagat, S.C. Puthen Thermadam, T.L. Alford, M. Mitkova, *J. Non. Cryst. Solids*, **2007**, *353*, 1844.

207. M. Vasilopoulou, L. C. Palilis, D. G. Georgiadou, A. M. Douvas, P. Argitis, S. Kennou, L. Sygellou, G. Papadimitropoulos, I. Kostis, N. A. Stathopoulos, D. Davazoglou, *Adv. Funct. Mater.*, **2011**, *21*, 1489.

208. M. J. Son, S. Kim, S. Kwon and J. W. Kim, *Org. Electron.*, **2009**, *10*, 637

209. H. Höchst and R. D. Bringans, *Appl. Surf. Sci.*, **1982**, *11*, 768.

210. J. B. Goodenough, *Phys. Rev.* **1960**, *117*, 1442.

211. J. B. Goodenough, *Prog. Solid State Chem.*, **1971**, *3*, 490.

212. The Essential Macleod, Thin Film Center, Inc.

213. A. Subrahmanyam, A. Karuppasamy, *Sol. Energy Mater. Sol. Cells*, **2007**, *91*, 266.

214. K. Kim, K. Hong, B. Koo, I. Lee, J.-L. Lee, *Appl. Phys. Lett.*, **2013**, *102*, 081118.

215. M.G. Hutchins, O. Abu-Alkhair, M.M. El-Nahass, K. Abdel-Hady, *J. Phys. Condens. Matter*, **2006**, *18*, 9987.

216. Z. Hussain, *Appl. Opt.*, **2002**, *41*, 6708.

217. M.C. Biesinger, L.W.M. Lau, A.R. Gerson, R.S.C. Smart, *Appl. Surf. Sci.*, **2010**, *257*, 887.

218. D. R. Lide, CRC Handbook of Chemsitry and Physics: 89th Edition, CRC Press, **2008.**

219. M.T. Greiner, L. Chai, M.G. Helander, W.-M. Tang, Z.-H. Lu, *Adv. Funct. Mater.*, **2012**, *22*, 4557.

220. S. B. Lee, J. H. Beak, B. H. Kang, K-Y. Dong, Y-Y. Yu, Y. D. Lee, B.-K. Ju., *Sol. Energy Mater. Sol. Cells*, **2013**, *117*, 203.

221. L. Fang, S. J. Baik, K. S. Lim, *Thin Solid Films*, **2014**, *556*, 515.

222. M. Vasilopoulou, A. Soultati, D. G. Georgiadou, T. Stergiopoulos, L. C. Palilis, S. Kennou, N. A. Stathopoulos, D. Davazogloua, P. Argitisa *J. Mater. Chem. A,* **2014,** *2*, 1738

223. J. Meyer, S. Hamwi, M. Kröger, W. Kowalsky, T. Riedl, A. Kahn, *Adv. Mater.*, **2012**, *24*, 5408.

224. S. Y. Chiam, B. Dasgupta, D. Soler, M.Y. Leung, H. Liu, Z.E. Ooi, L.M. Wong, C.Y. Jiang, K.L. Chang, J. Zhang, *Sol. Energy Mater. Sol. Cells*, **2012**, *99*, 197.

225. Z. Tan, L. Li, C. Cui, Y. Ding, Q. Xu, S. Li, D. Qian, Y. Li, *J. Phys. Chem. C,* **2012,** *16*, 18626.

226. S. B. Lee, J. H. Beak, B. H. Kang, K-Y. Dong, Y-Y. Yu, Y. D. Lee, B.-K. Ju, *Sol. Energy Mater. Sol. Cells,* **2013,** *117,* 203.

227. M.S. Ryu, J. Jang, *Sol. Energy Mater. Sol. Cells*, **2011,** *95*, 3015.

228. X. Yang, A. Uddin, *Renew. Sustain. Energy Rev.,* **2014**, *30*, 324.

229. N. R. Armstrong, P. A. Veneman, E. Ratcliff, D. Placencia, M. Brumbach, *Acc. Chem. Res.*, **2009**, *42*, 1748.

230. H. Pan, L. Zuo, W. Fu, C. Fan, B. Andreasen, X. Jiang, K. Norrman, F.C. Krebs, H. Chen, *Org. Electron.,* **2013,** *14,* 797.

231. P. Sullivan, A. Duraud, L. Hancox, N. Beaumont, G. Mirri, J.H.R. Tucker, R.A. Hatton, M. Shipman, T.S. Jones, *Adv. Energy Mater.,* **2011**, *1*, 352.

232. C. Li, H. Wonneberger, *Adv. Mater.,* **2012**, *24*, 613.

233. B.R. Lee, E.D. Jung, Y.S. Nam, M. Jung, J.S. Park, S. Lee, H. Choi, S.J. Ko, N.R. Shin, Y.K. Kim, S.O. Kim, J.Y. Kim, H.J. Shin, S. Cho, M.H. Song, *Adv. Mater.*, **2014**, *26*, 494.

234. W.-F. Xu, C.-C. Chin, D.-W. Hung, P.-K. Wei, *Sol. Energy Mater. Sol. Cells,* **2013**, *118*, 81.

235. T.H. Reilly III, J. van de Lagemaat, R.C. Tenent, A.J. Morfa, K.L. Rowlen, *Appl. Phys. Lett.*, **2008**, *92*, 243304.

236. L. Hu, H.S. Kim, J.-Y. Lee, P. Peumans, Y. Cui, *ACS Nano*, **2010**, *4*, 2955.

237. S. De, T.M. Higgins, P.E. Lyons, E.M. Doherty, P.N. Nirmalraj, W.J. Blau, J.J. Boland, J.N. Coleman, *ACS Nano*, **2009**, *3*, 1767.

238. S. DeMeo, *J. Chem. Educ.*, **1997**, *74*, 844.

239. C.H. Cheng, J. Wang, G.T. Du, S.H. Shi, Z.J. Du, Z.Q. Fan, J.M. Bian, M.S. Wang, *Appl. Phys. Lett.*, **2010**, *97*, 083305.

240. L.-J. Pegg, R.A. Hatton, *ACS Nano*, **2012**, *6*, 4722.